Seismic localization and observation of tectonic tremor in the northern Cascadia subduction zone

by

Madison Bombardier
B.A.Sc., Quest University Canada, 2017

A Dissertation Submitted in Partial Fulfillment of the
Requirements for the Degree of

DOCTOR OF PHILOSOPHY

in the School of Earth and Ocean Sciences

We acknowledge with respect the Lək̓ʷəŋən (Songhees and Esquimalt) Peoples on whose traditional territory the university stands, and the Lək̓ʷəŋən and W̱SÁNEĆ Peoples whose historical relationships with the land continue to this day.

Seismic localization and observation of tectonic tremor in the northern Cascadia subduction zone

by

Madison Bombardier
B.A.Sc., Quest University Canada, 2017

Supervisory Committee

Dr. Stan Dosso, Co-Supervisor
(School of Earth and Ocean Sciences)

Dr. John Cassidy, Co-Supervisor
(School of Earth and Ocean Sciences)

Dr. Honn Kao, Departmental Member
(School of Earth and Ocean Sciences)

Dr. Michel Lefebvre, Outside Member
(Department of Physics and Astronomy)

ABSTRACT

Convergent tectonic boundaries release accumulated stress on a spectrum of slip modes including large megathrust earthquakes with high societal impact, and slow slip events (SSEs), which are not felt by humans. In N. Cascadia, SSEs are regularly accompanied by seismic signals of tectonic tremor, such that the combined phenomena are referred to as episodic tremor and slip (ETS). This dissertation presents three related studies that characterize and localize tremor to better understand its generative processes and geophysical sources. I use a continuous 17-year record of tremor events to define episodes containing different numbers of events. This catalogue of episodes is used to demonstrate that major episodes (considered to represent ETS) and minor episodes exhibit distinct spatial distributions. Specifically, I provide the first observational evidence that the location of the forearc mantle corner controls whether major and minor episodes are segmented or colocated along dip. Minor episodes, which have been previously understudied, are ubiquitous along the margin but exhibit location-specific tendencies for episode sizes and recurrence intervals. To improve tremor localization, I developed the differential traveltime Bayesian inversion (DTBI) method, which prioritizes well-constrained localizations over comprehensive detection. DTBI localizes sources as 3D posterior probability distributions from which rigorous quantitative uncertainties (95% credibility intervals) are estimated. A test performed on small earthquakes supports the effectiveness of the method by relocating events within 4 km horizontally (100% of events) and 10 km vertically (90% of events) of their original locations. In addition, tremor localization exhibits less scatter than previous catalogues, indicating improved accuracy. I use the DTBI method to localize tremor sources during 20 episodes in N. Cascadia. This catalogue contains average horizontal and depth uncertainties of 4 km and 8 km, respectively. These uncertainties, which are computed for every tremor source, represent a significant improvement over previously-existing regional tremor catalogues. The enhanced constraints in the DTBI catalogue support detailed depth information that facilitates exploration of the tremor source region, which is often assumed to be the megathrust fault. I find that tremor is vertically-distributed within the deep accretionary complex up to 10 km shallower than the top of the oceanic crust (usually inferred to represent the megathrust fault). The compositional heterogeneity and structural complexity of the deep accretionary complex, as inferred from paleogeologic studies, suggest that tremor may be generated by multiple mechanisms driven by high fluid pressures and elevated strain from subduction at deeper depths.

Table of Contents

List of Tables

List of Figures

ACKNOWLEDGEMENTS

Foremost, I give thanks to my supervisors, John Cassidy and Stan Dosso, for being endlessly generous with their time and insights. I particularly benefitted from Stan's constant questioning and John's constant reminder that our work is, in fact, important. I also thank Honn Kao for providing essential expertise that supported all elements of this dissertation.

I give thanks to Ian Hoffman for always encouraging my curiosity, even when my ideas did not make sense, and for seeing that geophysics was likely a better field for me than physics. I thank Nicole Hoffman for being the pivotal geophysicist that showed me her textbooks. Her conveyance of John's social media advertisement of a Master's in seismology more than 6 years ago has resulted in this dissertation. I also thank Jackie Caplan-Auerbach at Western Washington University for spending 2.5 hours during winter break explaining the fundamentals of computational seismic analysis to a random Quest student.

I give thanks to all the staff, researchers, and students at the Pacific Geoscience Centre in Sidney for creating a rich environment of high-level, peer-based learning and discussion. Their continued enthusiastic engagement is a huge asset to graduate students.

Last, and certainly least, I give thanks to Cold Comfort Ice Cream for making the best ice cream sandwiches in Victoria by "doing whatever the hell they feel like". Eating an ice cream sandwich of their latest experimental flavour in the parking lot behind the store was always comforting, even when it was cold.

Chapter 1
Introduction

1.1 Background

A subduction zone (SZ) is a tectonic plate boundary wherein the relative displacements of two neighbouring plates is primarily convergent, causing the denser of the two to subduct into the Earth's interior. The area of contact between the two plates forms a megathrust fault that hosts seismicity of all magnitudes, including the largest earthquakes in the world. The accurate characterization of SZs and their associated earthquakes are therefore of broad societal importance. In general, megathrust faults release stress accumulated through tectonic convergence on a spectrum of slip modes, ranging from stick-slip (regular) earthquakes to continuous creep. Between the two end-member cases are slow earthquakes, often called slow slip events (SSEs), which entail event durations longer than regular earthquakes and slip rates faster than continuous creep. It is thought that many different geophysical factors influence the frictional properties that facilitate different slip modes. To a first order, the spatial distribution of areas exhibiting different slip modes varies with depth, as shown in Figure 1.1.1

In Cascadia, the seismogenic portion of the megathrust (solid and dashed yellow ellipses in Figure 1.1.1) primarily accommodates tectonic loading from its ~ 4 cm/yr convergence rate (Wells et al., 2002) as an accumulation of shear stress that is released periodically during large megathrust earthquakes. The area that constitutes the seismogenic zone remains significantly uncertain owing in part to its anomalous lack of earthquakes in recent history. Recent work suggests that the seismogenic zone experiences a high degree of locking and extends approximately to the coastline (Wang and Tréhu, 2016; Davis et al., 2023; Morton et al., 2023).

Downdip of the seismogenic zone, accumulated tectonic stress is released during SSEs (red ellipse in Figure 1.1.1). While megathrust earthquakes occur at intervals of hundreds of years, SSEs in N. Cascadia occur at intervals of approximately one year. Detection and modelling of slip during SSEs are facilitated by global navigation satel-

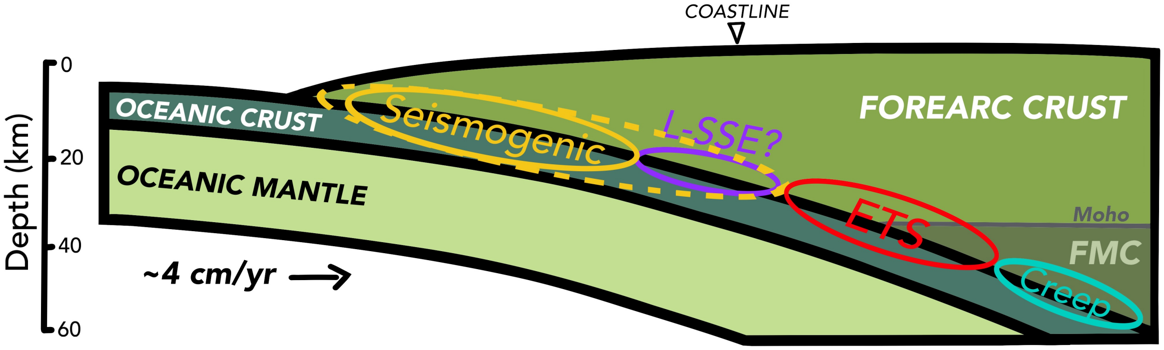

Figure 1.1.1: Schematic cross section of the N. Cascadia SZ showing the common understanding of slip modes on the megathrust. Coloured ellipses denote areas that exhibit different slip modes, including fast slip (regular earthquakes) in the seismogenic zone (yellow), long-duration SSEs (L-SSE) in a possible gap region (purple), SSEs in the episodic tremor and slip (ETS) zone (red), and continuous sliding in the creep zone (blue). The theoretical maximum extent of the seismogenic zone is indicated by the dashed yellow line. Lithologic segments are shown in shades of green. FMC: forearc mantle corner.

lite systems (GNSS), such as GPS. Displacement of the Earth's surface measured by a GNSS network can be used to model slip on a surface in the Earth's interior that represents the megathrust fault. For SSEs lasting more than a few days, slip modelling may reveal the location and migration of the slipping area during such an event. Long-term time-averaged slip models show that SSEs in Cascadia are located onshore (Bartlow, 2020).

In Cascadia, SSEs are typically accompanied by low-frequency tectonic (seismic) tremor, and the combined phenomenon is termed episodic tremor and slip (ETS; Rogers and Dragert, 2003). ETS is therefore considered one type of SSE. The proximity of the ETS zone to the seismogenic zone is an important consideration for seismic hazard assessment for two main reasons: first, the occurrence of SSEs may temporarily load the seismogenic zone, increasing the likelihood of triggering seismic rupture; and, second, the ETS zone may facilitate extended downdip rupture beyond the seismogenic zone during megathrust earthquakes. At one time it was thought that the ETS zone represented a transition between unstable (seismogenic) and stable (creeping) frictional regimes (Schwartz and Rokosky, 2007; Peng and Gomberg, 2010); however, more recent observational analyses (Wang and Tréhu, 2016) and numerical modelling (Gao and Wang, 2017) indicate that there may be a gap between the seismogenic and ETS zones (purple ellipse in Figure 1.1.1). In southwest Japan, long-duration, low-slip-rate SSEs occur in this gap area (Hirose and Obara, 2005). Such a gap may serve as a buffer between the ETS and seismogenic zones. However, if there is such a gap in Cascadia it remains undetected (e.g., Bartlow, 2020).

Although the spatial and temporal correlation of slip and tremor is well supported observationally, tremor in Cascadia tends to localize near the leading edge of the slipping area rather than the middle where peak slip rates occur (Bartlow et al., 2011; Hall et al., 2019). Globally, it is not uncommon to observe SSEs without tremor (e.g., Wallace, 2020), although there has only been one such documented case in Cascadia (S. Washington; Wech and Bartlow, 2014). While the physical nature of the relationship between tremor and slip remains largely elusive, tremor is nevertheless considered a key indicator of ETS (and thus SSEs), particularly in Cascadia where the correlation is strong. In addition, GNSS measurements are often afflicted by low signal-to-noise ratios and low sampling frequencies (e.g., one measurement per day for GPS). The comprehensive characterization of ETS tremor is therefore a crucial avenue through which to study SSEs. This dissertation focuses on localizing and characterizing the spatial distribution of tremor sources in order to better understand this component of ETS and, ultimately, the Cascadia SZ. This work provides insights into the mechanistic processes that produce tremor and the geophysical environment in which this activity occurs.

1.2 Thesis outline

This dissertation includes three main chapters with associated appendices that correspond to three scientific articles summarized below. Chapters 2 (Bombardier et al., 2024) and 3 (Bombardier et al., 2023) are published in peer-reviewed journals and Chapter 4 is submission-ready as of August 2024. My contribution to each chapter includes conceptualization, analysis, methodology, data acquisition and management, visualization, and writing. Development of the localization method presented in Chapter 3 is built upon the work of Fengzhou Tan (Tan et al., 2019) and made possible with technical contributions from Stan Dosso. All elements of this dissertation reflect guidance and editorial feedback from my supervisors, John Cassidy and Stan Dosso, and committee member Honn Kao. Some small editorial changes were made in the following three chapters to homogenize terminology and acronyms for this document. Otherwise, chapters 2, 3, and 4 are standalone journal articles that may contain some overlapping content.

Chapter 2 presents a spatial characterization of tremor episodes using a 17-year tremor catalogue from the Pacific Northwest Seismic Network (Wech, 2010). We use a clustering algorithm to construct a catalogue of episodes and investigate the differences in spatial distribution between episodes of different sizes, particularly between major tremor episodes (ETS events) and minor tremor episodes.

Chapter 3 describes a new method—the differential traveltime Bayesian inversion (DTBI) method—that addresses some of the common challenges in tremor localization. DTBI provides quantitative uncertainty analysis and improved depth estimation of tremor sources on a regional scale.

Chapter 4 employs the DTBI method to localize thousands of tremor sources to explore their distribution in depth. In particular, this work addresses large areas of scientific uncertainty regarding the structure of the N. Cascadia SZ and the nature of tremor and low-frequency earthquakes (LFEs).

Chapter 5 summarizes the main scientific contributions of chapters 2, 3, and 4, and includes discussion of possible improvements and future work related to each chapter.

Chapter 2

Spatial distribution of tremor episodes from long-term monitoring in the northern Cascadia subduction zone

Abstract

Large bursts of tectonic tremor (“major” tremor episodes) correlated with geodetic deformation recur regularly in the Cascadia subduction zone and are often called episodic tremor and slip (ETS). Minor episodes of tremor between ETS are ubiquitous but have been understudied. This paper assesses time-invariant characteristics of tremor episodes of all sizes within N. Cascadia. We derive a catalogue of tremor episodes ranging in size from 10 to $> 13,000$ tremor events using the results of 17 years of tremor monitoring. Minor episodes represent $\sim 96\%$ of all 896 tremor episodes and their occurrence varies on 10-km scales. Using estimates for the depth of the forearc Moho and subducting slab, we observe an association between the location of the forearc mantle corner (FMC) and tremor occurrence that leads to along-dip modality. Bimodality, present in southern Washington and Vancouver Island, represents the segmentation of major and minor episodes up-dip and down-dip of the FMC, respectively. Unimodality, present in Puget Sound, results when the FMC is located near the down-dip edge of the ETS zone and no segmentation occurs. We also use our extensive tremor episode catalogue alongside three-dimensional regional tomographic velocity models to reassess the relationship between tremor activity and low Vp/Vs signatures in the forearc. We do not find a correlation between tremor episode recurrence intervals and Vp/Vs, contrary to some previous work, suggesting that controls on silica precipitation in the forearc crust are not dominant controls of tremor episode recurrence, or that the association is not widely observable.

2.1 Introduction

Subduction zones (SZs) host the largest earthquakes on Earth owing to the broad area that generally constitutes the megathrust fault zone. Some segments of the megathrust fault may be incapable of hosting fast-slipping earthquakes, and instead facilitate subduction as transient slow slip events (Schwartz and Rokosky, 2007; Beroza and Ide, 2011; Ide, 2012; Obara and Kato, 2016; Wallace, 2020; Nishikawa et al., 2023; Takemura et al., 2023). In the Cascadia SZ, regularly-occurring transient surface deformation is interpreted to be slow slip on the megathrust down-dip of the seismogenic zone (Bartlow, 2020; Itoh et al., 2022). Geodetically-observed slip is often accompanied by low-frequency, semi-continuous tectonic tremor, which together are termed episodic tremor and slip (ETS) events (Rogers and Dragert, 2003). In N. Cascadia, the 14.9 ± 1.3-month recurrence interval of ETS (Kao et al., 2009) means that dozens of such events have been observed over the two decades since they were discovered.

Almost every year, ETS in N. Cascadia spans hundreds of kilometres of the SZ margin beneath Washington State and Vancouver Island (Figure 2.1.1) consisting of slip approximately equivalent to a magnitude 6.5 earthquake (Kao et al., 2010). Long-term tremor monitoring (Kao et al., 2009; Wech, 2010) has revealed abundant tremor activity between ETS, manifesting as small, short-lived episodes of relatively few tremor events, but little is known about this activity. Previous work estimates that inter-ETS activity represents 98% of episodes (Wech, 2021) comprising 20% of all tremor events (Kao et al., 2009), but this has not been verified before now.

Various properties of SZs are intrinsically linked to the tectonic tremor that they generate. For example, tremor is sometimes used as a proxy for slow slip (e.g., Obara et al., 2010; Wech and Creager, 2011; Frank, 2016). Thus, the comprehensive characterization of tremor episodes, including their spatial distribution and recurrence intervals, may be an effective method of inferring frictional properties of the megathrust. In addition, slow slip events have the capability to transfer stress to neighbouring seismogenic zones and potentially trigger seismic rupture (Obara and Kato, 2016). In this way, analysis of the full range of tremor episodes may enhance hazard assessment. The focus of this paper is primarily on the characterization of tremor episodes, including, for the first time, a detailed analysis of the more-frequent minor tremor episodes, and secondarily on properties of the SZ. To this end, we automatically define all tremor episodes in N. Cascadia consisting of as few as 10 individual events over a 17-year period between 2006 and 2023. We then use this catalogue to investigate the spatial characteristics of tremor episodes in relation to previously-modelled SZ structures.

Broadly speaking, tremor catalogues tend to include localizations that are either

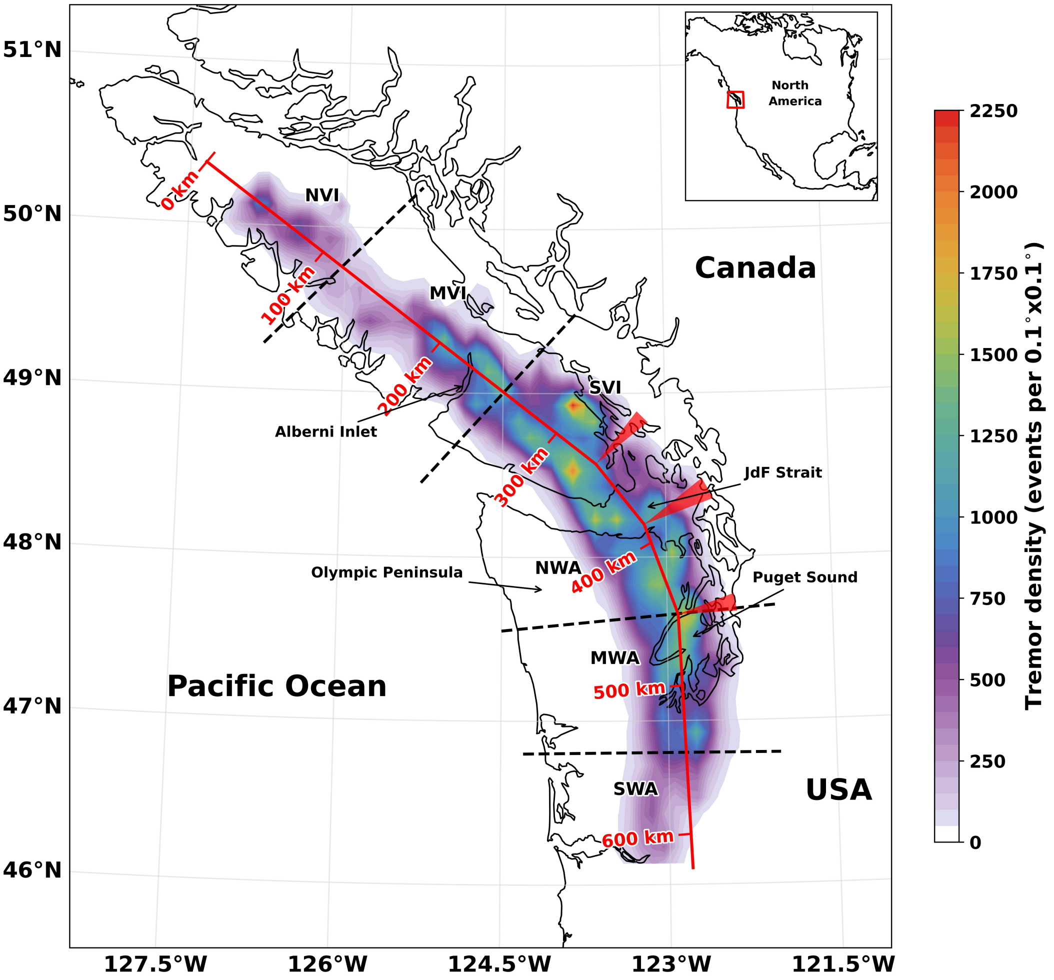

Figure 2.1.1: Map of the N. Cascadia study area and broader geographic location (inset). Tremor density of the combined tremor catalogue used in this study is shown as the shaded area. The red line pseudo-parallel to the margin denotes the 625-km transect used to cluster events. Black dashed lines delineate geographic regions referenced throughout this paper. Red triangles denote blind spots where tremor cannot be projected onto the transect at 335 km, 388 km, and 453 km along strike and discussed in Section 2.2.2. Labels are SWA, S. Washington; MWA, mid-Washington; NWA, N. Washington; JdF, Juan de Fuca; SVI, S. Vancouver Island; MVI, mid-Vancouver Island; and NVI, N. Vancouver Island.

relatively precise and targeted to a small region or time period (e.g., Armbruster et al., 2014; Peng and Rubin, 2016), or relatively imprecise and cover larger regions or time periods (e.g., Wech and Creager, 2008; Kao et al., 2009; Wech, 2010; Ide, 2012; Boyarko et al., 2015). The advantage of long-term catalogues results from the fact that larger data volumes compensate, in part, for low spatial resolution because persistent features become more evident through repeated occurrence while errors remain approximately randomly distributed. In this study, we leverage this advantage by building upon a continuous 17-year tremor catalogue, illustrated in Figure 2.1.1, to derive a catalogue of tremor episodes and assess their spatial characteristics within N. Cascadia. Specifically, we describe the spatial differences between major (ETS) and minor (inter-ETS) tremor episodes and provide observational evidence that the forearc mantle corner (FMC) is a dominant control on dip-dependent behaviour (Gao and Wang, 2017). Our episode catalogue is particularly well-suited to reexamining the relationship between episode recurrence intervals and forearc seismic velocities, which are thought to be correlated through the same generative processes (Audet and Bürgmann, 2014).

This paper employs the phrase "ETS event" with its original definition from Rogers and Dragert (2003) as the periodic combined phenomena of slow slip and tectonic tremor recurring approximately every 13–16 months, represented in this study by major tremor episodes recurring approximately every 10.5–15.5 months (discussed in Section 2.3.1). The "ETS zone" is the geographic area that regularly generates tremor during ETS events. Some tremor epicentres are localized outside the ETS zone due to natural variation as well as catalogue scatter/error. We therefore consider the ETS zone to be a subset of the "tremor zone", which is the all-inclusive geographic area in which all tremor is localized according to the catalogue employed here. "Tremor episode" refers to a distinct spatial-temporal cluster of tremor events.

2.2 Methods

We merged two catalogues of tremor epicentres computed using the waveform-envelope cross-correlation and clustering (WECC) method spanning the years 2006–2009 and 2009–2023 (Wech and Creager, 2008; Wech et al., 2009) to create one continuous catalogue spanning over 17 years. These catalogues were chosen for their temporal continuity, duration, and regional coverage. As such, the resulting merged catalogue was computed using continuous seismic data from a regional seismic network (shown in Figure A.0.1) spanning an extensive duration. Tremor events presented in this study do not have source depths associated with them; all depth values discussed in the following sections are inferred from independent models and do not represent observed tremor source depths.

2.2.1 Catalogue Processing

In 2009, the Pacific Northwest Seismic Network's (PNSN's) Tremor Map (Wech, 2010) came online providing near-real-time tremor epicentre localization along the Cascadia margin using the WECC method (Wech and Creager, 2008) and displayed at the Tremor Map webpage (`https://www.pnsn.org/tremor`). Since its debut, the WECC method producing this catalogue has undergone several informally-published updates (i.e., `https://www.pnsn.org/blog/2021/03/10/tremor-catalogue-update-again`) but retains the core methodology. A recent description of the method and updates can be found in Wech (2021). The WECC method requires temporal and spatial clustering of tremor events in order to increase the likelihood that catalogued activity is indeed tectonic tremor, which tends naturally to be clustered, and eliminate many spurious detections. We employ this catalogue, accessed from the Interactive Tremor Map in May 2023, without additional preliminary processing.

Before the advent of the Tremor Map, almost four years of tremor across the Cascadia margin between January 2006 and August 2009 was localized using an early form of the WECC method and published in various forms (e.g., Wech et al., 2009; Wech and Creager, 2011). This version does not impose clustering constraints on detections like subsequent versions; we therefore perform preliminary processing to this catalogue to remove probable non-tremor activity while preserving the majority of the catalogue. To this end, we employ the density-based spatial clustering of applications with noise (DBSCAN) algorithm (Ester et al., 1996), accessed from the Scikit-learn Python module (Pedregosa et al., 2011), in the spatial domain each four-day period. The algorithm calculates the distance between points and determines clusters according to the maximum distance between neighbouring points, *eps*, and the minimum number of points, *N*, in a neighbourhood around any given point for it to be considered part of a cluster. We set $eps = 30$ km and $N = 10$ events and perform clustering once per four-day period. Events not included in any clusters are removed, which reduces the size of the catalogue by 10%. This step does not define tremor episodes (described in Section 2.2.2), but rather enhances consistency between the pre-Tremor Map and Tremor Map catalogues by mimicking constraints later built into the WECC method that reduce scatter (Wech and Creager, 2008).

The PNSN Tremor Map and pre-Tremor Map catalogues are temporally distinct and contiguous, so there are no duplicated events or time gaps resulting from their combination. These catalogues are truncated at the southern and northern borders of the study area—46°N and 50.5°N, respectively—and temporally concatenated. Previous studies (Brudzinski and Allen, 2007; Boyarko et al., 2015; Wells et al., 2017) define the southern extent of N. Cascadia anywhere between mid-Puget Sound ($\sim$ 460 km along strike) and the Washington-Oregon border ($\sim$ 625 km along strike) on the basis of ETS recurrence intervals or tremor event density. We consider the southern limit of N. Cascadia to be approximately the border between Washington and Oregon. The combined result of these two catalogues, henceforth referred to as the combined tremor catalogue, is represented in Figure 2.1.1 as tremor event density.

2.2.2 Defining Episodes

To determine tremor episodes, the combined tremor catalogue is spatially and temporally clustered in the along-strike/time domain using DBSCAN. Figure 2.2.1 shows the results of this clustering procedure.

Along-strike distance is determined by projecting events onto a linearly-partitioned transect pseudo-parallel to the N. Cascadia margin (Figure 2.1.1). Due to the nature of using normal vectors for projecting points onto a line, the areas up-dip and down-dip of locations where two transect segments join at an angle contain events that are either normal to both segments (up-dip, inside angle) and are therefore projected onto both, or events that are not normal to either segment (down-dip, outside angle) and are therefore not projected onto the transect. The former is mitigated simply by projecting events in the duplicated area onto whichever segment is closest, but the latter cannot be mitigated. As such, $\sim$ 6000 events (2% of the combined tremor catalogue) are eliminated because they occur in one of three down-dip areas, denoted in Figure 2.1.1, located at 335 km, 388 km, and 453 km along strike. Testing different locations for transect segment joins indicates that the omission of this small set of tremor events does not affect results and interpretations in this paper.

The DBSCAN algorithm takes only one *eps* parameter, so to ensure it is applied appropriately to the spatial and temporal dimensions of the clustering domain we scale the input data directly. Specifically, we set $eps = 10$ and scale the origin times and along-strike distances to achieve this *eps* distance when the temporal difference between two events is 3.0 days and the spatial difference is 0.0 km, and conversely when the time difference is 0.0 days and the spatial difference is 20.0 km. With $N = 10$, this process essentially defines an episode as a minimum of approximately 10 tremor events with a mutually-exclusive maximum of 3 days or 20 km along strike between neighbouring events. Since there is no standard definition of tremor episodes, these constraints were determined through trial and error to resolve episodes with very few events and to prevent blending of qualitatively-distinct swarms of tremor activity. In addition,

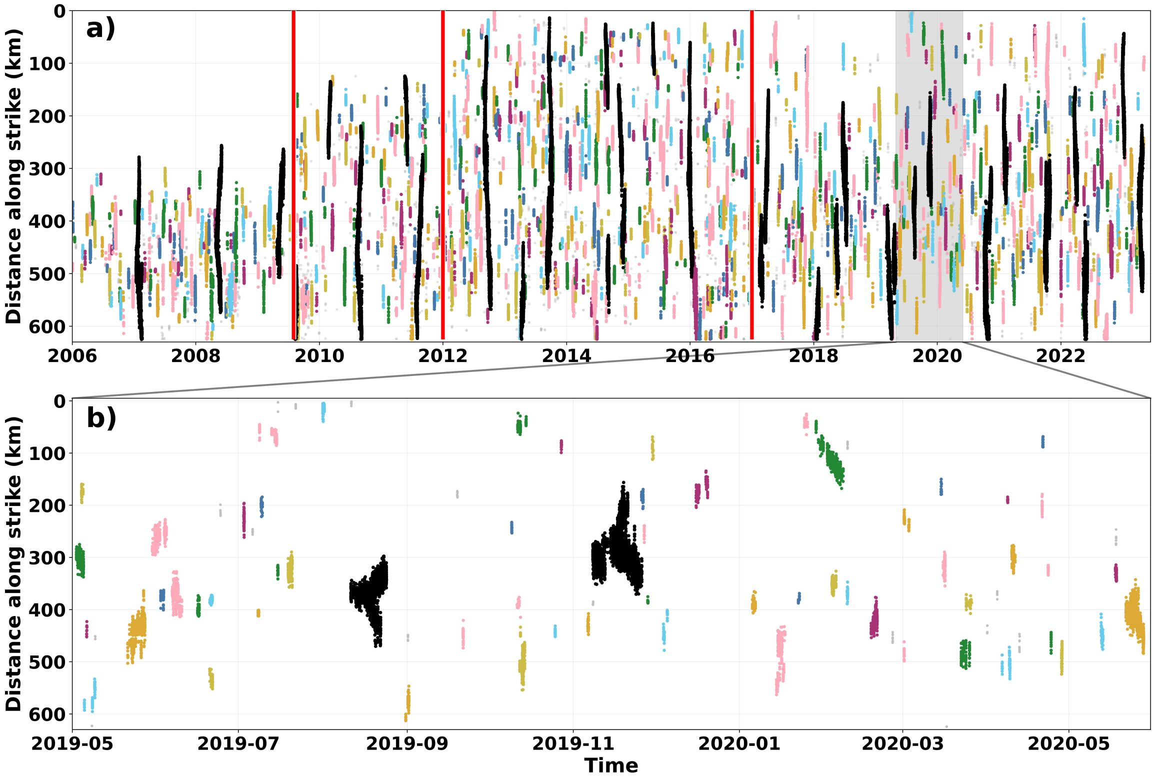

Figure 2.2.1: (a) All tremor events in the combined tremor catalogue plotted according to distance along strike from north to south over time, and (b) a zoom-in of one year. Events in minor episodes are coloured arbitrarily, events in major episodes are black, and events not part of any episode are light grey. Vertical red lines denote times of known updates to the localization methodology discussed in Section 2.2.3.

we take into account the fact that epicentral uncertainties are such that two colocated events may be erroneously localized up to approximately 16 km apart, given estimated uncertainties of 8 km (Wech and Creager, 2008). A total of 1723 events (0.65% of those successfully projected onto the transect) were not clustered into episodes (light grey dots in Figure 2.2.1) and are excluded from all subsequent analyses; the remaining 263,130 events cluster into 896 episodes that constitute a catalogue henceforth referred to as the clustered combined tremor catalogue (CCTC).

Episode metadata are derived from each cluster. Along-strike extent is quantified as the distance between the minimum and maximum tremor positions along strike within an episode. The begin and end times and locations are quantified from the origin times and positions along strike of the first and final events in an episode, respectively. Due to the built-in spatial and temporal clustering constraints in the WECC method that require a given number of events be detected per day in a given region, episode durations may be underestimated by as much as several hours if this detection threshold is not met on the days before and after episodes. Overall, episodes range from 30 minutes to 43 days in duration and 4 km to 519 km in along-strike extent. The number of events per episode is quantified simply by the number of events in each cluster. The WECC method detects tremor using 5-minute windows with 50% window overlap between consecutive search times, such that two events may be catalogued using 50% of the same seismic data at some stations. However, we consider each detection an individual event because, even in cases with the maximum data overlap of 50%, each detection is made with a unique set of seismograms. Given that there is no standard definition of a tremor event and that the duration of detection windows is largely arbitrary, we prefer not to impose additional manipulation of this statistic. Episode metadata are available online (Bombardier, 2024).

Tremor episodes that contain large numbers of tremor events (≥ 1500 events) are classified as major episodes (black dots in Figure 2.2.1) and are considered here to represent ETS events; all other episodes are classified as minor (< 1500 events). In this study we do not assume a priori that major episodes differ from other episodes in any way other than size (i.e., number of events per episode). Rather, we investigate potential differentiating characteristics between ETS events (i.e., major episodes) and inter-ETS tremor activity (i.e., minor episodes). Some studies have quantitatively assessed characteristics between major and minor tremor episodes. For example, Kao et al. (2009) differentiated four classes of tremor episodes according to tremor occurrence rate, along-strike extent, and episode duration, but subjectively defined two class tiers as consisting of ETS events. Some studies suggest that tremor epicentres localized relatively up-dip in the tremor zone primarily occur during larger episodes (Wech and Creager, 2011) and that this spatial characteristic may therefore be a universal differentiating feature. The 1500-event threshold used here to define major episodes was determined by trial and error to achieve results that subjectively conform with that of previous work (Brudzinski and Allen, 2007; Kao et al., 2009; Wech and Creager, 2011; Idehara et al., 2014; Boyarko et al., 2015). Although simplistic, this single criterion reliably identifies commonly-studied ETS events throughout the catalogued time period except in N. Vancouver Island (> 49.5°N; < 125 km along strike) where some minor episodes contain relatively large numbers of events but do not meet the major-episode criterion (examples shown in Figure A.0.2). Station density in N. Vancouver Island is lower throughout the study period and detection rates are likely lower as a result, suggesting that some large minor episodes in this region could be miscategorized major episodes. However, ETS in N. Vancouver Island is rarely studied so we are unable to compare our results to previous work. Additionally, the merged catalogue employed here does not provide coverage in N. Vancouver Island until 2012. For these reasons, we focus our comparative analysis of major and minor episodes south of N. Vancouver Island.

2.2.3 Catalogue Updates

Updates to the WECC method producing the PNSN Tremor Map catalogue have not been fully documented, but there are three known periods of change in the CCTC resulting from such updates (red vertical lines in Figure 2.2.1). The first is in August 2009 when the pre-Tremor Map and Tremor Map catalogues join, which, in addition to updating the methodology, extends coverage northward (from 275 km to 125 km along strike). The second change is in January 2012 when coverage is again extended northward (from 125 km along strike to its current limit in N. Vancouver Island) accompanied by an update to the detection procedure (`https://www.pnsn.org/blog/2012/03/30/the-wech-o-meter-takes-over-all-of-cascadia`). The third and most recent update occurred in January 2017 and again included an update to the detection procedure aimed at reducing false positives and which allowed for the detection of tremor episodes consisting of fewer events (Wech, 2021). This most recent detection update in January 2017 is expected to result in the detection of more short-duration minor episodes and more events per episode for all episodes; however, its impact appears to be focused in S. Cascadia (Wech, 2021).

To understand the impact of these updates on the CCTC, we compare the duration and number of events contained in short-duration minor episodes between distinct catalogue segments, which are shown in columns of Figure 2.2.2. Until January 2017, minor episodes of $<$ 24 hours duration are found to contain fewer than about 50 tremor events; in this range, the number of events per episode appears uncorrelated with duration, and such episodes cluster approximately uniformly within the 0–50 events per episode range (top row of Figure 2.2.2). However, after January 2017 shorter episode durations are found to be accompanied by fewer events, indicating improved resolution and detection of minor episodes of $<$ 24 hours duration. The frequency of occurrence of events in short-duration episodes (bottom row of Figure 2.2.2) decays roughly super-exponentially without noticeable differences between catalogue segments.

Since we do not compute statistics relating to episode duration or investigate temporal characteristics, changes in the detection rate of tremor over time due to methodological updates do not affect the analyses presented here. Extended northward coverage in August 2009 and January 2012 limit some along-strike comparisons that include mid-Vancouver Island and N. Vancouver Island. Changes in the detection rate over space are likely to vary due to methodological updates as well as changes to the station network. While the regional station network can change over time, the network density in mid-Vancouver Island and N. Vancouver Island is consistently lower than southern

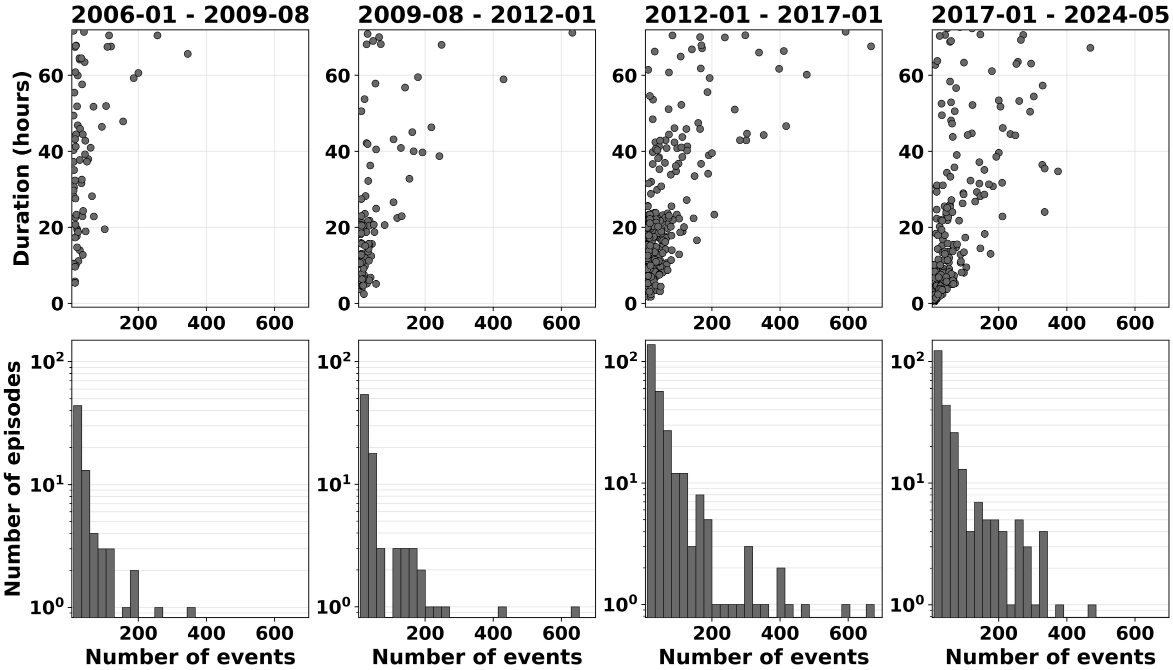

Figure 2.2.2: Duration and number of events per episode in minor episodes shorter than 72 hours across three updates to the WECC method detection procedure. The number of episodes represented in each time period (column) from left to right total 115, 111, 341, and 294, and average 20, 38, 55, and 34 episodes per year.

areas (Figure A.0.1). Over the duration of the catalogue, density of the permanent station network in Washington has increased while in S. Vancouver Island it has stayed approximately the same. In addition, not all available seismic stations are necessarily used, and the January 2017 update includes changes in the management of available seismic stations. For these reasons, the 1500-event threshold defining major episodes does not apply equally well across space and time; however, a more detailed assessment of the impact of method updates and station availability would require ground-truthing to remove natural variations over time and sensitivity testing of the methods, which is beyond the scope of this study.

2.3 Results

Of the 896 episodes determined by the clustering procedure, 3.9% (35 episodes) consisting of 64% of tremor events are classified as major episodes. On average, two major episodes per year occur somewhere in N. Cascadia. Over the 6335 days in the study period, 2321 (35%) include tremor, and 12% of days contain major episode activity somewhere in the region. The mean daily tremor occurrence rate is 3.7 times higher during major episodes than minor, with 211 and 56 events occurring per day, respec-

Table 2.3.1: Number of tremor events occurring within episodes between January 2006 and May 2023.

	Major (% of total)	Minor (% of total)	Total
Episodes	35 (3.9)	861 (96.1)	896
Events	169,288 (64.3)	93,842 (35.7)	263,130

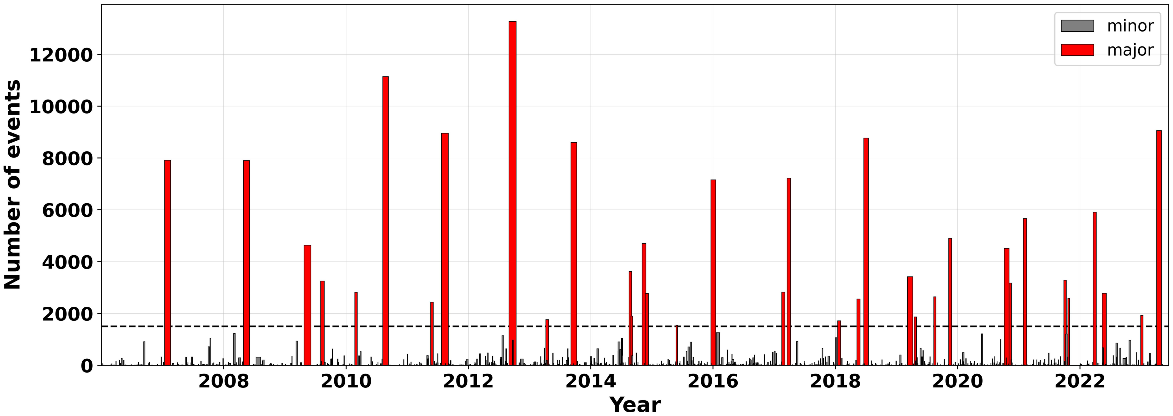

Figure 2.3.1: Number of events per episode over time. The width of bars represent episode duration. Episodes with more than 1500 events (horizontal dashed line) are defined as major and colored red. Minor episodes are colored grey.

tively. A numerical summary of tremor events in major and minor episodes is given in Table 2.3.1. Figure 2.3.1 shows episodes over time according to how many tremor events they contain. Major episodes are strikingly visible due to the fact that they often contain many thousands of events.

The spatial distribution of tremor within minor episodes of different sizes is shown in Figure 2.3.2, where the range of events per episode is doubled between panels. This figure encompasses all 861 minor episodes, the largest of which contains 1257 events. Tremor during minor episodes is ubiquitous, although nonuniform, along the margin. Tremor during minor episodes concentrates heavily in the down-dip portion of the tremor zone except in Washington where some larger minor episodes (≥ 641 events per episode) extend into up-dip areas (discussed further in Section 2.4.2). Tremor during intermediate and larger minor episodes tends to concentrate in several areas, including JdF Strait, N. Puget Sound, eastern S. Vancouver Island, mid-Vancouver Island at the inland terminus of the Alberni Inlet, and N. Vancouver Island near the northern edge of the study area (see Figure 2.1.1 for geographic references). Also notable are areas that lack tremor during episodes within one or more size denominations, including mid-Puget Sound near the border between N. and mid-Washington, which lacks tremor within all denominations except the largest (discussed further in Section 2.4.2). Two locations, the southern tip of S. Vancouver Island and the northern border of S.

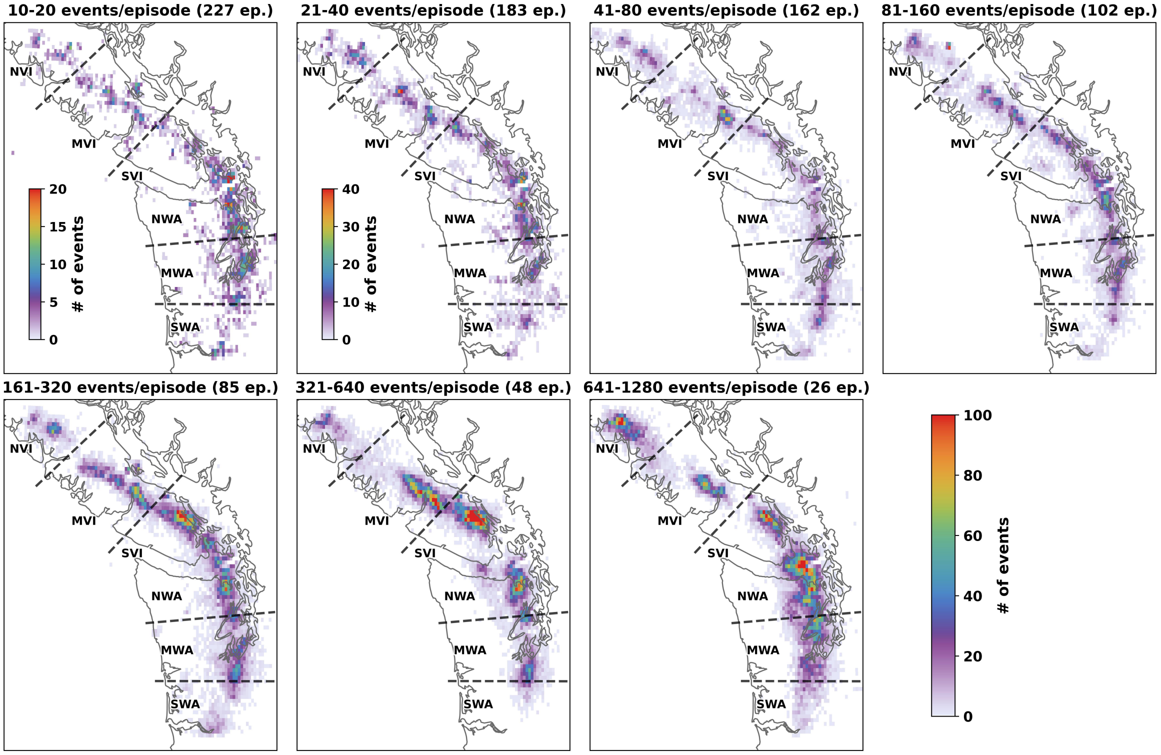

Figure 2.3.2: Heat maps of tremor events in episodes within seven denominations of episode size. The colour scale is the same for all panels except the two lowest denominations, which have their own scale to accommodate low numbers. Size denominations double between subsequent panels and the number of episodes ("ep.") in each panel is given in parentheses. The smallest minor episode contains 10 events and the largest contains 1257 events. Black dashed lines delineate geographic regions referenced throughout this paper: SWA, S. Washington; MWA, mid-Washington; NWA, N. Washington; SVI, S. Vancouver Island; MVI, mid-Vancouver Island; and NVI, N. Vancouver Island.

Vancouver Island, lack tremor during episodes larger than 321 events. Eastern S. Vancouver Island contains the highest density tremor patch in the entire region (Figure 2.1.1), which is shown in Figure 2.3.2 to be composed of episodes primarily in the three largest denominations.

2.3.1 Recurrence Intervals

We assess episode recurrence intervals by dividing the study area into 0.05° × 0.05° (∼ 5 × 5 km) cells and identifying the earliest time episodes had tremor activity in each cell. The mean time difference between the first tremor event in consecutive episodes in each cell is considered the recurrence interval of episodes in that cell. Recurrence intervals over the region are shown in the first column of Figure 2.3.3, as well as the associated coefficient of variation (standard deviation divided by the mean) in the second column. All episodes are represented in the top row of Figure 2.3.3 (panels a–d), major episodes in the middle row (panels e–h), and minor in the bottom row (panels i–l).

Figure 2.3.3a–d shows that 90% of recurrence intervals for all episodes are between 80 and 650 days (2.5–21.5 months). Episodes are 2–3 times more numerous with 2–4 times shorter recurrence intervals in down-dip portions of the tremor zone compared with up-dip portions. Despite the greater number of episodes down-dip, there is no significant difference in the number of tremor events between up-dip and down-dip areas, indicating that up-dip areas are activated less frequently but generate more tremor events when activated. The observation that activation rates are dip-dependent is independently supported by the facts that minor episodes occur primarily down-dip (Figures 2.3.2 and 2.3.3l) and exhibit 3.7 times lower mean daily tremor occurrence rates compared to major episodes (discussed in Section 2.3).

Figure 2.3.3e–h shows that 50% of recurrence intervals for major episodes are between 320 and 460 days (10.5-15.5 months), roughly consistent with previous work: 420 days, 447 days, and 240–480 days from Brudzinski and Allen (2007), Kao et al. (2009), and Boyarko et al. (2015), respectively. The median coefficient of variation is 0.5, which translates to a median standard deviation of approximately 200 days, although 50% of standard deviations are between 40 and 200 days. These values demonstrate significantly more variability in the recurrence of major episodes than previous estimates of 40 days from Kao et al. (2009) and 60 days from Brudzinski and Allen (2007). Major episodes fill nearly the entire tremor zone along dip and exhibit no along-dip trends on three of the four metrics represented (Figure 2.3.3e, f, and g). Tremor events during major episodes are 2–5 times more numerous in up-dip portions than down-dip. Most

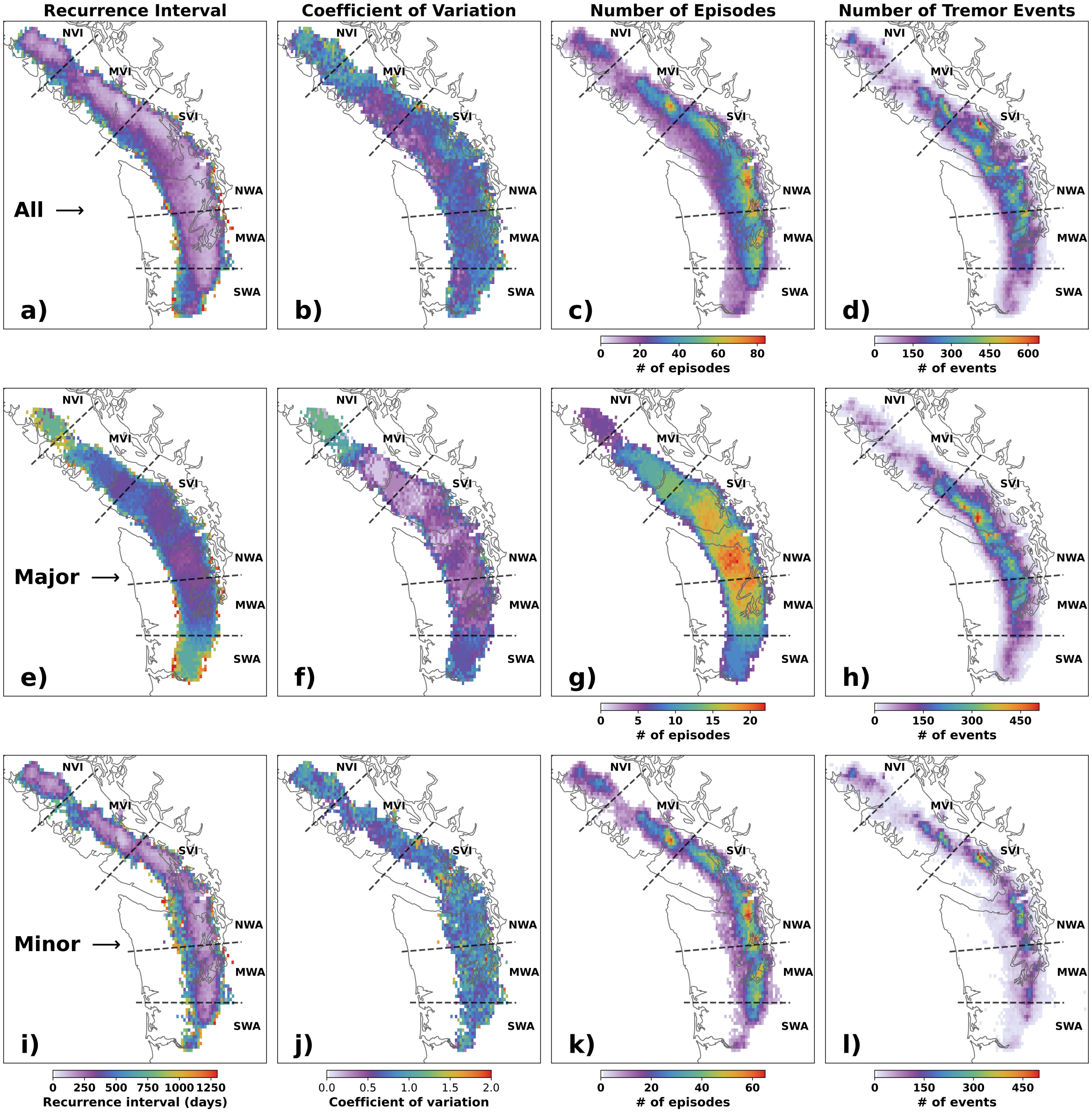

Figure 2.3.3: Recurrence intervals, coefficient of variation, and occurrence of tremor episodes and events in $0.05^\circ \times 0.05^\circ$ cells with ≥ 5 episodes present. (a)–(d) represents all episodes, (e)–(h) represents major episodes, and (i)–(l) represents minor episodes. The first two columns use the same colour scales shown at the bottom. Black dashed lines delineate geographic regions referenced throughout this paper: SWA, S. Washington; MWA, mid-Washington; NWA, N. Washington; SVI, S. Vancouver Island; MVI, mid-Vancouver Island; and NVI, N. Vancouver Island.

major episodes occur in S. Vancouver Island and N. Washington, although changes in regional coverage provided by the CCTC northward of S. Vancouver Island preclude region-wide along-strike comparisons. Near the southern extent of N. Cascadia, S. Washington is characterized by few major episodes, 8 episodes total, compared to 15–19 episodes in N. Washington.

Figure 2.3.3i–l shows that minor episodes are characterized by shorter recurrence intervals overall but span a wide range, with 50% of recurrence intervals between 100 and 340 days (3.5–11.5 months). The narrowest range containing 50% of coefficients of variation is 0.6–0.88, translating to 50% of standard deviations between 80 and 290 days with a median of 278 days. This demonstrates significant variability in minor episode recurrence even where they recur most frequently. Minor episodes occur primarily in down-dip portions of the tremor zone. Unlike major episodes, minor episodes exhibit finer-scale spatial variation along strike. Notably, the spatial distribution of tremor during minor episodes (Figure 2.3.3l) includes gaps along strike where tremor occurrence is vanishingly low (Figure 2.3.2). The down-dip concentration and along-strike variability of minor tremor activity reveal that the processes and structures that generate tectonic tremor vary over distances of tens of kilometres in dip and strike directions. Section 2.4.2 includes a more-detailed discussion of the distribution of minor episodes.

2.4 Spatial Correlations with Tremor Activity

In this section, we use our long-term CCTC to review two features thought to be spatially correlated with tremor activity—namely, seismic velocities in the forearc and the location of the FMC. The SZ model employed here is a three-boundary model estimated from receiver function inversion by Bloch et al. (2023). The model resolves boundaries interpreted to be the oceanic Moho, the top of the oceanic crust, and the upper extent of the ultra-low velocity zone. We use the top of the oceanic crust (termed the "c horizon" in Bloch et al., 2023) as the estimated surface of the subducting slab. In this section, the "ETS zone" is considered to be everywhere in the tremor zone where recurrence intervals are $\leq$ 450 days (within the dark blue line in Figure 2.4.1). Since 450 days is the high end of recurrence intervals for major episodes, and since major episodes tend to fill the width of the tremor zone, limiting analysis to this subregion considers only the area in which tremor occurs regularly.

2.4.1 Relation to Forearc Velocities

It is generally thought that ETS activity is associated with the presence of fluids through one or more mechanisms; for example, by inducing high pore-fluid pressures and reducing effective normal stress in the SZ. The production (e.g., Peacock, 2009; Condit et al., 2020; McLellan et al., 2022), transport pathways (e.g., Hyndman et al., 2015; Savard et al., 2018), and storage locations (e.g., Egbert et al., 2022) of slab-derived fluids are therefore rich areas of study. Independent observations of anomalously-low Vp/Vs ratios in the continental forearc above the ETS zone suggest relatively-high concentrations of silica (Audet et al., 2010; Ramachandran and Hyndman, 2012; Hyndman et al., 2015; Savard et al., 2018). Although there remain debates about the details, the leading general hypothesis is that silica precipitates into quartz in the forearc from slab-derived fluids along (sub)vertical transport pathways. Within this framework, Audet and Bürgmann (2014) show that forearc Vp/Vs in S. Vancouver Island correlates with recurrence intervals of tremor episodes in N. Washington. Specifically, they observe a Vp/Vs trend that decreases linearly with plate interface depth. Since tremor episode recurrence intervals also decrease with down-dip distance (Wech and Creager, 2011), they argue that the same processes producing quartz-enriched forearcs (low Vp/Vs) also shorten tremor episode recurrence intervals. In this section, we investigate the relationship between forearc Vp/Vs and recurrence intervals using regional tomographic velocity models and our CCTC.

The Vp/Vs model we use, shown in Figure 2.4.1, is derived from three-dimensional Vp and Vs tomographic models of Vancouver Island (Savard et al., 2018) and Washington (Merrill et al., 2020) from mostly passive sources. The same methodology is used to compute both models making them directly comparable (Merrill et al., 2020). The two models are merged in-kind by interpolating each onto a common $1 \times 1 \times 1$ km grid and taking an average between the two at nodes where both contain values. Merged Vp and Vs models are used to create a Vp/Vs model. Forearc Vp/Vs is determined by averaging columns of the Vp/Vs model from 10 km depth down to the nearest 1-km grid node equal to the shallowest depth of either: (1) the top of the ultra-low velocity zone given in the SZ model (Bloch et al., 2023), or (2) the shallowest regional estimate for the continental Moho, which we take to be 36 km (McCrory et al., 2014). In this way we reduce the influence of velocities near the surface, in the ultra-low velocity zone, and in the continental mantle. Forearc Vp/Vs is broadly associated with coastal terrane complexes (Merrill et al., 2020); specifically Siletzia through Washington (high Vp/Vs), the Olympic Accretionary Complex beneath the Olympic Peninsula in N. Washington (low Vp/Vs), and the Wrangellia complex in Vancouver Island (low Vp/Vs).

We assess the relationship between forearc Vp/Vs and recurrence intervals by ex-

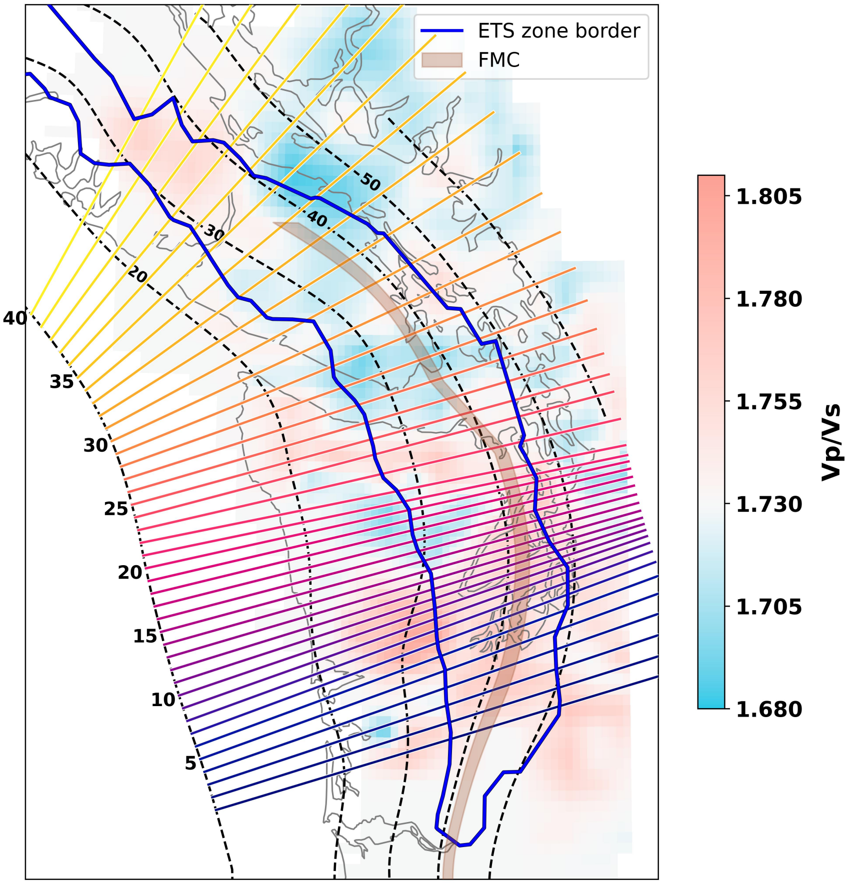

Figure 2.4.1: Forearc Vp/Vs from combined tomographic Vp and Vs models. Transects used in Sections 2.4.1 and 2.4.2 are shown as numbered coloured lines. Black dashed lines denote isodepth contours of the subducting slab in 10-km intervals. The dark blue contour line denotes the border around the ETS zone. The shaded brown area denotes the location of the FMC corresponding to 36–38 km and 41–43 km isodepth contour ranges of the slab surface in S. Vancouver Island and Washington, respectively, connected linearly through the JdF Strait.

tracting these values within the ETS zone along 40 transects perpendicular to the 10 km isodepth contour of the subducting slab shown in Figure 2.4.1. There are two idiosyncrasies employed here to be consistent with the methods of Audet and Bürgmann (2014), whose results partially depend on those originally presented in Wech and Creager (2011). First, because the ETS zone is defined as the area where recurrence intervals are ≤ 450 days, and because minor episodes occur primarily down-dip with greater frequency, recurrence intervals generally decrease along dip from the up-dip edge of the ETS zone to the location where minor episodes are most frequent, beyond which they increase (Figure 2.3.3a). In this way, recurrence intervals along dip asymmetrically decrease and then increase (Figure A.0.3a). As such, it is necessary to consider only the decreasing trend of recurrence intervals from the up-dip edge of the ETS zone, as seems to have been done in Wech and Creager (2011). Second, Wech and Creager (2011) argue that recurrence intervals averaged through N. Washington and the JdF Strait decrease with horizontal down-dip distance, which Audet and Bürgmann (2014) translate to plate interface depth. Such a translation is non-linear if the slab dip is irregular and/or the up-dip edge of the ETS zone corresponds to different slab depths along strike; it is not clear how or whether these factors were accommodated in that work. The slab model we employ indicates that slab depths at the up-dip edge of the ETS zone in N. Washington vary between 25 and 30 km and slab dips vary between 7° and 12°. In addition, expanding the study area beyond N. Washington introduces slab depths that vary significantly more than that; S. Washington has deepest slab depths spanning 37–52 km in the ETS zone, whereas mid-Vancouver Island has the shallowest spanning 30–39 km. Indeed, the depth ranges of the slab in the ETS zone in mid-Vancouver Island and S. Washington are nearly mutually exclusive, with the only overlap occurring between 37 and 39 km depth (Figure A.0.4). As such, the common reference for recurrence intervals along dip is not slab depth, but slab depth *increase* from the up-dip edge of the ETS zone. In other words, we normalize the slab depth range in the ETS zone by its shallowest depth in the ETS zone. This is similar to the horizontal down-dip distance reference used by Wech and Creager (2011) in that it makes the origin the up-dip edge of the ETS zone, but should be more accurate because it takes into account slab geometry. Recurrence intervals and forearc Vp/Vs in the ETS zone with reference to slab depth increase along each transect are summarized in Figure 2.4.2.

Recurrence intervals overall decrease approximately exponentially with slab depth increase, represented in Figure 2.4.2a, consistent with findings from Wech and Creager (2011). A linear least-squares exponential fit is expressed mathematically as $a10^{-x/b}$, where $a = 363$, $b = 25$, and x is slab depth increase in kilometres, with a resulting r^2 value of 0.7. Forearc Vp/Vs (Figure 2.4.2b) varies irregularly along strike broadly reflecting the overall forearc lithology, with higher values (> 1.73) in Washington and

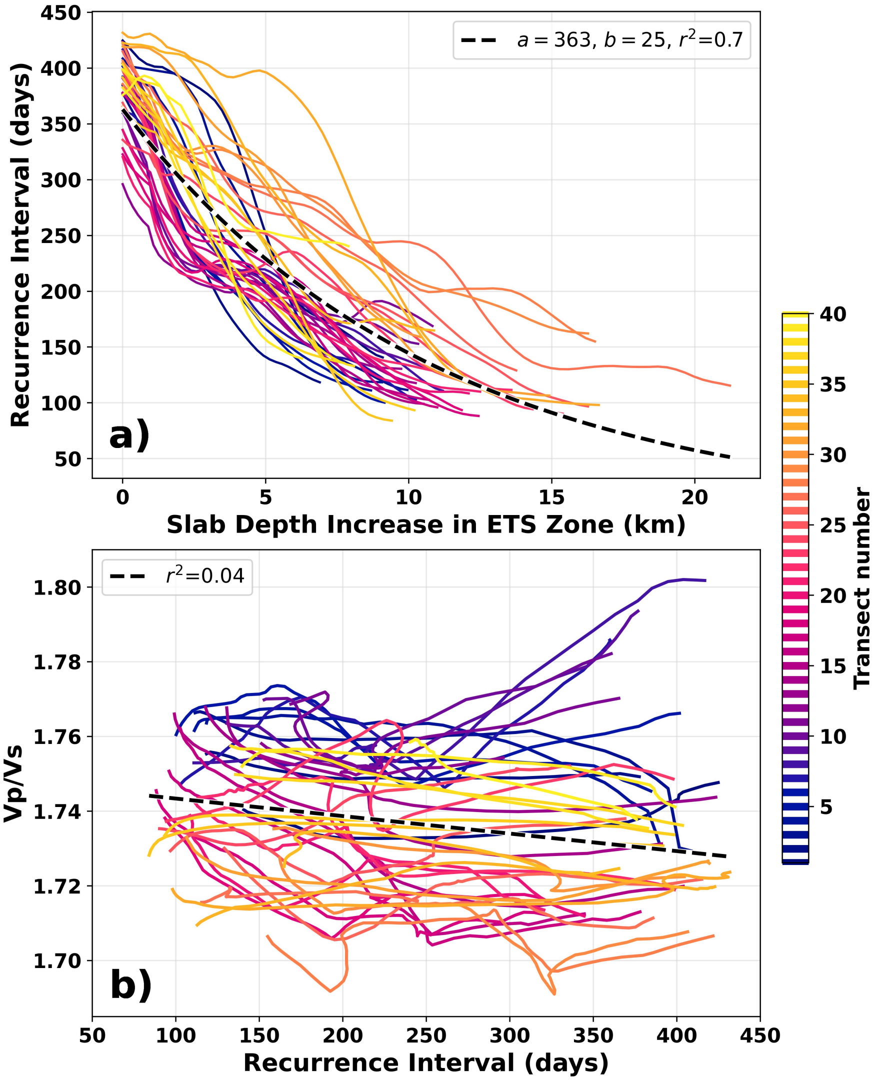

Figure 2.4.2: Recurrence intervals and forearc Vp/Vs with slab depth increase in the ETS zone along 40 margin-normal transects coloured corresponding to Figure 2.4.1 (blue in the south to yellow in the north). (a) recurrence intervals as a function of slab depth increase. The black dashed line denotes a linear least-squares best-fit exponential decay with an r^2 value of 0.7. (b) forearc Vp/Vs as a function of recurrence interval. A poorly-fit ($r^2 = 0.04$) linear relationship between Vp/Vs and recurrence intervals is denoted by the black dashed line. A version of this figure using slab depth and the full range of recurrence intervals is available in Figure A.0.3.

mid-Vancouver Island and lower values (< 1.73) in the JdF Strait and S. Vancouver Island. However, forearc Vp/Vs appears to have no relationship to tremor episode recurrence intervals, contrary to findings from Audet and Bürgmann (2014). A linear function fit to these data (dashed line in Figure 2.4.2b) has a very small r^2 value (0.04), indicating that a linear trend does not represent the data.

Reasons for this difference could be that Audet and Bürgmann (2014) extract Vp/Vs (in S. Vancouver Island) and recurrence intervals (in N. Washington) from different locations, which are characterized by different forearc lithologies. These locations also represent a minority of the N. Cascadia margin. In contrast, results presented here encompass the entire N. Cascadia region, including areas targeted by Audet and Bürgmann (2014), with an emphasis on uniform geographic coverage and direct dataset comparison. Considering recurrence intervals and forearc Vp/Vs only in those areas included in Audet and Bürgmann (2014) also does not replicate their finding (Figure A.0.5). Forearc velocities estimated using tomography are expected to vary less widely than those estimated using receiver functions due to regularization, but regional trends present in large volumes, such as the forearc through N. Cascadia, should be resolved by both methods. We therefore conclude that in N. Cascadia the composition of forearc crust as inferred by Vp/Vs, whether indicative of exogenous terrane lithologies or silicates precipitated in situ, is not associated with tremor episode recurrence intervals along dip. We note, however, that these results do not preclude a correlation between silica precipitation and ETS characteristics in general; our results indicate specifically that tomographic Vp/Vs throughout the mid- and lower-forearc bares no relation to the full range of tremor-episode recurrence intervals in N. Cascadia.

Audet and Bürgmann (2014) additionally demonstrate a correlation between regional average forearc Vp/Vs and recurrence intervals of major tremor episodes (i.e., ETS events) globally. Specifically, they find that higher regionally-averaged forearc Vp/Vs is associated with longer recurrence intervals of ETS events in five SZs across the globe, including the southern, central, and northern segments in Cascadia. They use these observations to support their aforementioned proposition linking silica precipitates (low Vp/Vs) to ETS characteristics (short recurrence intervals). Work from McLellan et al. (2022) supports the correlation by demonstrating that regional fluid flux estimates from slab dehydration at continental Moho depths are negatively correlated with major episode recurrence intervals (i.e., larger flux is associated with shorter ETS recurrence intervals) across the three Cascadia segments. However, our dataset is not conducive to investigating this relationship because major-episode recurrence intervals vary negligibly across N. Cascadia.

Other studies reveal complex relationships between slow earthquake characteristics, regular seismicity, and seismic velocities. While fluid presence appears to be commonly associated with slow earthquakes (Audet and Kim, 2016), there are variations within and between regions regarding where fluids take up residence and what results from their presence (Delph et al., 2021; Egbert et al., 2022). For instance, some work suggests that fluids allowed to migrate into the forearc crust serve to drain the megathrust (lower fluid pressures), induce forearc metamorphism, and increase rates of crustal seismicity (Kato et al., 2010; Nakajima and Hasegawa, 2016). In Cascadia, if there is indeed widespread silica enrichment from slab-derived fluids, this would seem to indicate drained conditions in the megathrust leading to reduced pore-fluid pressures and reduced slow earthquake activity (i.e., longer recurrence intervals)—the opposite of what Audet and Bürgmann (2014) observe. Additionally, if fluids in the forearc increase seismicity rates, the dearth of crustal earthquakes in the ETS zone in Cascadia (Bostock et al., 2019) would seem to suggest limited fluid presence in the forearc and thus minimal silica enrichment. The seemingly-contradictory nature of this body of work regarding high pore-fluid pressures in the ETS zone and the ingress of fluids into the forearc (discussed in detail by Savard et al., 2018) likely represents the inherent complexity of the topic and the challenges of its study. The observations presented here suggest that the full spectrum of tremor episode recurrence intervals and forearc Vp/Vs preclude a simple relationship within N. Cascadia.

2.4.2 Along-dip Modality

Using thermal modelling, Gao and Wang (2017) demonstrate the existence of a weak velocity-weakening segment of the subduction megathrust around the FMC (i.e., in the ETS zone) in warm SZs. In their models, this frictionally-weak portion of the megathrust is neighboured by velocity-strengthening segments up- and down-dip. They argue that these conditions are facilitated by processes that are both concurrent and sequential, which are: the release of fluids from the slab via metamorphic dehydration reactions; fluid-driven serpentinization of the FMC and quartz precipitation in the lower forearc crust; and permeability reduction of the forearc crust and mantle, resulting in high pore-fluid pressures and low shear strength on the megathrust. In this way, Gao and Wang (2017) argue that the thermo-petrological environment around the FMC may give rise to an isolated friction zone capable of exhibiting unstable slip induced by stable slip in neighbouring segments. Observational studies from southwestern Japan show that tremor episodes located down-dip of the FMC, as inferred from receiver function analysis (Sawaki et al., 2021), recur frequently (nearly continuously), whereas tremor activity in up-dip areas mainly consists of major episodic bursts (Obara et al., 2010). This dip-dependent behaviour creates tremor density distributions that are bimodal around the FMC. In this section we investigate the spatial relationship between tremor activity and the FMC in N. Cascadia and provide observational evidence that the location of the FMC is a dominant control on along-dip tremor distributions and the segmentation of major and minor episodes.

The location of the FMC, that is, the intersection of the continental Moho and subducting plate, is inferred from depth estimates of the Moho and the depth of the subducting slab model employed here. In N. Cascadia, free fluids and serpentinization in the mantle wedge lower seismic velocities thereby obscuring velocity contrasts between forearc crust and mantle near the subducting slab (Bostock, 2013). A review of the literature by McCrory et al. (2014) finds that estimates of the depth and slope of the forearc Moho near the subducting plate can vary significantly between studies due to uncertainties on both the data and their interpretation. Based on their aggregation of results from the studies they analyzed, the preferred conclusion from McCrory et al. (2014) is a horizontal Moho that is deeper in Washington, from 41–43 km, and shallower in S. Vancouver Island, from 36–38 km. These ranges do not reflect formal uncertainties, which are unknown, but rather the approximate ranges of the data. The brown shaded region in Figure 2.4.1 denotes the area between 41 and 43 km isodepth contours of the slab in Washington and 36 and 38 km in S. Vancouver Island connected with straight lines through the JdF Strait. This shaded region is henceforth considered to represent the location of the FMC.

In Section 2.3.1, we showed that tremor during minor episodes concentrates in the down-dip portion of the tremor zone (Figure 2.3.3l), and that tremor during major episodes fills nearly the entire tremor zone but concentrates in the up-dip portion (Figure 2.3.3g and h). Figure 2.4.3 shows the distribution of tremor during all, major, and minor episodes and the location of the FMC along transects shown in Figure 2.4.1. The FMC is generally located in the middle or down-dip portion of the tremor zone. Through central and N. Puget Sound (transects 9–22) the FMC is nearer the down-dip edge of the tremor zone and tremor event distributions are largely unimodal (Figure 2.4.3a); tremor concentrates in mid- and down-dip portions of the tremor zone but still up-dip of the FMC. Conversely, where the FMC is located nearer the middle of the tremor zone, such as through the JdF Strait and S. Vancouver Island (transects 24–33), there are relatively fewer events near the FMC and higher concentrations up- and down-dip resulting in bimodal distributions. This association ceases north of S. Vancouver Island (transect 33) where the tremor zone steps seaward and slab depths are shallower than the shallowest depth estimate of the S. Vancouver Island Moho.

Comparison of Figure 2.4.3b and c demonstrates that bimodal tremor distributions (in Figure 2.4.3a) are the superposition of tremor during minor episodes (concentrated down-dip) and major episodes (concentrated up-dip). Unimodal distributions occur

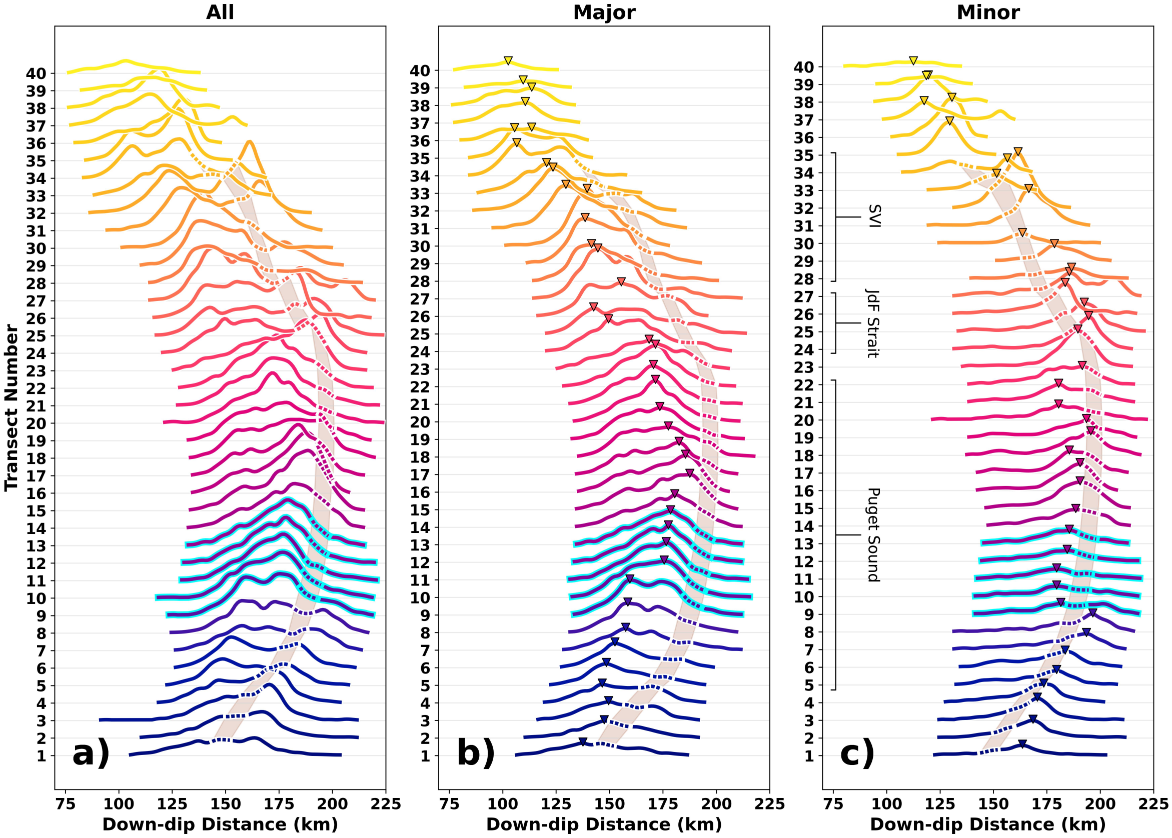

Figure 2.4.3: Relative number of tremor events during all (a), major (b), and minor (c) episodes along margin-perpendicular transects coloured and numbered according to Figure 2.4.1. The maximum along each transect is denoted with an inverted triangle in (b) and (c). The FMC is denoted by the dotted portion of the lines and connected by the brown shaded region for clarity. Transects through mid-Puget Sound are outlined with light blue and discussed in Section 2.4.2. Tremor data presented in (a), (b), and (c) are extracted from Figures 2.3.3d, h, and l, respectively. Vertical scales are the same for all panels.

where the FMC is located near the down-dip edge of the tremor zone, such that tremor during all episodes is colocated mid-dip. In this way, the position of the FMC in the tremor zone appears to be a dominant control on whether major and minor tremor activity is spatially segmented (bimodal) or colocated (unimodal).

Recall that episodes are classified based only on whether the 1500-event-per-episode threshold is met; no spatial prerequisites were imposed, signifying that the simple criterion accurately reflects inherent differences between major and minor episodes. If the association between major and minor tremor episodes and the FMC is shown to be robust through replication in future work, the distribution of tremor, in particular the presence of along-dip bimodality, may be used to constrain the location of the FMC where the depth and geometry of the forearc Moho are uncertain.

Despite the observation that bimodality results from segmentation of major and minor episodes, which have systematically different recurrence intervals, we do not observe any clear feature in recurrence intervals along-dip corresponding to the FMC (Figure A.0.6). One possible reason for this is the fact that recurrence intervals across the region are derived from the binary occurrence of episodes within discrete cells; in a given cell, an episode is either present or not present, and a single tremor event signifies the presence of an episode. This reflects the maximum distribution of tremor events within episodes; the spatial distribution of episodes and their recurrence intervals are expanded to the broadest areas due to the grid-based binning of scatter in the tremor catalogue. Along-dip analysis of recurrence intervals using tremor catalogues with greater epicentral precision may illuminate trends not resolvable by our CCTC.

The spatial association of the tremor zone with high fluid fluxes (McLellan et al., 2022) and high pore-fluid pressures (Audet et al., 2009) suggests that tremor-genic mechanisms are likely facilitated, in part, by fluids (Bernaudin and Gueydan, 2018; Platt et al., 2018; Shapiro et al., 2018; Benson et al., 2020). Geologic studies of exhumed, ancient SZs that likely hosted ETS observe abundant mineralized fault networks and veins interpreted to be evidence of fluids and high pore pressures at depth (Bürgmann, 2018; Kirkpatrick et al., 2021). The present study focuses on macroscopic observations and is not ideal for investigating probable tremor-genic mechanisms, especially because the tremor catalogue employed here does not resolve source depths, but any proposed mechanisms must be able to explain the full spectrum of observations presented here and throughout the published literature.

It has been widely shown that some portion of tremor waveforms contains signals from events considered low-frequency earthquakes (LFEs; Shelly et al., 2007; Brown et al., 2009; Frank et al., 2014; Royer and Bostock, 2014) and very low-frequency earthquakes (VLFEs; Ide et al., 2008; Ide, 2016, 2019; Fan et al., 2022). Whether such events constitute the entire tremor signal is difficult to demonstrate conclusively. LFEs and VLFEs exhibit impulsive waveforms with focal mechanisms largely consistent with slip on a low-angle thrust fault, such as the megathrust. Numerical simulations (e.g., Luo and Liu, 2021) and models (e.g., Sibson, 1990, 2013) of ETS can successfully replicate geodetic and seismological observations using fluid-controlled, friction-based frameworks on or within the megathrust system. Simulations (Farge et al., 2023) and laboratory experiments (Yuan et al., 2024) of systems involving non-slip mechanisms, such as hydraulic fracture, also present intriguing models of tremor generation. While pure dilatational fracturing cannot explain the inferred thrust mechanism associated with tremor, shear strain within structurally-complex folded networks, such as those widely observed in exhumed SZs, is expected to produce both extensional fracture and shear slip (Platt et al., 2018; Sibson, 2017; Ujiie et al., 2018). More work from an array of disciplines is needed to comprehensively understand the geophysical processes underlying the various components of tremor signals.

Puget Sound

Minor episodes within most of Puget Sound (Figure 2.4.3) occur primarily up-dip of the FMC (colocated with major episodes), in contrast with the rest of the N. Cascadia margin. The mid-Puget Sound area in particular (Figure 2.4.3 transects 9–13 outlined in light blue) hosts minor episodes that are less numerous (Figure 2.3.3l) with dip-averaged recurrence intervals 100 days longer than the rest of the region (350 days rather than 250 days). However, the number of major episodes (Figure 2.3.3g) and total number of tremor events (Figure 2.3.3d) are approximately consistent with the rest of the region. Wech (2021) similarly showed that cumulative tremor energy in mid-Puget Sound does not exhibit a deficit. These observations demonstrate that tremor activity in mid-Puget Sound is not diminished overall, despite a deficit of minor episodes, but manifests mainly as major episodes. In this study, it is the character of minor episodes, specifically their conspicuous absence, that makes the mid-Puget Sound area stand out. This highlights the importance of including minor episodes in the study of ETS.

Irrespective of tremor activity, several observations from the literature suggest Puget Sound as a whole is unique within N. Cascadia. First, regular in-slab and crustal seismicity is considerably more prevalent and includes some of the largest known earthquakes in the region (McCrory et al., 2012; Schneider et al., 2023). Second, the forearc beneath mid-Puget Sound is highly deformed with several major faults (i.e., Tacoma Fault Zone, Seattle Fault, and Southern Whidbey Island Fault Zone), accreted terranes, contiguous regions of uplift and subsidence (i.e., Seattle Uplift, Seattle Basin, and Tacoma Basin), and deep structure whose lithology remains unknown (Merrill et al., 2020). Third, McCrory et al. (2012) and Bloch et al. (2023) respectively identify significant deformation of the subducting slab and oceanic Moho that indicate localized deepening of the down-going plate. Adding tremor activity to this list, Brudzinski and Allen (2007) and Boyarko et al. (2015) identify mid-Puget Sound as a significant impedance to along-strike migration of major episodes (also supported by our catalogue, Figure A.0.7). We suggest that the character profile of minor tremor episodes, such as recurrence intervals and distribution with respect to the FMC, provides insights into the tectonic and geophysical environment that may not be available from analysis of major episodes alone.

2.4.3 Limitations and Future Work

While this study reveals crucial features of the spectrum of tremor activity on the basis of numbers of events, we do not address time-dependent aspects such as migration paths, episode durations, or scaling relations. The study of tremor and/or LFE migration patterns especially can reveal important properties of slow earthquakes (Frank and Brodsky, 2019; Gombert and Hawthorne, 2023) and their relation to fast earthquakes (Obara and Kato, 2016). We also do not make any observations on the depth of tremor sources, which is a critical unknown that requires more investigation in order to improve our understanding of possible tremor-genic mechanisms and controls. The absence of depth constraints are particularly problematic in N. Cascadia where interpretations of SZ structure are still debated (e.g., Calvert et al., 2020; Bloch et al., 2023).

We also do not consider observed or predicted slip that may be associated with tremor activity. While tremor and slow slip are spatially and temporally correlated, they are often not colocated (Bartlow et al., 2011; Itoh et al., 2022). For example, Hall et al. (2019) demonstrate that peak tremor occurrence during N. Cascadia ETS events is often localized to the leading edge of the propagating slip front a few days ahead of peak slip rates. We therefore do not extrapolate trends in the geographic distribution of tremor to slip at depth, as is sometimes done (e.g., Wech and Creager, 2011).

Finally, our results demonstrate that many tremor episodes are very small—around 28% of episodes contain fewer than 25 events and are shorter than 24 hours—and persistent spatial features of minor episodes vary on 10 km scales. Close analysis of such activity requires greater localization precision and more comprehensive detection of tremor than the WECC method can currently provide. Study of such minute tremor activity may provide additional insight on the nature of tremor generation that is not supported by the catalogues employed here.

2.5 Conclusion

In this study, we develop a catalogue of 896 tremor episodes by combining two long-term continuous catalogues of tectonic tremor in N. Cascadia. Episodes represent spatial-temporal clusters of tremor events and range in size from less than a dozen tremor events to more than 13,000. Major episodes, typically referred to as ETS events, consist of 64% of all tremor events but make up only 4% of episodes. At most locations, major episodes recur every 10.5–15.5 months, similar to recurrence interval estimates from previous work, but with standard deviations between 40 and 200 days, which indicates greater irregularity in the occurrence of ETS than the 40–60-day estimates given in previous work (Brudzinski and Allen, 2007; Kao et al., 2009).

Minor episodes (i.e., inter-ETS events) are nearly ubiquitous along the margin but are not distributed uniformly. Locations with relatively few minor episodes include mid-Puget Sound and the boundary between S. Vancouver Island and mid-Vancouver Island. Some locations only exhibit minor episodes in a certain size range (i.e., number of events per episode); for instance, eastern S. Vancouver Island primarily hosts minor episodes of intermediate sizes. Heterogeneity in the size and spatial distribution of minor episodes demonstrated in this study reveals persistent variability in tremor-genic processes throughout N. Cascadia on a 10-km scale that is not available from analysis of major episodes alone.

Using approximate Moho depths in Washington and S. Vancouver Island (McCrory et al., 2014) and a subducting slab model (Bloch et al., 2023), we show that the FMC is a dominant control of the occurrence of tremor along dip during major and minor episodes. Specifically, tremor during minor episodes concentrates down-dip of the FMC and tremor during major episodes concentrates up-dip, resulting in bimodal distributions of tremor along dip. In cases where the FMC is located near the down-dip limit of the ETS zone rather than in the middle, major and minor episode activity is colocated, resulting in unimodal tremor distributions along dip. Bimodality of tremor representing spatial segmentation of major and minor episodes along dip delineated by the FMC has been demonstrated to a limited degree in southwest Japan (Obara et al., 2010; Sawaki et al., 2021); here we show that the association between the FMC and along-up heterogeneities in tremor occurrence persists across the N. Cascadia region as the location and depth of the FMC varies.

Our extensive catalogue of tremor episodes is particularly well-suited to reexamining earlier findings that suggested short recurrence intervals and low forearc Vp/Vs result from the same fluid-facilitated processes (Audet and Bürgmann, 2014). Using regional 3D tomographic velocity models (Savard et al., 2018; Merrill et al., 2020), we find that recurrence intervals of tremor episodes throughout N. Cascadia are not correlated with forearc Vp/Vs, contrary to previous findings. We conclude that, while regionally-averaged forearc Vp/Vs may be correlated with recurrence intervals of major episodes (i.e., ETS events) across SZs around the world (Audet and Bürgmann, 2014), intra-regional and along-dip variations of forearc Vp/Vs are not correlated with recurrence intervals representing the full range of tremor episodes within N. Cascadia.

Chapter 3

Tackling the challenges of tectonic tremor localization using differential traveltimes and Bayesian inversion

Abstract

Episodic tremor and slip events in N. Cascadia produce low-frequency, emergent seismic signals, often referred to as tectonic tremor. Methods designed to locate tremor face two challenges that increase the likelihood of producing low quality catalogues: first, signal arrival and duration are often poorly defined; second, high rates of tremor activity during episodes can cause multiple signals to be indiscernible from each other. In this paper, we present a new method of locating tectonic tremor using differential traveltimes from a waveform-envelope cross-correlation in a grid-based Bayesian inversion. To address the aforementioned challenges, we use a recently-developed three-dimensional shear wave model to compute traveltimes, and include processes to remove data outliers, estimate data error statistics, and quantify uncertainties within the Bayesian framework. Although this method is designed for tremor, to test the approach we first consider a set of 58 local earthquakes between magnitudes -0.07 and 2.6 in the S. Vancouver Island region and obtain well-constrained relocations. Residuals between official catalogue values and our relocations are quantized with respect to the 1 km grid resolution of the inversion, and average 2.7 km in epicentre and 5.2 km in depth. Analysis shows that depths of relocations are sensitive to horizontal variations and simplifications in velocity models. We then present our catalogue of tremor events during the 2004 episodic tremor and slip event beneath S. Vancouver Island, Canada. Median uncertainties of tremor events quantified by 95% credibility interval widths in a 1 km grid are 5 km and 9.5 km in horizontal and depth directions, respectively (1.2 km and 2.3 km using traditional standard deviation-based uncertainties). Comparison of our catalogue with previously published work demonstrates that our new method yields a good detection rate, a greater degree of epicentral clustering, and better depth

resolution of tremor events. Catalogues produced using this new method may help to provide insight into the spatial extent of tremor, especially in depth, by yielding enhanced constraints on source locations on a regional scale.

3.1 Introduction

The Cascadia subduction zone (SZ) hosts quasi-periodic episodic tremor and slip (ETS) events that are characterized by low-frequency seismic signals and transient crustal deformation thought to originate from a conditionally-stable portion of the subduction fault. ETS seismic activity includes tremor-like events appearing as a semi-continuous signal distinct from environmental noise by its slightly increased amplitude over 10s of seconds or minutes in the 1-10 Hz frequency band. A seismogram displaying tremor shows no clear phase arrivals, but rather a gradual increase and decrease in amplitudes. Most tremor location methods use simplified information extracted from the seismogram, such as envelope functions, in a cross-station cross-correlation (CC) routine to obtain differential traveltimes (DTTs) between pairs of stations (Obara, 2002; Wech and Creager, 2008; Ide, 2010); others use back-projection methods (Kao and Shan, 2004; Haney, 2014; Li et al., 2017). Such methods rely on the obvious time-varying change of amplitudes across regional networks and can therefore be computationally efficient enough for daily monitoring, producing catalogues of tens of thousands of events (Wech, 2010). Depth resolution of N. Cascadia tremor catalogues varies from non-existent (Wech and Creager, 2008) to reasonably well-constrained (La Rocca et al., 2010; Ducellier and Creager, 2022), but with the latter generally only possible to date with temporary deployments of high-density arrays.

One of the inherent challenges in earthquake localization, including that of tremor, is the disambiguation of signals originating from spatially-distinct events during high rates of activity. This can produce intercalated signals, making them difficult to parse and to associate with sources. This inherent limitation is often exacerbated in tremor location methods by imprecise definitions of tremor signal arrival and duration, causing missed or false detection and leading to contaminated datasets. To improve localization results given these challenges, the method we present uses a recently-developed 3D velocity model, outlier controls, data error estimates, and probabilistic uncertainty quantification on source locations.

In this paper, we present a new method for locating ETS tremor by inverting DTTs in a Bayesian inversion, hereafter called the differential traveltime Bayesian inversion (DTBI) method. This method uses the source scanning algorithm (SSA; Kao and

Shan, 2004) for detection, a navigated waveform-envelope CC to construct a dataset of DTTs, the maximum intersection technique (MAXI; Font et al., 2004) to identify data outliers, and a grid-based Bayesian inversion to compute the 3D posterior probability distribution (PPD) of event source locations using a maximum-likelihood estimate of data error statistics. This method is tested on a catalogue of 58 local earthquakes in the S. Vancouver Island region throughout 2019, and results are analyzed with respect to crustal velocity structure, with particular attention to source depths. We then present a new catalogue of the 2004 ETS event beneath S. Vancouver Island and compare the results to the tremor catalogue presented in Kao et al. (2009).

3.2 The DTBI Method

3.2.1 Study Area and Data Processing

The study area of S. Vancouver Island (red polygon in Figure 3.2.1) is discretized into a 1 km cubic source grid. A propagation grid and 3D shear wave velocity model from Savard et al. (2018) encompassing the study area and seismic network are used in PyKonal's (White et al., 2020) 3D ray tracing point-source solver to compute traveltimes for direct shear waves between all nodes in the study area and all receivers at 1 km cubic spacing. Horizontal (EW and NS) components of all broadband seismometers and geophones, shown in Figure 3.2.1, provide seismic data from the Canadian National Seismograph Network (CN) maintained by Natural Resources Canada (NRCan), the Pacific Northwest Seismic Network run by the University of Washington (UW), the Pacific Boundary Observatory Borehole Seismic Network (PB) operated by the University NAVSTAR Consortium (UNAVCO), the Canadian Seismic Research Network (C8), and the Portable Observatories for Lithospheric Analysis and Research Investigating Seismicity (POLARIS) array (PO). Complete station lists are given in Appendix B as Tables B.0.1 and B.0.2. Tremor signals are dominantly composed of horizontal particle motion (Kao et al., 2006), and we find that identifying tremor signals using P-wave traveltimes on vertical components yields more noise than useful data given our current seismic data processing methods.

Daily continuous waveform recordings are resampled to 50 Hz, linearly detrended, and filtered using a fourth-order Butterworth band-pass filter with corner frequencies at 1.5 and 8 Hz. Tremor signals contain diminished energy in frequencies greater than 10 Hz (Kao et al., 2009; La Rocca et al., 2005) and environmental noise heavily dominates the seismograms below 1 Hz, so corner frequencies are chosen to place the roll-off of the filter strategically in these ranges. One-hour segments are normalized by the median of their absolute amplitudes to scale the waveforms to their approximate level

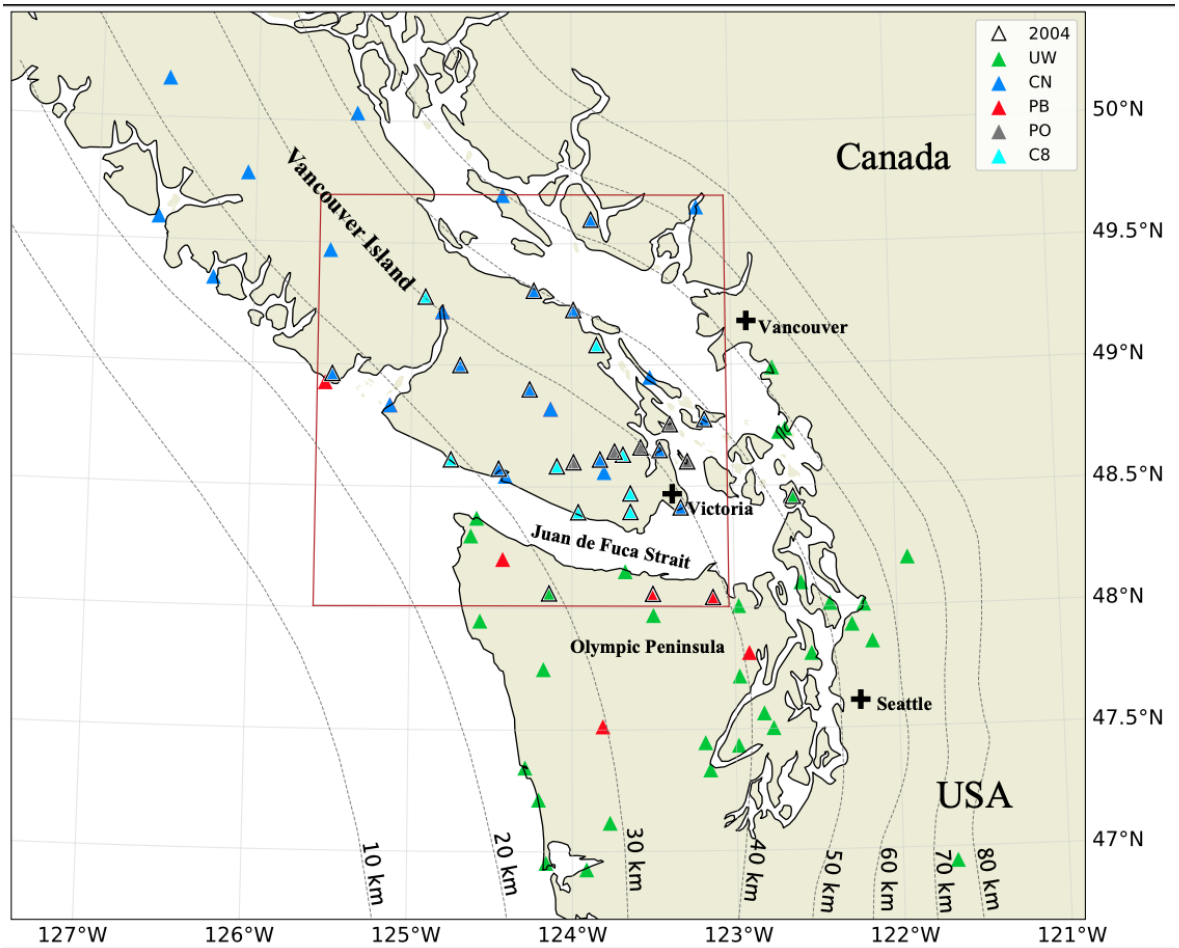

Figure 3.2.1: Regional map of S. Vancouver Island in N. Cascadia. The study area is outlined by the red polygon and seismic stations used in this study are shown as coloured triangles. Stations used in tremor localization of the 2004 ETS event are indicated by a black outline. Grey dashed lines show depth contours of the surface of the subducting JdF slab according to McCrory et al. (2012).

of noise. Segments with very low median values likely contain large data gaps and are removed from analysis.

The DTBI method consists of three main processes discussed in the following sections and outlined in the flow chart in Figure 3.2.2.

1. Detection: the study area is scanned at low spatial and temporal resolution to detect approximate times and locations that are associated with relatively large seismic amplitudes across the network.

2. Dataset construction: the seismograms containing signal from a detection are used in a network-wide waveform-envelope CC procedure to construct a dataset of DTTs. The MAXI technique (Font et al., 2004) is used to assess coherence of

the dataset and remove outliers.

3. Localization: A grid-based Bayesian inversion at higher spatial resolution is applied to the dataset to determine the spatial PPD that represents the source location and its uncertainty.

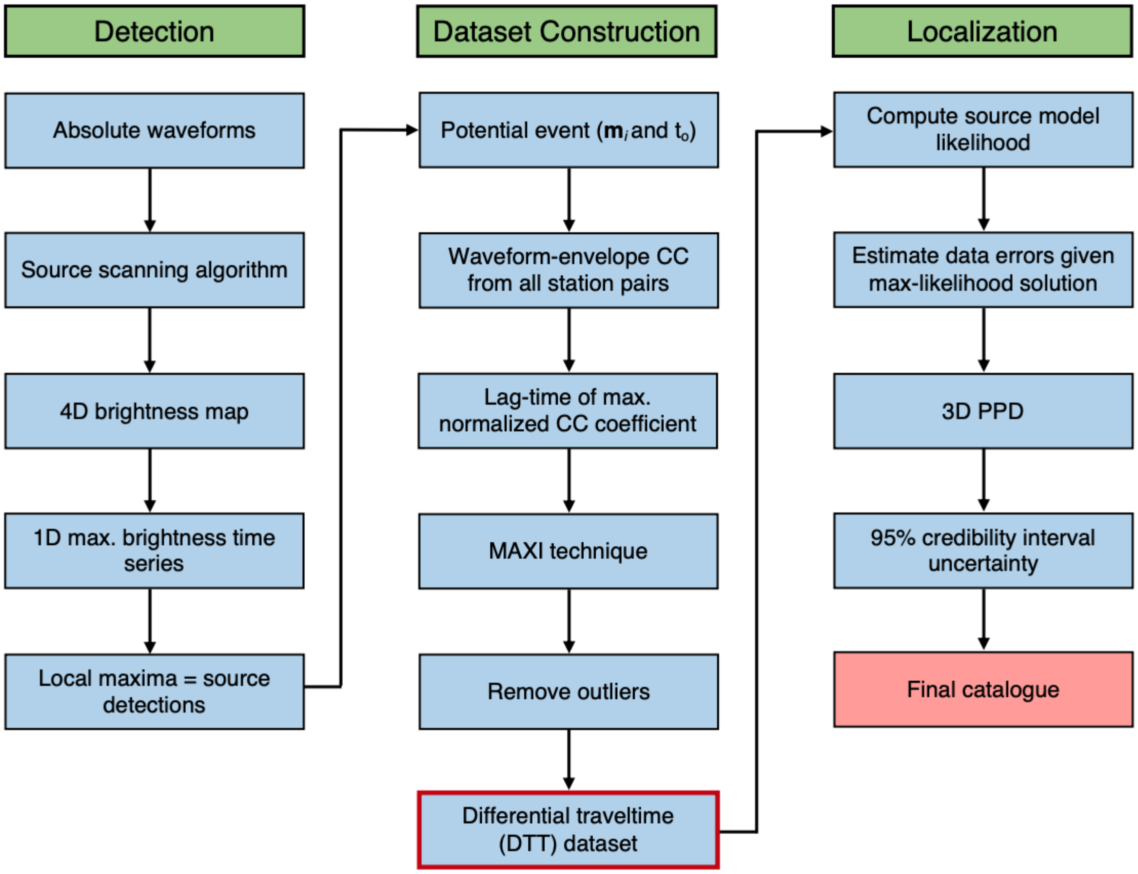

Figure 3.2.2: Flow chart of the DTBI method outlining the three main processes. First, the SSA is used to scan the study area for times and locations that correspond to relatively large amplitudes to yield event detections. Second, waveform envelopes from each detection are cross correlated between all station pairs in the seismic network, and a dataset of DTTs is constructed and curated. Finally, a Bayesian inversion computes the 3D PPD, and the solution is catalogued.

3.2.2 Detection: Source Scanning

The first process in the DTBI method is a simple version of the SSA originally developed by Kao and Shan (2004), which scans the four-dimensional model space to detect source locations and times that are associated with large amplitudes. Processed NS- and EW-component seismogram time series $N_j(t)$ and $E_j(t)$, respectively, from all n receiver stations ($j = 1, ..., n$) are combined using the Pythagorean relationship to produce a single time series $s_j(t)$ for each station, defined as

$$s_j(t) = \sqrt{E_j(t)^2 + N_j(t)^2}. \tag{3.1}$$

A scalar value, referred to as "brightness", is computed using amplitudes in $s_j(t)$ associated with a spatial node and origin time through back propagation of S-waves using pre-computed traveltimes T. Brightness is used as a proxy for the level of seismic activity at each location and time. Given $\mathbf{m}$ as the set of three-coordinate position vectors of model nodes, the brightness at node $\mathbf{m}_i$ over origin times t_o is calculated by

$$B(\mathbf{m}_i, t_o) = \sqrt{\frac{1}{w}\sum_{k=0}^{w-1} A^2(\mathbf{m}_i, t_o, k)}. \tag{3.2}$$

$A(\mathbf{m}_i, t_o, k)$ is the average stacked absolute waveforms of seismograms in $s_j(t)$ containing w samples, defined by

$$A(\mathbf{m}_i, t_o, k) = \frac{1}{n}\sum_{j=1}^{n} \left| s_j\left(t_o + T_{ij} + k - \frac{w}{2}\right)\right|, \tag{3.3}$$

where T_{ij} is the traveltime between node i and station j. A search over N_m model nodes and time intervals results in a 4D brightness map. In application to tremor, the brightness map is the result of searching origin times at 5 s intervals using seismogram windows of 15 s (i.e., 2/3 window overlap) and every fourth grid node in the study area (i.e., 4 km grid spacing).

At each origin time, the model node with the maximum brightness value is considered to be the most likely to contain a seismic source. As such, a 1D brightness time series, $R(t_o)$, is constructed by selecting the maximum brightness at each time step, defined as

$$R(t_o) = \max_{i=1,\ldots,N_m} \left\{ B(\mathbf{m}_i, t_o) \right\}. \tag{3.4}$$

An example of $R(t_o)$ is illustrated in Figure 3.2.3b with accompanying waveforms from a station shown in Figure 3.2.3a. All nodes and times corresponding to local maxima in $R(t_o)$, indicated by red circles in Figure 3.2.3b, are flagged as event detections. A local maximum represents the approximate origin time corresponding to amplitudes that are both relatively large and congruous across the seismic network, although spurious or artificial signals with extremely large amplitudes may cause erroneous detections. Additional processes described later in this paper are designed to identify and terminate the localization of such false detections. Note that $R(t_o)$ represents seismic activity as a function of origin time whereas a seismogram is a function of arrival time. The time difference between a local maximum in $R(t_o)$ and the corresponding heightened amplitude at any given station is the theoretical traveltime between the detected source and that receiver. The time in $R(t_o)$ associated with any detection is the origin time that may eventually be catalogued.

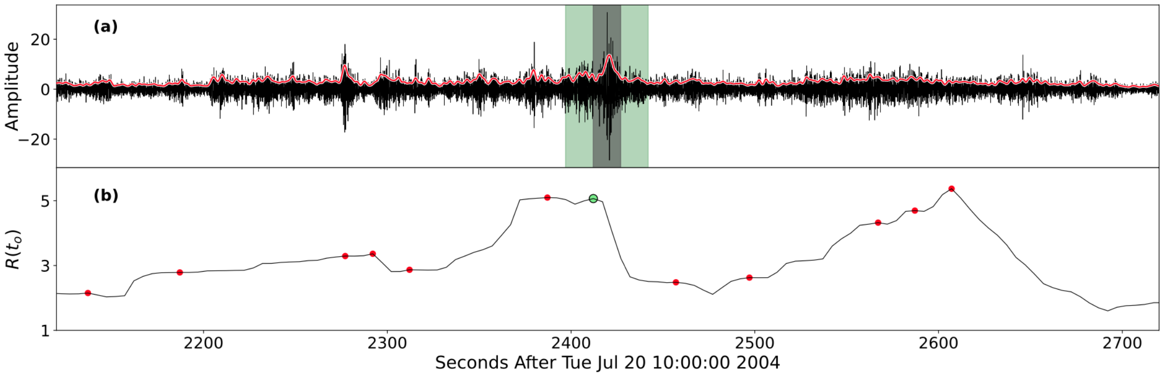

Figure 3.2.3: (a) Ten minutes of processed EW-component seismic data (black) from station TWBB and the corresponding lowpass-filtered envelope (red line). The grey shaded region denotes the 15 s window used by SSA to make this detection, and the green shaded region denotes the 45 s window associated with this detection used in the network-wide CC process. (b) Maximum brightness time series $R(t_o)$ (black line) derived from the 4D brightness map produced by SSA using the entire seismic network. Green and red circles represent local maxima and thus event detections. The green circle denotes the detection of the event whose signal is highlighted in (a).

There are two related limitations to the detection process resulting from the interpretation of the brightness map. First, $R(t_o)$ only includes one brightness value per time step — the maximum brightness over source locations. This necessarily excludes local maxima, which may be brightness values corresponding to other events occurring around the same time. In addition, only local maxima of $R(t_o)$ are flagged as detections. This means that events associated with lower brightness occurring in time steps before or after a brighter event may be over shadowed in $R(t_o)$ and may not therefore result in a detection. Both limitations potentially result in fewer detections of real events and are partially modulated by the size of the time step, so the SSA should be parameterized with these issues in mind.

3.2.3 Dataset Construction

Each detection is used to construct a dataset that may later be inverted for source location. Dataset construction requires two steps: one to derive the data and another to remove outliers and assess the coherence of the set. The first step is carried out using a waveform-envelope CC and the second step uses the MAXI technique (Font et al., 2004).

Waveform-Envelope Cross-Correlation

The first step in the dataset construction process is a waveform-envelope CC that produces DTTs between station-pairs with highly-correlated signals.

The envelope of processed seismograms is computed using a Hilbert transform, lowpass filtered at 0.3 Hz, and downsampled to 10 Hz. The DC offsets of 45 s enveloped CC windows are removed and the edges are tapered using a 5% cosine-tapered window function. For each detection, enveloped windows centred on the expected arrival at two stations are cross-correlated between all station pairs. The normalized CC function $C(\tau)$ of envelopes ε containing n' samples from stations j and p as a function of lag time τ is defined by

$$C_{jp}(\tau) = \frac{\sum_{k=1}^{n'} \varepsilon_j(k)\ \varepsilon_p(k-\tau)}{\left[\sum_{k=1}^{n'} \varepsilon_j^2(k)\ \times\ \sum_{k=1}^{n'} \varepsilon_p^2(k-\tau)\right]^{\frac{1}{2}}}. \tag{3.5}$$

EW- and NS-component seismograms are cross-correlated independently. Figure 3.2.3a shows ten minutes of processed seismogram (black line) and its filtered envelope (red line). The green shaded region is an example a CC window containing the signal envelope from the detection denoted by the green circle in Figure 3.2.3b.

CC here serves two functions: (1) to identify which windows are highly correlated, by which we can infer that signal related to the seismic event in question may be present in the windows; and (2) to identify the relative times at which pairs of windows are maximally correlated (i.e., identify the lag time of the signal), by which we can infer the arrival-time differences between pairs of stations. Note that the arrival-time difference between two stations from a single event is equal to the traveltime difference from the event source to the stations. If enveloped windows from two stations j and p are sufficiently correlated within some time range, the DTT d_{jp} between them from a detected location $\mathbf{m}_i$ is defined by

$$d_{jp} = T_{ij} - T_{ip} + \tau'_{jp}, \tag{3.6}$$

where τ'_{jp} is the lag-time of the maximum normalized CC coefficient. Note that d_{jp} is independent of both origin time and the absolute arrival time of signals at either station. Tremor signals do not have clear phase arrivals, so the inherent independence of DTTs from phase arrival picks is a distinct advantage for tremor localization. The maximum possible lag time between two stations corresponds to the slowest velocity in the model and the case where the epicentre and both stations are in a straight line. As such, the maximum allowable lag-time of peak correlation for any particular station pair is a function of the distance between them.

DTTs must have a maximum normalized CC coefficient above a pre-set threshold to be considered in future processes. This threshold is determined by performing a CC of 50,000 randomly-selected 45 s enveloped windows from randomly-selected station pairs. According to the Central Limit Theorem, the distribution of the normalized coefficients of this random sampling closely approximates a zero-mean Gaussian distribution, and the coefficient threshold is set to three standard deviations above the mean of this distribution. Since random sampling is derived directly from the seismic data, this threshold is computed separately for each hour. In this study, the normalized CC coefficient thresholds range from approximately 0.65 to 0.72, often corresponding to when tremor activity is low and high, respectively. Finally, we require that any station may not be greater than 120 km from the detected epicentre to reduce the inclusion of DTTs from mantle-interfering raypaths, and that the two stations in a pair may not be separated by more than 100 km from each other to reduce the inclusion of coincidental and erroneous DTTs.

The CC process produces a dataset that contains observed DTTs between all highly-correlated windows. Since the detection process described in Section 3.2.2 provides times and locations likely to contain seismic sources, the dataset likely includes DTTs directly related to the detected event, but this does not exclude DTTs related to other phenomena; any signal that is congruous across two or more stations may contaminate the dataset. For example, station pairs with small inter-station separations (generally < 5 km) may be correlated regardless of the nature or location of the seismic source(s). The CC may also yield heterogenous datasets when two or more events have occurred sufficiently close in space and time. Consider spatially-distinct events A and B occurring sufficiently close in time such that some signal from both events are included in CC windows at most stations. The DTTs from some station pairs may represent event A while those from other pairs may represent event B, leading to a heterogenous dataset containing *intra*-event DTTs. It is also possible for signals from A to be correlated with signals from B, leading to a heterogenous dataset containing *inter*-event DTTs. In either case, such heterogenous datasets can sometimes be avoided by allowing for the detection of multiple simultaneous sources, as is possible using back-projection methods. However, it is still possible for back-projected signal segments from two different sources to be spatially coalescent at one location (McBrearty et al., 2019). This problem is inherent in any method that aims to associate a set of observed signal segments or arrival times with a set of (unknown) sources and is commonly described as the phase association problem (Johnson et al., 1997). This problem is increasingly impactful during high rates of seismic activity, such as during aftershock sequences or, as is the case here, during ETS. In addition to the inherent ambiguity related to the phase association problem, the use of moderate-duration windows can add further ambiguity by the possible inclusion of inter- and intra-event DTTs in a dataset. We therefore apply spatial constraints to the dataset in order to identify possible outliers and remove them, thereby mitigating dataset heterogeneity, before localization. Here, we use a modified version of the MAXI technique developed by Font et al. (2004) to remove outliers that may reasonably be considered unrelated to the tremor event without assuming the error distribution of the dataset.

Maximum Intersection of Equal Differential-Time Surfaces

After an initial DTT dataset is constructed, a modified version of the MAXI technique is used with weighted residuals to estimate the source location and subsequently remove outliers. While this procedure yields a source location as well as a quality assessment of the solution, it does not provide a statistically-meaningful uncertainty estimate or spatial distribution of probability. Therefore, this step is only used to remove outliers and estimate dataset coherence; a subsequent Bayesian inversion is applied to the curated dataset, as described in Section 3.2.4.

The MAXI technique computes the grid node at which the maximum number of equal differential-time (EDT) surfaces intersect by assessing every fourth node in the study area (i.e., 4 km grid spacing). Each DTT value corresponds to a surface in 3D space — the EDT surface — that contains all associated source locations. In theory, EDT surfaces have zero thickness; however, in practice, DTTs are assigned a finite time range, within which they are considered to apply in order to accommodate reasonable approximations and errors from all previous procedures, thereby turning each surface into a layer. ETD layers are constructed using both observed DTTs, which determine locations of EDT *surfaces*, and theoretical DTTs associated with a given node, upon which the thickness of the ETD layer depends. In other words, the thickness of EDT layers is a function of the residuals between observed and theoretical DTTs associated with a given node. An example of three EDT layers of varying thicknesses is shown in Figure 3.2.4.

The MAXI technique constructs all EDT layers associated with each model node in the study area for a given dataset. For example, if a given node is close to the actual source, the residuals should generally be small and the EDT layers will be correspondingly thin, but they may also vary due to measurement and theory errors. A

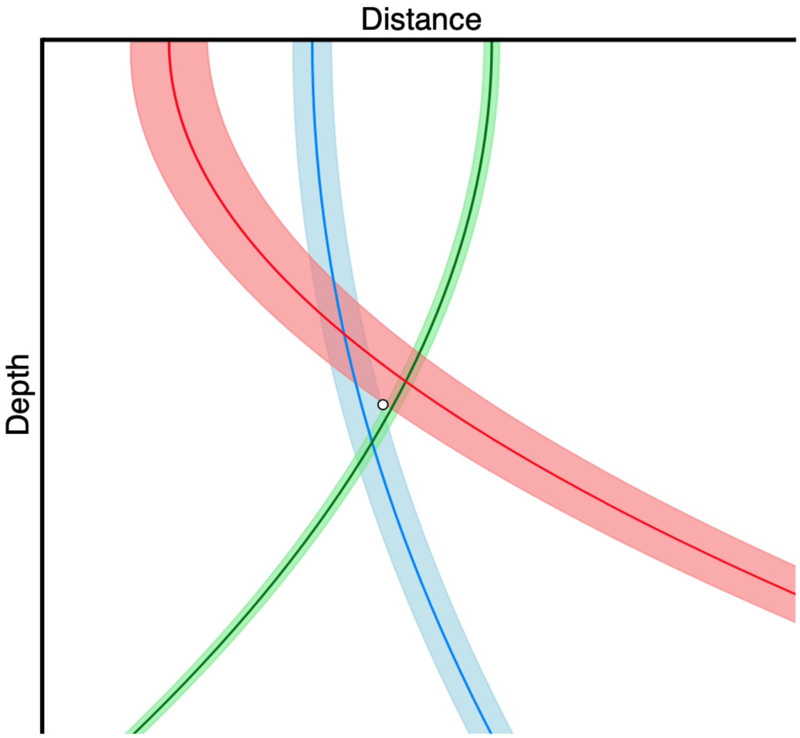

Figure 3.2.4: A cartoon showing three EDT layers associated with a single node. EDT surfaces (solid lines) are extrapolated into layers (shaded regions) with thicknesses defined by the magnitude of the DTT residuals at the given node (black open circle). Each of the intersecting layers is assigned a predetermined integer weight, which is inversely related to its thickness, that contributes to the MAXI value of the node. In this example, the green layer contributes the greatest weight and the red contributes the lowest. The weighting scheme is defined in Table 3.2.1.

traditional minimization procedure would sum the squared residuals at each node and then identify the node with the smallest sum as the source. However, because such a process uses the magnitude of residuals, the resulting sum is sensitive to large outliers. The MAXI technique avoids undue influences from outliers by using a weighting scheme — a greater weight is assigned to residuals with smaller magnitudes, that is, thinner layers. As such, this process represents a weight maximization rather than a residual minimization. The weight of a given residual is determined by a weighting scheme defined for multiple residual time-ranges, summarized in Table 3.2.1. Absolute residuals within the specified ranges are assigned an equal weight, thereby avoiding the proportionally larger influence from larger residuals. The design of this weighting scheme, such as the total range of the residuals, how many weighted bins to use, and the ranges associated with each bin, are methodological choices that may depend on the type of data used and the nature of the problem, and can be altered for different desired outcomes. In this study, the allowable ranges of EDT layer residuals was determined through trial and error to remove likely outliers but prevent the removal of good data; for regional tremor applications, the density and number of stations in the seismic network are the largest factors that influence the tolerance of residuals.

Table 3.2.1: Allowable time ranges for absolute residuals and the corresponding weight added to the MAXI value of a given node.

Absolute Residual (s)	Weight
[0.0, 0.3]	5
(0.3, 0.6]	4
(0.6, 1.2]	3
(1.2, 2.1]	2
(2.1, 3]	1
(3, ∞)	0

After computing MAXI values at every fourth model node for all DTTs in the dataset, the node corresponding to the maximum value, denoted M, is considered the preliminary location solution and is used to estimate which DTTs are outliers using the following conditions: (1) any DTT with an EDT layer intersecting the preliminary node with an associated weight < 2; and (2) any DTT for which the traveltime from the preliminary location is more than 3 s shorter for the farther station in the pair. Condition (2) is adopted from the tremor location method developed by Ide (2010) and takes advantage of the expectation that source-to-receiver traveltimes are usually longer for receivers that are farther; however, to allow for the possibility of particular raypaths and velocity structures that could yield traveltimes that defy this expectation, and to allow for other possible errors, we permit the traveltime at the farther station to be a maximum of 3 s shorter than at the closer station between any given pair. Any DTT that meets either condition is considered an outlier and is removed from the dataset. Using the remaining DTTs, the quality of the preliminary location is assessed by

$$Q = \frac{M}{\text{maximum possible MAXI value}} \equiv \frac{M}{5 \times (\text{number of DTTs})}. \tag{3.7}$$

Q can vary between 0 and 1. $Q < 0.5$ is taken to terminate the process with the implication that the dataset has low coherence and a well-localized solution does not exist. When $Q = 1$, the coherence of the dataset is high; all EDT layers intersect the preliminary node with associated weights equal to 5. However, in regional applications, a densely-spaced cluster of stations alone may produce a dataset with maximum coherence across multiple nodes. This is because traveltime differences between closelyspaced stations are small at every node in the search grid and therefore provide little meaningful resolution. In such cases, the MAXI technique cannot determine a global maximum and a preliminary source node cannot be resolved. In this study, a dataset must include at least 30 DTTs from at least 8 seismic stations after removing outliers, while limiting the use of clusters (< 1 km separation) to two stations (at most one DTT) per cluster. A dataset meeting these conditions is used in the subsequent localization process.

3.2.4 Localization: Bayesian Inversion

The final process uses the curated DTT dataset in a Bayesian inversion to construct a 3D PPD for the seismic source location in a 1 km cubic source grid.

A Bayesian solution to the inverse problem is the probability of a model given data and prior knowledge about the model itself. In this approach, prior knowledge is updated by new data information. Bayes' rule can be stated as follows:

$$P(\mathbf{m}|\mathbf{d}) = \frac{P(\mathbf{m})P(\mathbf{d}|\mathbf{m})}{P(\mathbf{d})}, \tag{3.8}$$

where $P(\mathbf{m})$ is the prior probability of the model $\mathbf{m}$, $P(\mathbf{d}|\mathbf{m})$ is the conditional probability of the data $\mathbf{d}$ given $\mathbf{m}$, $P(\mathbf{d})$ is the unconditional probability of $\mathbf{d}$, and $P(\mathbf{m}|\mathbf{d})$ is the PPD of $\mathbf{m}$ given $\mathbf{d}$. We will describe the application of each term to this inversion individually.

We use a uniform prior within the study area and 0 outside the study area, which is to say, no prior knowledge is used to favour one model node over any other within the bounds of the study area. The prior probability at all N_m model nodes is

$$P(\mathbf{m}) = \frac{1}{N_m}, \tag{3.9}$$

such that $\sum_{i=1}^{N_m} P(\mathbf{m}_i) = 1$.

In this study, the error distribution of the data, including both measurement and theory errors, is unknown. Hence, for simplicity, data errors are assumed to be due to an independent, identically-distributed Gaussian random process with an unknown standard deviation σ. In this case, the conditional probability of the data can be written

$$P(\mathbf{d}|\mathbf{m}) = \frac{1}{(2\pi)^{\frac{N_d}{2}}\sigma^{N_d}} \exp\left[-\frac{1}{2\sigma^2}\left|\mathbf{d} - \mathbf{d}(\mathbf{m})\right|^2\right], \tag{3.10}$$

where $\mathbf{d}$ and $\mathbf{d}(\mathbf{m})$ are the observed and predicted data, respectively, with N_d data.

When interpreted as a function of $\mathbf{d}$, equation 3.10 is the probability distribution of the data; however, for fixed observed data it can be interpreted as a function of $\mathbf{m}$, describing the likelihood of the model. The model node for which the likelihood is greatest is considered the maximum-likelihood solution $\hat{\mathbf{m}}$, that is, the node most likely to have produced the observed data $\mathbf{d}$, which is independent of σ. Hence, $\hat{\mathbf{m}}$ can be computed simply by minimizing $|\mathbf{d} - \mathbf{d}(\mathbf{m})|^2$ over the grid. We then derive an expression for σ by maximizing the likelihood with respect to σ and computing its value $\hat{\sigma}$ using $\hat{\mathbf{m}}$.

We denote the likelihood as $L(\mathbf{m}, \sigma)$ and maximize it with respect to σ, solving

$$0 = \frac{\partial L(\mathbf{m}, \sigma)}{\partial \sigma} \tag{3.11}$$

for σ, which, when evaluated at $\hat{\mathbf{m}}$, gives

$$\hat{\sigma} = \left[\frac{1}{N_d} |\mathbf{d} - \mathbf{d}(\hat{\mathbf{m}})|^2 \right]^{\frac{1}{2}}. \tag{3.12}$$

Substituting equation 3.12 into equation 3.10 for σ gives the likelihood over the entire model grid used in this inversion.

Bayes' rule describes $P(\mathbf{d})$ as the evidence, or the probability of the data irrespective of the model. We derive $P(\mathbf{d})$ as a constant from equation 3.8, expressed as

$$P(\mathbf{d}) = P(\mathbf{m}) \sum_{i=1}^{N_m} P(\mathbf{d}|\mathbf{m}_i) \; \equiv \; \frac{1}{N_m} \sum_{i=1}^{N_m} L(\mathbf{m}_i, \hat{\sigma}). \tag{3.13}$$

The final Bayesian expression for the PPD within the study area is the product of the likelihood and prior divided by the evidence, which becomes

$$P(\mathbf{m}|\mathbf{d}) = \frac{L(\mathbf{m}, \hat{\sigma})}{\sum_{i=1}^{N_m} L(\mathbf{m}_i, \hat{\sigma})}. \tag{3.14}$$

3.3 Results and Discussion

3.3.1 Local Earthquake Relocation

The DTBI method is tested against a suite of 58 local crustal and in-slab earthquakes with magnitudes M_L ranging from -0.07 to 2.6 beneath S. Vancouver Island and the JdF Strait from the NRCan catalogue during 2019; an event list is given in Appendix B (Table B.0.3). Events in the official catalogue were located by analysts using picked arrival times of P- and S-phases, whereas the fully-automatic DTBI method uses DTTs from CCs of S-wave envelopes, which, while applicable for tremor localization where phases cannot be picked, are expected to be less informative and less suited to earthquake localization. Nevertheless, this test provides important verification of the efficacy of the DTBI method. NRCan's routine earthquake location procedures use a regional 1D layered Vp model that is scaled by a uniform Vp/Vs ratio, and therefore Poisson's ratio (PR), to derive Vs when applicable (Figure 3.3.1a). Despite the fact that this simplification introduces errors in localization, we consider locations in the official catalogue to be the standard for the purpose of this study. We assess the sensitivity of the results on velocity structure by using both a smoothed 3D double-difference tomographic Vs model from Savard et al. (2018) and a regional 1D model derived from the Geological Survey of Canada (GSC) Vp model used by NRCan for routine earthquake localization shown in Figures 3.3.1a and b.

Compared with its configuration for tremor localization described in Section 3.2, the DTBI method was parameterized with some differences for earthquake localization, as follows. The filtering passband is widened to 1.5–20 Hz, the SSA detection window is shortened to 5 s, and the CC window is shortened to 20 s to reflect the typical frequency spectra and duration of small, local earthquakes. Consequently, the corner of the low-pass filter used on seismogram envelopes is increased to 0.7 Hz to allow more amplitude variation within shorter windows. The source location estimate for each event is taken to be the grid node that maximizes the PPD—the maximum *a posteriori* node—given by equation 3.14. The uncertainty on this estimate is quantified by the width of the 95% highest-probability density credibility intervals (CIs) of the marginal probability distributions in horizontal and vertical dimensions. With a 1 km search grid for the Bayesian inversion, the minimum possible CI width is 1 km, except when the PPD is truncated by the study area boundaries, where the minimum possible CI width is 0.5 km. The NRCan official catalogue does not provide uncertainties, but qualitative estimates indicate uncertainty intervals are approximately ±3 km in epicentre and ±5 km in depth (C. Brillon, private communication, 2022). It is important to note that our uncertainties quantified in terms of 95% CI interval widths are generally substantially larger than standard-deviation based uncertainties; for a Gaussian PPD the 95% CI is approximately 4 standard deviations wide. However, CIs can provide a more meaningful measure of uncertainty than standard deviations for significantly non-Gaussian PPDs, such as are sometimes observed here.

Using the 3D model, 35 of 58 events passed baseline requirements in the DTBI method. Since the DTBI method is designed with emphasis on accuracy and high resolution, it is expected that some number of events would not be catalogued. Of the events successfully relocated (M_L 0.05-2.6), most are in good agreement with the official catalogue; all NS and EW residuals between official and relocated events are ≤ 6 km and all but 4 depth residuals are < 10 km, as shown in Figure 3.3.2a. Since depth is often the most difficult parameter to constrain, it is not surprising that the range of depth residuals, with a median of 5.2 km, is larger than that of the NS and EW residuals, which have medians of -1.5 km and 0.1 km, respectively. Using the 1D model, 37 events were successfully relocated with a similar distribution of NS and EW residuals (Figure 3.3.2b), but 12 events are relocated with depth residuals ≥ 10 km, resulting in a median depth residual of 8.8 km.

Relocated events using both models are shallower than their official locations overall; however, this possible systematic trend is not present uniformly throughout the study area. Figure 3.3.3 shows official event locations, relocations, and error bars representing the extent of the marginal CIs in EW and depth dimensions (profile only). In general, the depths of relocations east of 123.75° W deviate more from their official locations (by a median of 5.7 km) than those to the west (by a median of 3.5 km). As shown in Figure 3.3.1c, the velocity structure of the study area east of $\sim$ 123.75° W exhibits strong vertical and lateral variations in PR, including high PR in the mantle wedge (> 0.27) and low PR in the forearc (< 0.21), that are not accounted for in the 1D model. Over two thirds of our relocations are in this region and, while this is part of the ETS zone, there is minimal overlap of areas where tremor and crustal earthquakes tend to occur most. Relocations east of 123.75° W using the 1D model, shown in the right panels of Figure 3.3.3, represent a more significant shallow trend as well as larger mean depth CIs (4.6 km) compared with 3D relocations (3.8 km) in this area. Savard et al. (2018)'s relocated catalogue computed during the tomographic inversion of the 3D velocity model used in this study (Figures 3.3.1b and c) yields relocations of forearc earthquakes east of 123.5° W shallower than NRCan locations overall, with mean depth residuals around 2 km. This indicates that using a simplified 1D velocity model could result in a deep bias when using traditional location methods and a shallow bias using the DTBI method, for earthquakes located in the southeastern part of the study area; specifically, it possibly could result in a deep bias for the former and a shallow bias for the latter. Using the 3D model serves to deepen relocations in the DTBI catalogue east of 123.75° W compared with using the 1D model, and, although it is beyond the scope

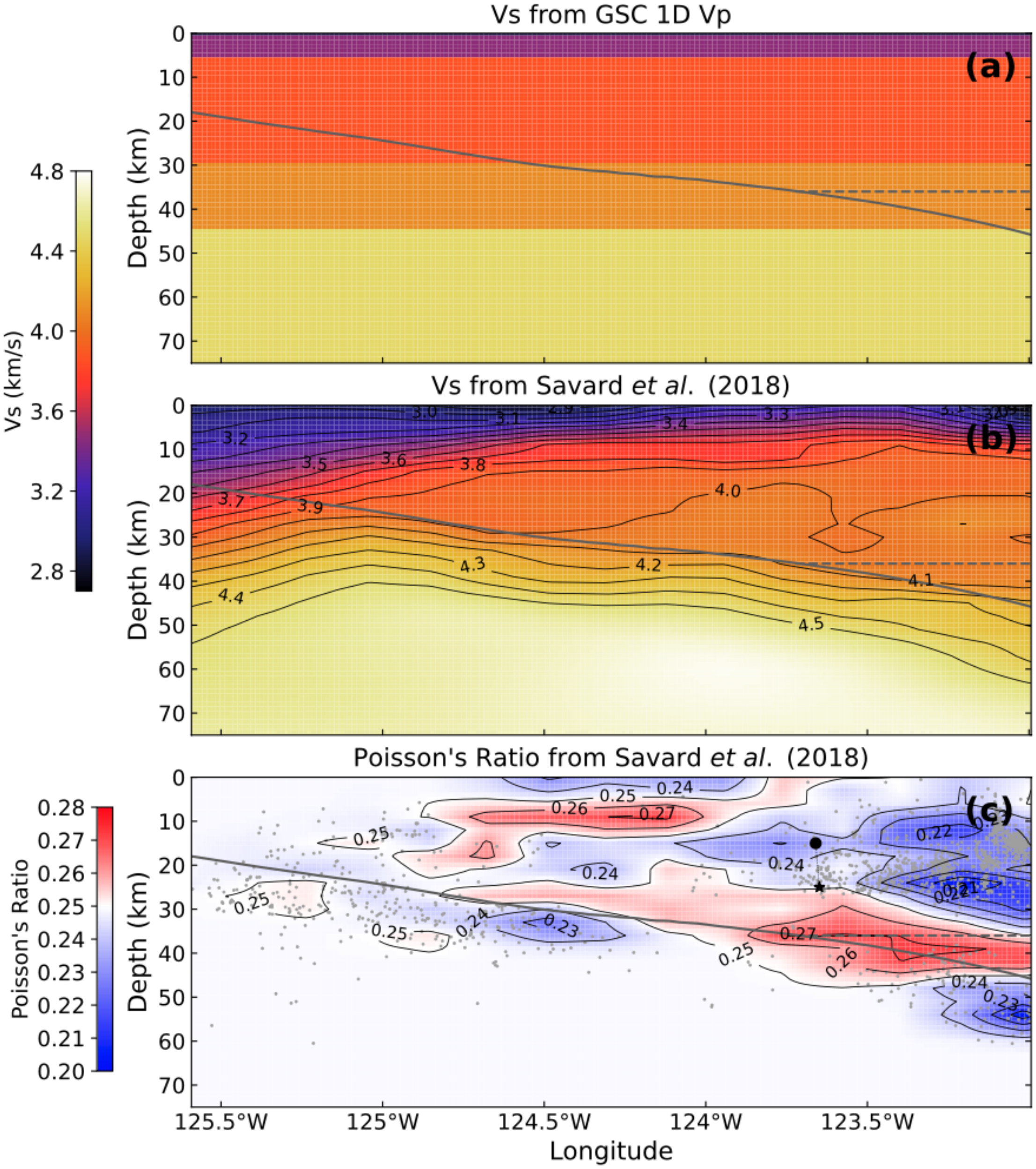
Vs from GSC 1D Vp

Vs from Savard *et al.* (2018)

Poisson's Ratio from Savard *et al.* (2018)

Figure 3.3.1: Two velocity models used in this study and variation in PR along 48.5° N. (a) 1D Vs model derived by scaling the regional GSC Vp model by a uniform Vp/Vs ratio of 1.73; (b) and (c) are depth slices through smoothed 3D Vs and PR models from Savard et al. (2018). PR is coloured by deviation from a value of 0.25 (corresponding to a Vp/Vs ratio of ~ 1.73). Grey dots in (c) represent background seismicity relocated during the tomographic inversion of Savard et al. (2018). Our relocation (black circle) of an earthquake (black star) is 10.0 km shallower than the NRCan location using the 3D velocity model in (b). The solid grey line in each panel represents the subducting plate interface from McCrory et al. (2012), and the dashed grey line approximates the location of the continental Moho at 36 km depth. No vertical exaggeration.

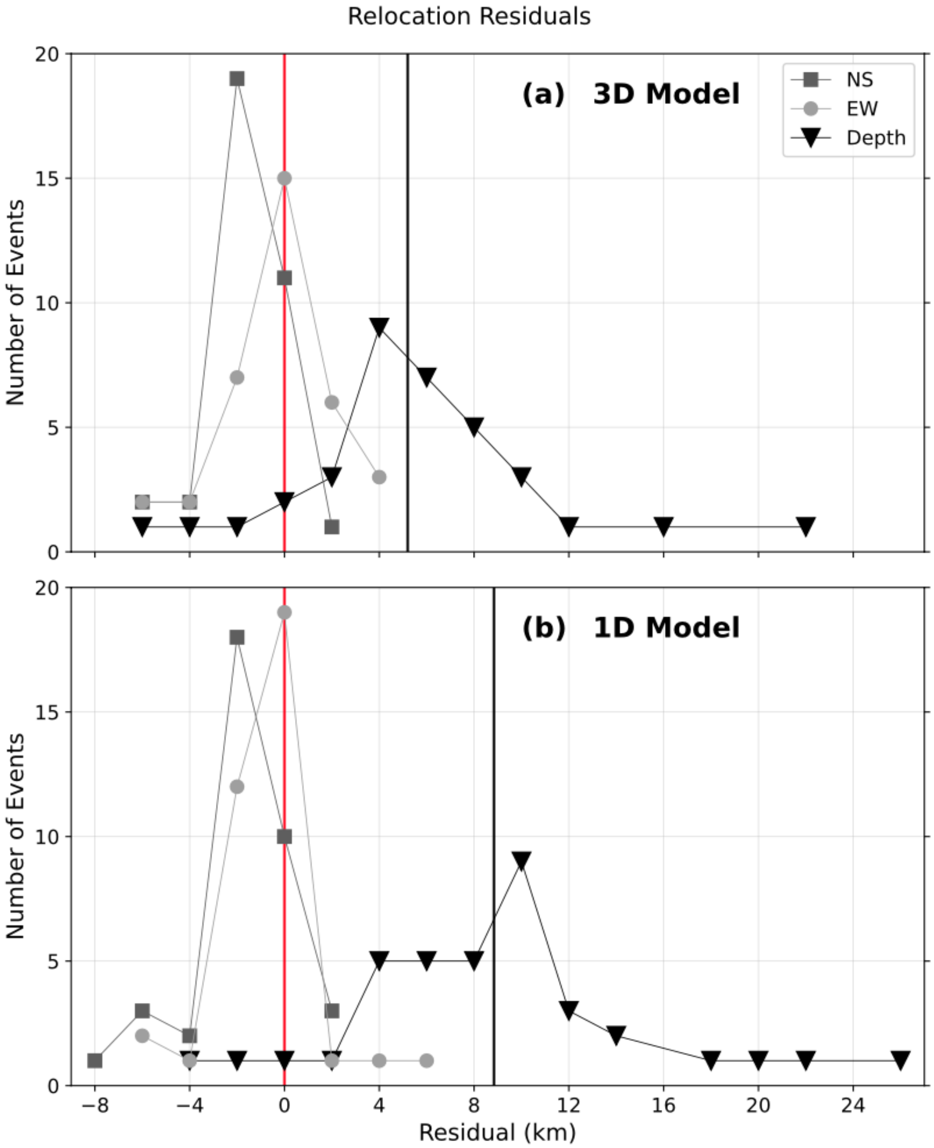

Figure 3.3.2: Histograms of NS, EW, and depth residuals between official and relocated events using (a) 3D and (b) 1D velocity models. Positive NS, EW, and depth residuals respectively indicate more southerly, more westerly, and shallower relocations. Median depth residuals using the 3D and 1D velocity models are respectively 5.2 km and 8.8 km, indicated by the black vertical lines. Red vertical line indicates 0 km for reference.

of this study, a possible deep bias in the NRCan catalogue may explain the remaining shallow depth residuals.

Waveforms corresponding to the event enclosed in a black rectangle in Figure 3.3.3 are shown in Figure 3.3.4. This event is chosen for additional analysis because it is one of the few relocations with a large depth residual (10 km) and small epicentral residual (1.7 km). The moveout of the signal from this event is arranged according

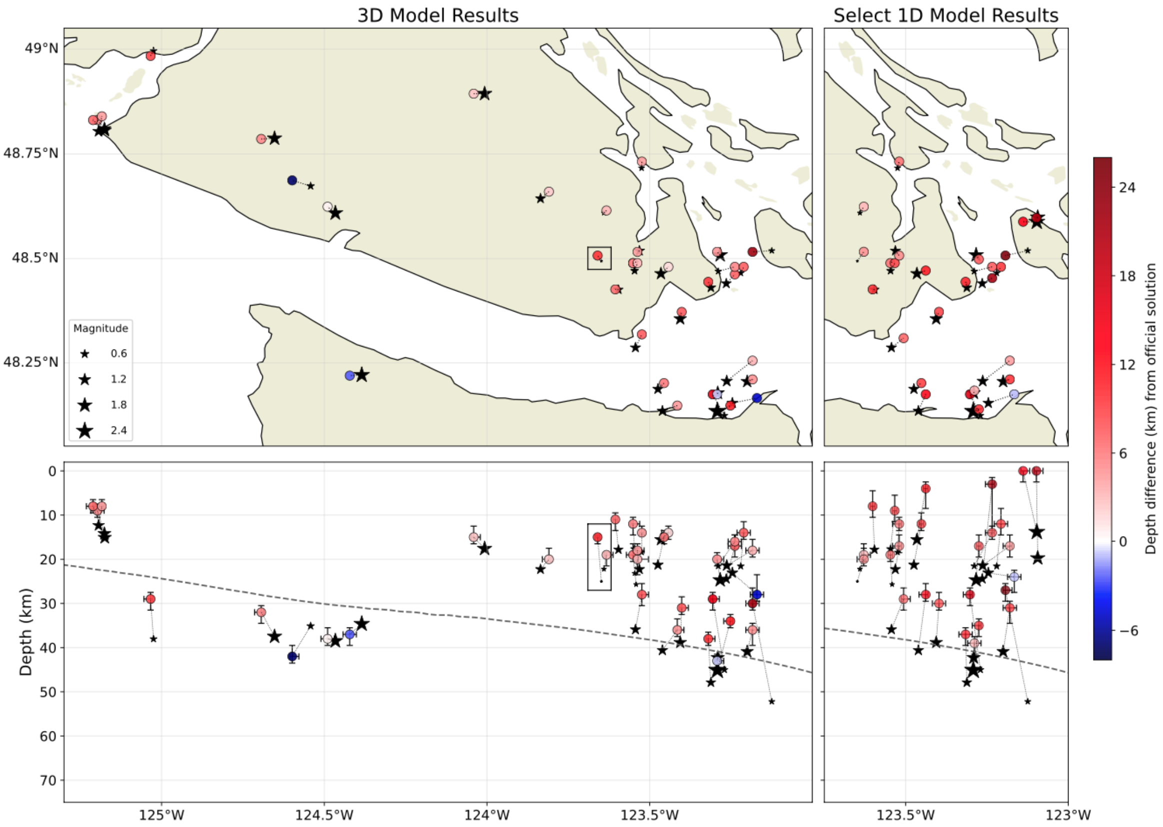

Figure 3.3.3: Map and profile of earthquakes located by official agencies (black and yellow stars) and relocated in this study (coloured circles) connected by dotted lines. Black stars are earthquakes that were not successfully relocated by the DTBI method. Relocations are coloured by their depth residual with respect to the official solution; blue and red indicate deeper and shallower relocations, respectively. Error bars represent the total width of the marginal 95% CI in EW and depth dimensions. Left panels show relocations using the 3D velocity model of Savard et al. (2018), and right panels show a selection of the relocations using the GSC 1D velocity model. Waveforms from event enclosed in the black polygon are shown in a later figure. The region in the right panels corresponds to an area of low PR in the continental forearc (Savard et al., 2018). The horizontal grey dashed line represents the plate interface from McCrory et al. (2012) interpolated longitudinally at 48.5° N. No vertical exaggeration.

to the location produced in this study, including CC windows of waveform envelopes used to compute 83 DTTs across 28 stations. Theoretical arrivals (magenta markers) from the relocated source correctly identify the largest amplitudes of the signal, which, for an event of this size, is often the S-phase. Cyan markers indicate the S-phase arrival picks from the NRCan archives used to locate this event (a subset of 20 P and S picks across 12 stations), and orange markers indicate the theoretical arrival from our relocated source assuming the same depth as the NRCan solution. The presence of P-phases within CC windows has little to no effect on calculated DDT values, because the greatest correlation values involve the largest amplitudes (i.e., S-waves). At greater source-to-receiver distances surface waves may produce larger amplitudes than S-waves, which is part of the reason we limit this distance to 120 km. The cause of the 10 km depth residual between the NRCan location and our relocation of the event highlighted in Figure 3.3.3 is not obvious after inspection of the waveforms in Figure 3.3.4. Artificially deepening the solution to match the depth in the official catalogue does not yield theoretical arrivals that appear more consistent with NRCan picks. The orange markers in Figure 3.3.4, representing arrivals from such a source, tend to arrive too late at stations closer to the source and too early at stations farther from the source. From this we may conclude that the main cause of the large depth residual is the different velocity models. Velocity gradients in the 3D model resulting from rheological discontinuities, such as the Moho and subduction interface, may cause raypath effects (e.g., turning rays) that are absent in raypaths computed using a layered model. Furthermore, we recognize that the crust may have variations in seismic velocities at scales and magnitudes that have been smoothed over or that are potentially not resolved in the inversion of Savard et al. (2018) and that may affect the relocation result.

Differences between our relocations and the official catalogue are expected, and we do not claim here that our results are more accurate. The DTBI method is not designed to extract high-precision data from seismograms that are often available from traditional earthquake signals (e.g., phase picks) because tremor does not readily provide such information. Rather this test demonstrates that CC of S-wave envelopes can produce large DTT datasets that yield source locations of microseismic events that are consistent with official catalogues. This test also demonstrates that simplified velocity models can introduce significant depth errors on source locations. Our method uses a 3D Vs model for the S. Vancouver Island region to mitigate such errors.

3.3.2 ETS Tremor Localization

In this section we illustrate the DTBI method for tremor localization by analyzing one tremor source in detail and then comparing our catalogue of the 2004 ETS event beneath S. Vancouver Island with that presented in Kao et al. (2009) computed using the SSA.

Single Event Solution

Figure 3.3.5 shows the catalogued PPD corresponding to the detection highlighted in Figure 3.2.3 represented as 2D marginal probability distributions in map-view and depth profile computed using 85 DTTs from 14 stations. Side panels show 1D marginal

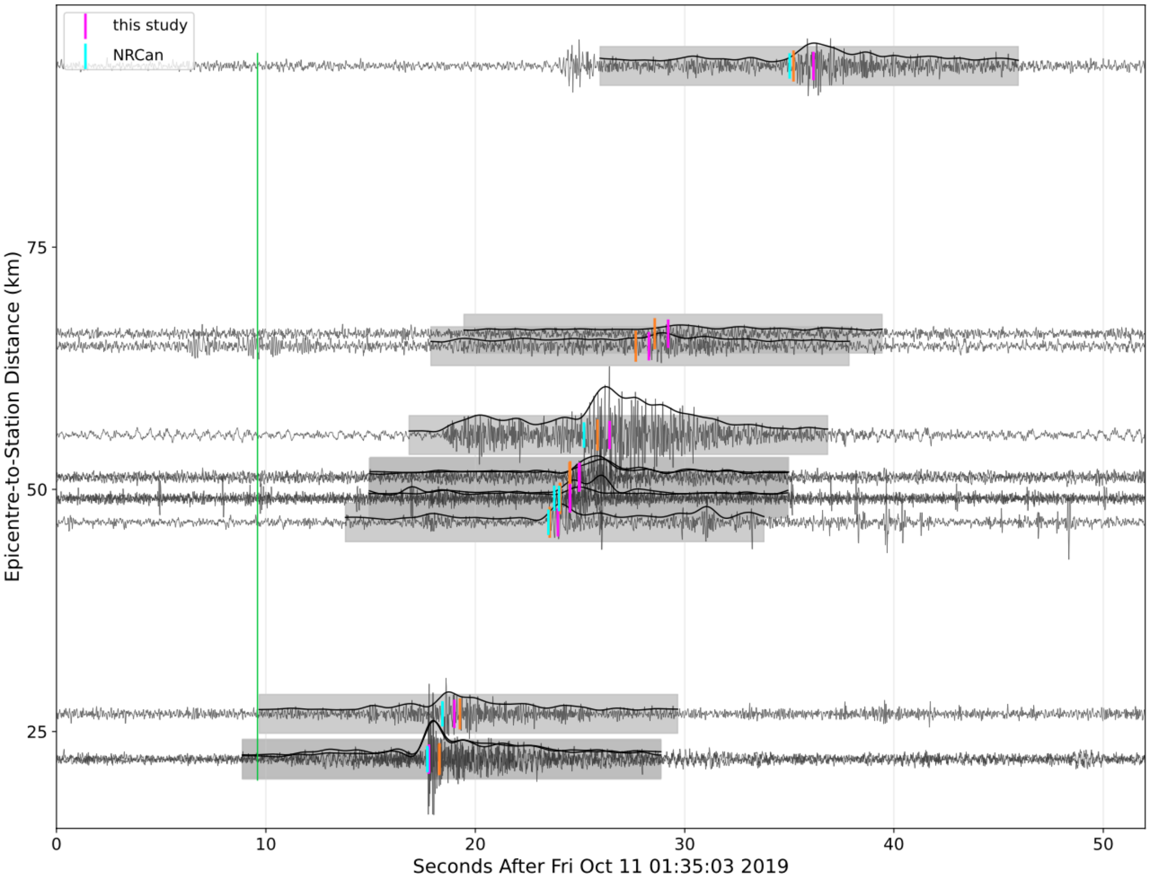

Figure 3.3.4: EW-component waveforms from the highlighted $\mathrm{M_L}$ 0.05 forearc earthquake in Figure 3.3.3, arranged vertically by epicentre-to-receiver distance according to the relocation in this study. Grey shaded rectangles indicate the 20 s CC windows of envelope functions (thick black lines) used to compute DTTs. Magenta markers indicates the theoretical arrival times of the largest S-wave amplitudes from the relocated source calculated with the 3D model used in this study. Cyan markers indicate actual S-phase picks by NRCan analysts for the stations represented. Orange markers indicate the same as magenta markers but for the same depth as the NRCan location. The vertical green line indicates the origin time determined by the DTBI method. 95% CIs are 1 km in EW and NS and 2 km in depth. Epicentral and depth residuals between official and relocated solutions of this event are 2.9 km and 10.0 km, respectively.

distributions with uncertainty in each dimension estimated from their respective 95% CIs, which are 4 km in NS and EW and 8 km in depth. At a depth of 34 km, the maximum *a posteriori* node in the PPD is coincident with the plate interface.

Seismograms corresponding to the tremor event in Figure 3.3.5 are shown in Figure 3.3.6 with their associated envelopes and CC windows. In the 2.75 minutes of waveform data, tremor activity may be identified visually both inside and outside the CC windows with similar moveouts, indicating that it likely originates from similar

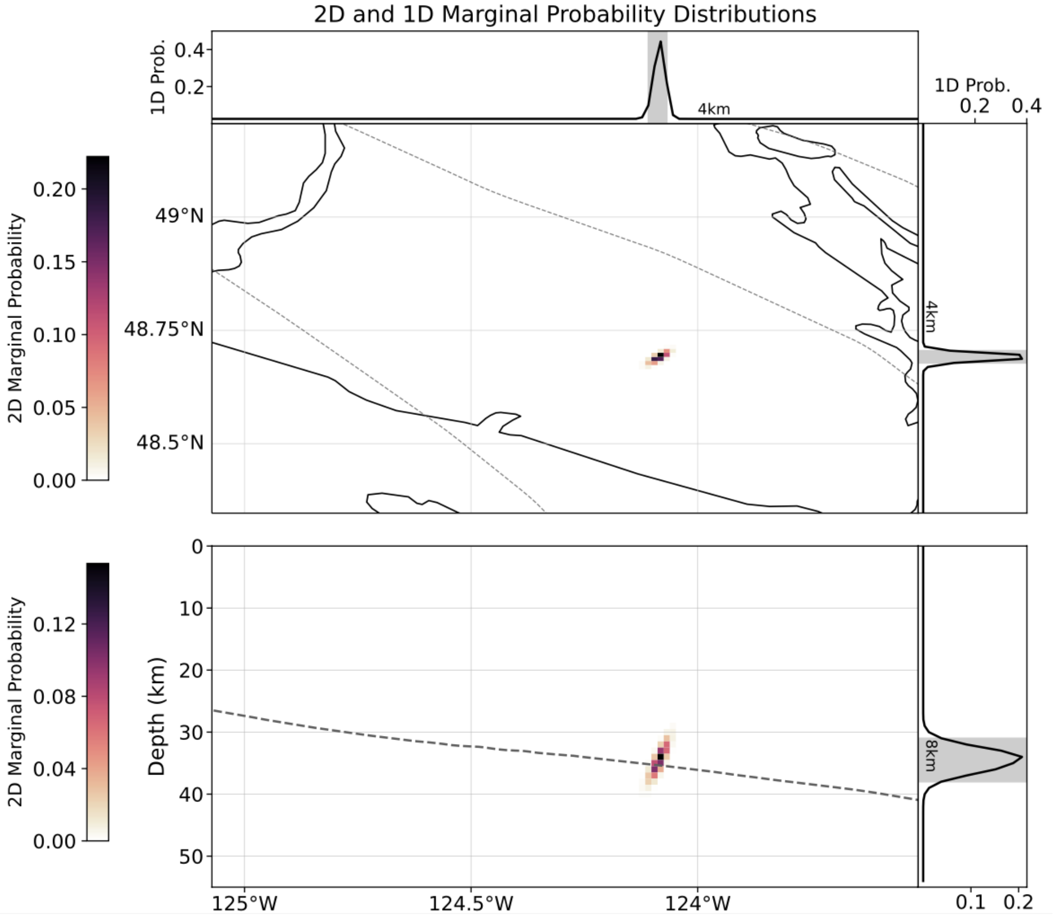

Figure 3.3.5: 1D and 2D marginal probability distributions in map-view (top) and depth profile (bottom) of the tremor event identified in Figure 3.2.3. Each 1 km grid cell in the 2D marginals represents a model node and is coloured by the marginal probability that the seismic source exists at that location. Side panels show the 1D marginal distributions (solid lines) and the 95% CIs (shaded intervals) in each dimension. Grey dashed lines on the map indicate the 30, 40, and 50 km depth contours of the plate interface from McCrory et al. (2012). In profile, the plate interface is interpolated longitudinally at the latitude of the maximum *a posteriori* node, 48.69°N. Depth profile contains no vertical exaggeration.

locations. The clustering behaviour of tremor means that windows containing signal from multiple events may be used to locate clusters rather than individual events, as is the intention behind some tremor location methods that use longer windows (Wech, 2010; McCausland et al., 2010; Armbruster et al., 2014). Within the CC windows there are at least two tremor events that may be identified independently. In Section 3.3.1 we note that the inclusion of P-waves in the CC windows (Figure 3.3.4) has a negligible effect on the DTT values because their amplitudes are consistently smaller than those of S-waves. Due to the fact that tremor signals are emergent and often have low-amplitudes, there is no guarantee that amplitudes from two different events within the same CC windows will be sufficiently and consistently different across the seismic network. As described in Section 3.2.3, the DTBI method has processes to mitigate the effects of this issue to the degree possible by forcing spatial coherence in order to identify such heterogenous datasets, remove outlying data, and terminate localization when necessary. In addition, any catalogue may be screened retroactively to select events that meet stricter criteria (e.g., number of DTTs) than for what the DTBI method already accounts.

Application to the 2004 ETS Event

The 2004 ETS event beneath S. Vancouver Island began generating significant tremor activity in the southeast of the study area on July 8 and migrated northwest along strike over the following 17 days, with most activity terminating after July 25. We present here our DTBI localization results of this episode and compare with the SSA tremor catalogue from Kao et al. (2009).

Figure 3.3.7 shows all events between July 8-25, 2004, from both tremor catalogues coloured by time. Each event in the DTBI catalogue is here considered a point source at the maximum *a posteriori* node in its PPD. Both catalogues show that tremor activity began updip in the JdF Strait and covered the entire ETS zone along-dip over the first few days before beginning a northwest migration along strike around July 15. The DTBI catalogue includes 1,565 events with datasets including up to 188 DTTs (median of 46) from up to 17 contributing stations (median of 12). The median of 95% CI widths in NS and EW dimensions is 7 km and 4 km, respectively, and depth CIs range from 2 to 20 km (median of 9.5 km). A distinct advantage of the DTBI method is that CI-based uncertainties are computed for events individually, which allows for direct estimates of sub-regional resolution. For example, events in the depth profile of Figure 3.3.7c located within ±10 km of the transect have a median depth CI width of 8 km—1.5 km less than the regional median. The SSA catalogue does not provide formal uncertainties, but Kao et al. (2009) estimate that the 0.85 contour in the brightness maps of their best constrained tremor sources may have minimum horizontal and depth intervals of ±2 km and ±4 km, respectively, around the maximum brightness node. Of the 1,584 events in the SSA catalogue, the number of stations used ranges from 8, the minimum we allow in this analysis, to 25 (median of 16), and since each station contributes one datapoint for localization, this is also the size range of the datasets used. Both catalogues include a similar number of events, indicating that the DTBI method yields a reasonable detection rate despite the high thresholds and restrictive measures. The DTBI catalogue has notably fewer detections in the northwest portion of the study area, likely due to the reduced station coverage in mid-Vancouver Island,

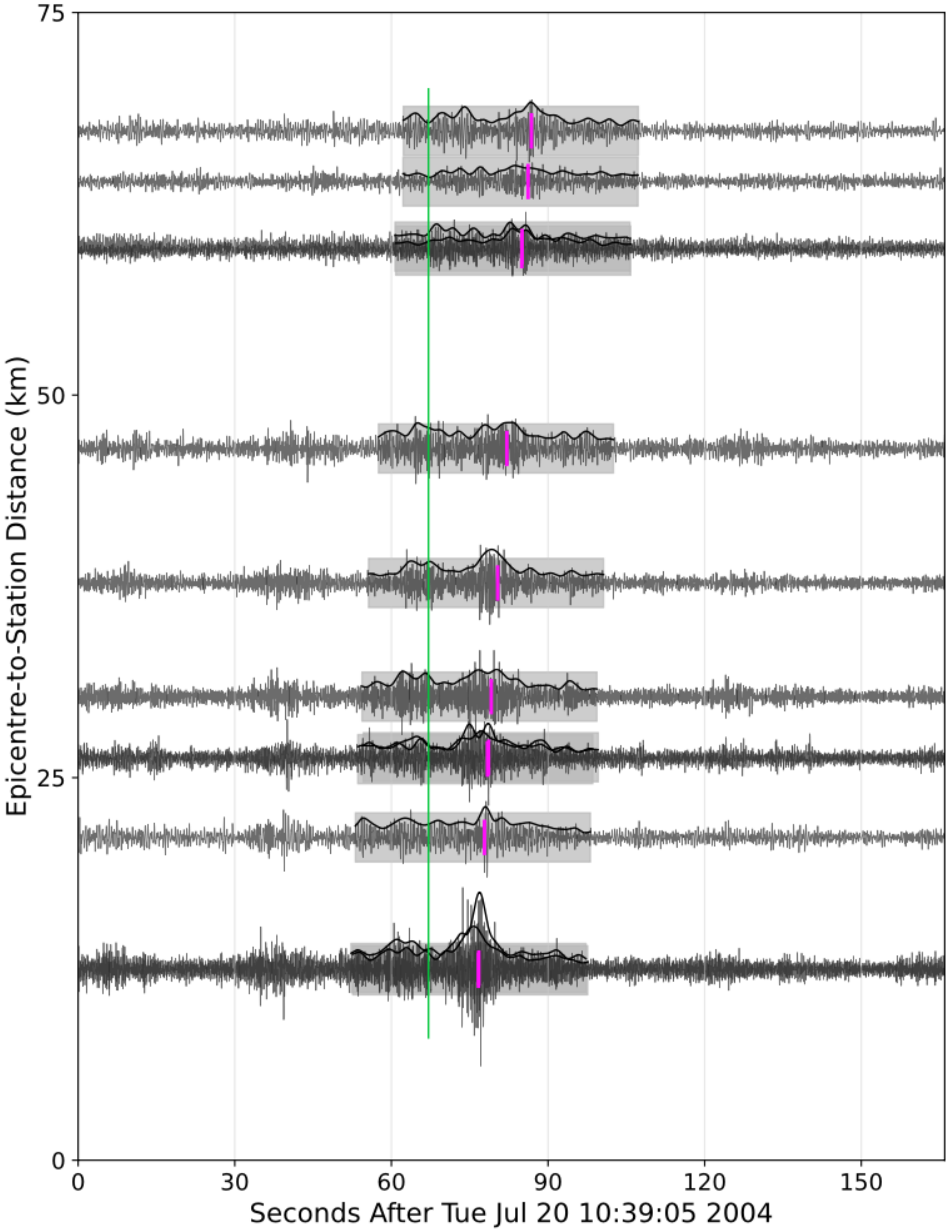

Figure 3.3.6: Same as Figure 3.3.4 but for the tremor localization shown in Figure 3.3.5. Grey shaded rectangles indicate 45 s CC windows of envelopes (thick black lines) used to compute DTTs. The magenta markers indicate the theoretical arrival time of the largest S-wave amplitudes from the catalogued source, and the green line denotes the origin time of the event, 2004-07-20 10:40:12 UTC.

confirming the intuition that requiring larger datasets increases the sensitivity to network density and reduces the detection rate in areas of sparse coverage. However, in the south and southeast through the JdF Strait, the DTBI method makes more detections and exhibits greater epicentral clustering. The DTBI catalogue overall displays a greater degree of epicentral clustering then the SSA catalogue, consistent with previous studies of ETS tremor and low-frequency earthquakes (Ghosh et al., 2012; Armbruster et al., 2014; Savard and Bostock, 2015; Peng and Rubin, 2016), which we interpret to be evidence of better spatial accuracy.

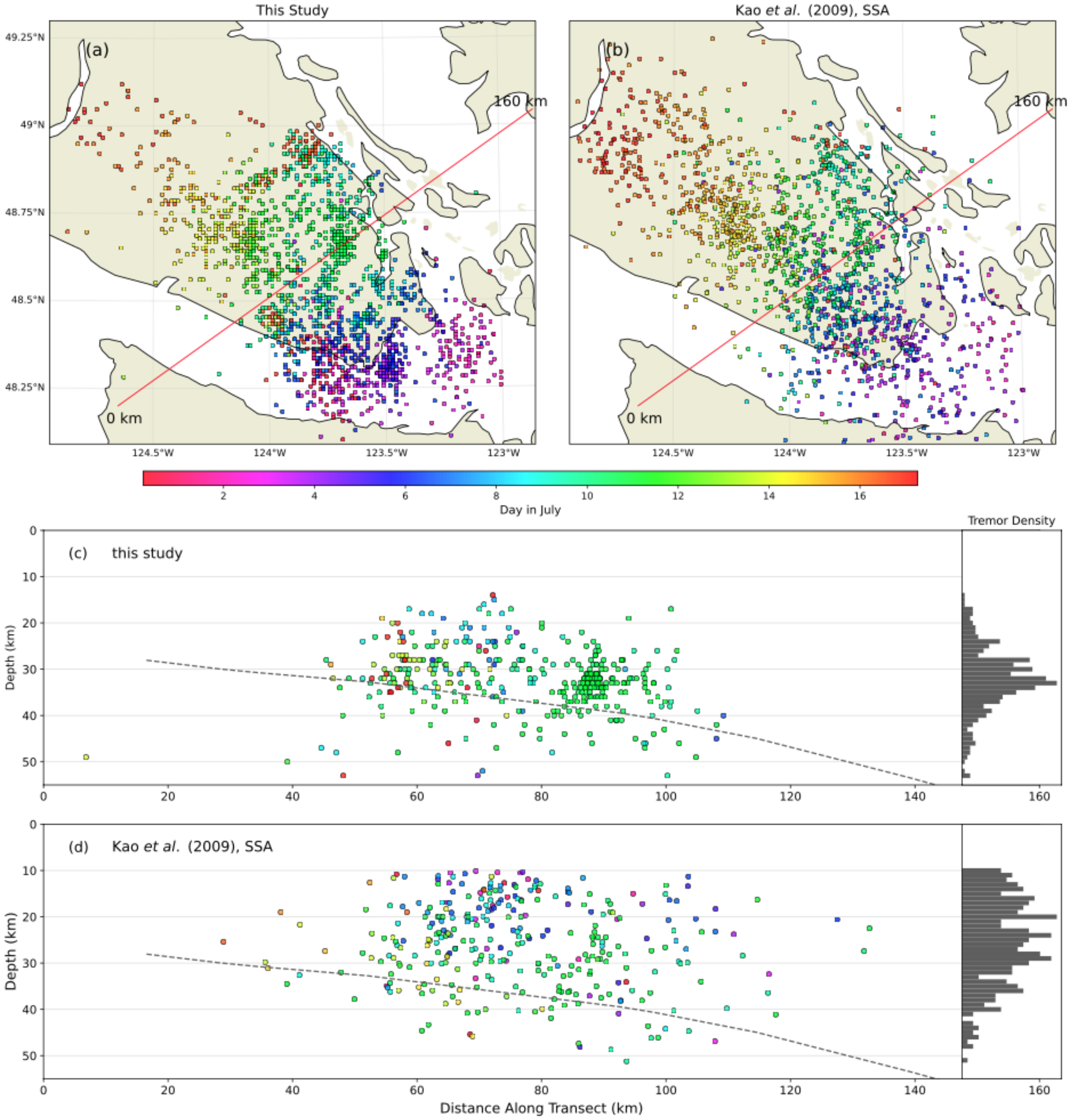

Figure 3.3.7: Spatial and temporal distribution of tremor events located by the DTBI method, (a) and (c), and SSA from Kao et al. (2009), (b) and (d), during the 2004 ETS event. Tremor events are coloured by origin time and projected onto a margin-normal transect [red line in (a) and (b)] from within ±10 km and shown in profiles (c) and (d). Histograms to the right of (c) and (d) show relative tremor density according to depth. The dashed grey line indicates the plate interface from McCrory et al. (2012). (c) and (d) contain no vertical exaggeration.

The depths of tremor events along the indicated transect and shown in the depth profiles of Figure 3.3.7c and d also demonstrate that the DTBI method resolves spatial heterogeneity in depth better than the SSA. As indicated by the density histograms on the right of each profile, the SSA catalogue is more uniformly distributed, with a mean depth of 25.6 km, and has a higher proportion of events located farther from the plate interface, mostly shallower, with a mean depth difference of 11.1 km. Events in the DTBI catalogue cluster between 25 and 35 km depth, with a mean of 33.1 km, and tend to better coincide with the plate interface, with a mean difference of 3.4 km. The primary cause of different average depths between the SSA and DTBI catalogues is likely the different velocity models used in localization, and this trend may not persist throughout the region. The depth and structure of the subduction interface, and consequently the depths and mechanisms of tremor activity in N. Cascadia, remain an active area of study, and we do not presuppose here that tremor originates exclusively from the subduction fault nor that the subduction fault is appropriately represented by the McCrory et al. (2012) plate interface model. Rather we show this model as a commonly-used reference and leave the other topics for future research.

3.4 Conclusions

We have developed a new method of detecting and locating ETS tremor that aims to address some of the fundamental challenges in this area. The DTBI method uses CC-derived DTTs in a Bayesian inversion to locate sources and provide 3D probabilistic uncertainties. We use a recently-developed 3D Vs model and include processes to assess dataset heterogeneity, remove outliers, and estimate data error statistics. Application of this method to local earthquakes <M 2.6 in the S. Vancouver Island region demonstrates that large datasets of low-precision information generally yield relocations in good agreement with the NRCan earthquake catalogue except in the southeastern portion of the study area—the very downdip edge of the ETS zone—where relocations are shallower than expected. We speculate the main cause is that the orientation of systematic errors resulting from using the GSC 1D model is in the deep direction for traditional earthquake localization and the shallow direction for the DTBI method applied to the 1D model. In general, depth is often the most difficult parameter to constrain. Approximately 82% of our relocations using a 3D model have a depth residual <8 km; compared with approximately 46% of relocations using a 1D velocity model. From this, we conclude that a simplified Vs model derived from a 1D Vp model can cause systematic depth errors on earthquake relocations in some areas when only S-wave traveltimes are used, as is common in tremor localization.

We use the DTBI method to locate tremor during the 2004 ETS event and demonstrate its ability to construct sizeable datasets and well-constrained localizations using the regional seismic network. With stringent selection criteria, our tremor catalogue includes approximately the same number of events as the SSA tremor catalogue from Kao et al. (2009) but with more robust and smaller uncertainty estimates. The spatial and temporal progression of tremor in each catalogue agree overall; however, our catalogue shows a greater degree of epicentral clustering throughout the region and a narrower depth range of tremor along a margin-normal transect. In addition to fewer scattered events, the median of depth uncertainties (95% CI widths) is 9.5 km; alternatively, computing standard deviations from the PPDs, the depth uncertainty represents a median standard deviation of 2.3 km, which marks a substantial improvement over other methods that typically have very low or no depth resolution within regional applications. The DTBI method should be well-suited to investigate the spatial relationship between tremor, low-frequency earthquakes, and the structure of the Cascadia SZ, which will be the focus of future work.

Chapter 4

Examining tectonic tremor source depths in relation to subduction zone structure in northern Cascadia

Abstract

Tectonic tremor occurs in frequent episodes throughout N. Cascadia, typically during slow slip events deep in the subduction zone. Tremor localization methods often do not constrain source depths adequately due to the challenges associated with using low-amplitude, emergent waveforms. However, localizing large numbers of tremors yields distributions whose averages are minimally influenced by individual-event uncertainties and can thus reveal spatial trends of tremor. In this study, we examine tremor source depth distributions exhibited in two long-term catalogues in relation to low-frequency earthquakes (LFEs) and key features in the subduction zone imaged using receiver-function analysis. We present a tremor catalogue computed using the differential traveltime Bayesian inversion method where tremor sources are represented as 3D probability distributions. We represent this catalogue as an average over all tremor sources, which provides detailed depth distributions of tremor. Our results show that the highest concentrations of tremor are vertically offset from LFEs by 5–10 km everywhere in N. Cascadia. We also find that neither tremor nor LFEs localize consistently to the top of the oceanic crust, which is often assumed to represent the subduction fault. Rather, tremor localizes throughout a volume corresponding to the deep accretionary complex at depths deeper than 15 km. Where the accretionary complex is vertically-truncated by forearc terranes, such as the Olympic Accretionary Complex in Washington, the tremor depth distribution is similarly vertically restricted. Depth trends of tremor and LFEs through the apex of the bend in the margin may indicate deformation within and above the downgoing plate that is not represented in current models of the subduction zone. We suggest that multiple mechanisms, likely involving shear slip and extensional/fluid-driven fracturing, occur during slow slip events and ul-

timately produce the distributions of tremor presented here. These processes seem to be partly dependent on their distance from the downgoing plate and occur within the compositionally- and structurally-heterogeneous mélange comprising the accretionary complex.

4.1 Introduction

In subduction zones (SZs), geodetically-observed transient surface displacements of several millimetres can be modelled in terms of a few centimetres of slip on a surface at depth that represents the megathrust (Dragert et al., 2001). Contemporaneous signals of low-frequency tectonic tremor occur closely enough in time and space to such slow slip that the combined phenomena is called episodic tremor and slip (ETS; Rogers and Dragert, 2003). In Cascadia, ETS events typically contain several thousand tremor events (Bombardier et al., 2024) and occur downdip of the seismogenic zone (onshore) in an area referred to as the ETS zone. Although the nature of the relationship between tremor and slip is still enigmatic, episodes of tremor events are considered a reliable indicator of ETS in N. Cascadia.

Sources of tectonic tremor can be localized using various methods appropriate for specific features that can be extracted from seismic data. Such features include, for example, general amplitude variations over tens of seconds (i.e., down-sampled or low-pass filtered envelopes, e.g., Obara, 2002; Kao and Shan, 2004; Wech and Creager, 2008; Ide, 2010) and backazimuth direction (e.g., La Rocca et al., 2005). Constraining tremor sources, particularly their depths, using such low-order features from seismic data is challenging.

Embedded within tremor waveforms are short-duration, low-frequency signals from impulsive events called low-frequency earthquakes (LFEs). Detection of such signals is often performed by using a template waveform to detect similar waveforms (matched-filtering; e.g., Shelly et al., 2006; Bostock et al., 2012). Once identified, LFE sources can be localized using traditional earthquake location methods and generally constrained better than tremor sources.

Broadly speaking, the processes generating tremor and LFEs are unknown. It is sometimes thought that LFEs are the constituent unit of the geophysical process that produces emergent tremor signals (Shelly et al., 2007). However, there are a number of findings that bring into question this hypothesis. First, tremor and LFEs sometimes occur in different geographic areas (Ide, 2021). Second, LFE detection in Guerrero, Mexico, reveals that only a third of tremor waveforms contain LFE signals (Frank et al., 2014). Finally, matched-filtering techniques commonly used to detect LFEs have been shown to detect impulsive signals even when impulsive sources are absent (Ide, 2019, 2021).

In this study, we investigate the spatial relationship between tremor and LFEs in N. Cascadia by considering their distribution in depth. Prior to this work, large uncertainties on tremor localizations resulting from the use of low-order waveform properties often precluded useful depth resolution. In fact, tremor and LFE depths are often fixed to a model representing the megathrust either during localization or in their interpretation (Ghosh et al., 2010; Wech and Creager, 2011; Audet and Bürgmann, 2014; Peng and Rubin, 2016). We employ two tremor catalogues and three LFE catalogues for which source depths are independently constrained during localization. The LFE catalogues, computed by Savard et al. (2018), Chestler and Creager (2017), and Armbruster et al. (2014), include family template hypocentres, family centroids, and event hypocentres, respectively. The tremor catalogues include the 15-year source-scanning algorithm (SSA) catalogue (Kao et al., 2009) and a new catalogue computed here using the differential traveltime Bayesian inversion method (DTBI; Bombardier et al., 2023, outlined in the following section).

The two tremor catalogues we employ have an advantage that supports the distribution of tremor depths presented here. Specifically, they both contain large numbers of tremor events (56,000 in total) localized using traveltimes computed with 3D velocity models. The use of a 3D velocity model is an important strategy in seismic localization to limit systematic error (bias), particularly in the depth dimension. Considering a numerous set of events facilitates analysis of trends (e.g., moving median trends), which should yield accurate overall analyses provided systematic errors are insignificant, even if uncertainties on individual localizations are relatively large. In addition, DTBI localizes tremor sources as posterior probability distributions (PPDs), which inherently reflects uncertainties; this method currently provides the best constraints on tremor source depths while maintaining regional coverage (Bombardier et al., 2023).

We investigate the depth distribution of tremor and LFE sources in relation to the latest regional tomographic shear-wave (S-wave) velocity (Vs) models (Savard et al., 2018; Merrill et al., 2020) and a three-boundary model of the SZ estimated by receiver-function inversion (Bloch et al., 2023). Figure 4.1.1 shows the geographic distribution of tremor and LFEs, forearc Vs, and contours representing the depth of the top of the subducting oceanic crust.

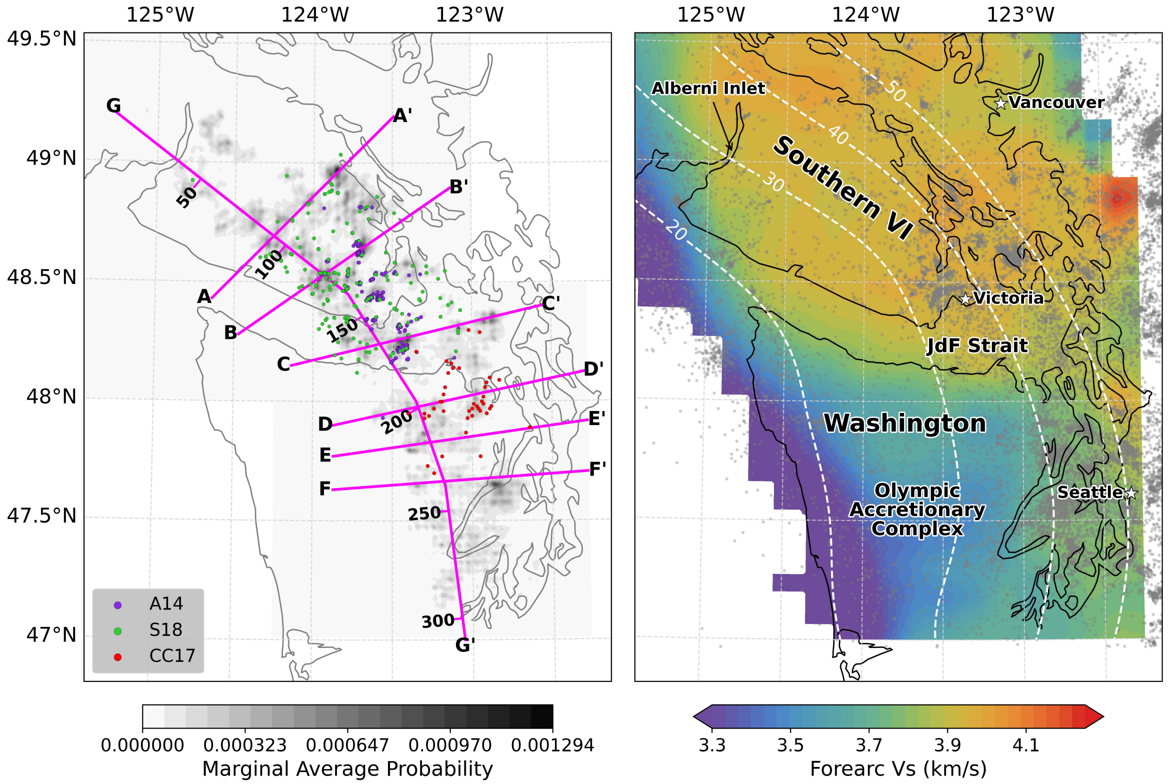

Figure 4.1.1: (left) Map of marginal tremor probability (DTBI average PPD integrated over depth indicated by grey shading) overlain by transects (pink lines) used in this study. LFEs (coloured circles) are coloured by catalogue according to the legend: green, Savard et al. (2018); purple, Armbruster et al. (2014); and red, Chestler and Creager (2017). (right) Map of depth-averaged forearc Vs overlain by regular earthquakes in the NRCan and PNSN catalogues (grey dots) and white dashed lines representing isodepth contours of the top of oceanic crust (Bloch et al., 2023). White stars denote major city centres. JdF: Juan de Fuca. VI: Vancouver Island. A map of tremor in the SSA catalogue is shown in Figure C.0.3.

4.2 Catalogues

4.2.1 Differential traveltime Bayesian inversion tremor catalogue

The DTBI tremor catalogue is computed using the methodology of Bombardier et al. (2023), which is briefly summarized here. Four sequential processes are used to detect candidate tremor events, construct and curate a dataset, and localize sources. The detection procedure is a coarse search through space and time using SSA (Kao and Shan, 2004). Segments of horizontal-component seismograms at multiple seismic stations associated with detections are used in a waveform-envelope cross-correlation to produce S-wave traveltime differences between pairs of stations exhibiting similar envelopes. Datasets of traveltime differences are processed using a modified version of the maximum-intersection (MAXI) technique (Font et al., 2004) to remove outliers and assess data quality. A final grid-based Bayesian inversion is used to compute 3D PPDs as well as optimal point-source solutions, which represent nodes with maximum probability.

Uncertainties of each localization in NS, EW, and depth dimensions are quantified as minimum-width 95% credibility intervals, which are the shortest interval on each 1D marginal probability distribution that contains 95% of the probability. Note that seismic-localization uncertainties are often quantified as standard deviations about the mean. However, for potentially non-Gaussian PPDs estimated in the nonlinear Bayesian inversion, credibility intervals can be a more-meaningful characterization of uncertainty than standard deviations (for a Gaussian distribution, a 95% credibility interval is approximately 4 standard deviations wide, but this does not hold for non-Gaussian distributions).

Credibility-interval uncertainties on all events average 4.0 km in horizontal (NS and EW) and 7.9 km in depth dimensions. Horizontal uncertainties do not exhibit significant systematic variation across the region (Figure C.0.1), but depth uncertainties tend to be larger than average in the JdF Strait ($\sim$ 9–16 km) and near the east coast of S. Vancouver Island (VI; $\sim$ 9–12 km). In comparison, minimum depth uncertainties in the SSA catalogue (Kao et al., 2009, described in Section 4.2.2) are estimated to be 8 km (± 4 km about the point-source location), and larger by a factor of two or more for poorly constrained sources. However, SSA uncertainty estimates are based on the distributed "brightness" of a regular earthquake test case, whereas DTBI uncertainty estimates represent probability and are specific to each tremor source.

From the original development of the DTBI method (Bombardier et al., 2023), two changes have been made to reduce computation time. First, the SSA detection procedure is limited to a 2D search space fixed at 25 km depth. This detection step only provides temporal flags at seismic stations that serve to orient the subsequent steps. Depth estimates of detections with SSA are very poorly constrained and therefore provide little useful information at this stage of the DTBI workflow at the cost of considerable computation time. Second, the grid for the Bayesian inversion is limited to 15 nodes (i.e., 15 km given 1 km grid spacing) in each cardinal direction around preliminary location solution epicentres. Preliminary location solutions estimated from the MAXI technique vary by only a few kilometres from final solutions in NS and EW dimensions, so a limited search space is sufficient to encompass the final solution. Additionally, given small horizontal uncertainties (Figure C.0.1), it is not necessary to compute posterior probabilities over the entire grid of the study area. Rather, we compute posterior probabilities within a limited epicentral area (31 km × 31 km) over the entire depth range (0–54 km depth) encompassing the preliminary location solution; posterior probabilities at all other nodes are normally extremely small and considered to be zero. Where preliminary solutions are < 15 nodes from a study area boundary, a 31 km × 31 km × 54 km volume is still used but the epicentre is off-centre.

The DTBI catalogue is computed considering the Vancouver Island and Washington regions separately with overlapping coverage in the JdF Strait (see Figure 4.1.1 for geographic references). Traveltimes are computed between all nodes and receivers each calendar year in each study area to account for changes in the station network over time (see Figure C.0.2 for station maps). Traveltimes are computed using 3D tomographic Vs models from Savard et al. (2018) and Merrill et al. (2020) for Vancouver Island and Washington, respectively, using the Python-based ray-tracing program PyKonal (White et al., 2020). Time periods during which tremor is localized in each study area are given in Table 4.2.1. Episodes of tremor events have variable characteristics throughout N. Cascadia (Bombardier et al., 2024), so a set of episodes are selected to provide balanced detection throughout the ETS zone while preferring times when station coverage is densest.

Point-source solutions (Figure C.0.3) are only used here to identify and remove earthquakes and duplicate tremor events between the Vancouver Island and Washington study areas. Any two tremor events with origin times and epicentres separated by less than 10 s and 10 km, respectively, are considered duplicates; in such cases the event localized using the Washington study area seismic network is preferred due to generally-better station coverage and the more-recent tomographic model. Any events with origin times and epicentres within 20 s and 20 km of known earthquakes in the NRCan and PNSN catalogues are considered earthquake relocations and are removed. This step removes 90 suspected earthquakes from the DTBI catalogue. We note that the median absolute depth residual of these 90 earthquake relocations is 5.0 km (89% of depth residuals < 10 km), despite that fact that relocations are computed using a parameterization scheme designed for tremor. Manual inspection finds that earthquakes not catalogued by official agencies still remain in the DTBI catalogue; we estimate that the number of such events is small (a few dozen at most), so effects on our analysis are insignificant. Finally, events in the DTBI catalogue are also removed if their point-source solutions have depths equal to the 54-km lower depth boundary or less than 10 km. The above steps remove a total of 12% of events initially localized, and the remaining 13,049 events are used in subsequent analyses as one coherent catalogue.

In this study, we represent the entire DTBI catalogue as the average of all event PPDs (e.g., Figure 4.1.1), henceforth referred to as the average PPD. Since the average

Table 4.2.1: Time periods during which tremor is localized in the DTBI catalogue. Vancouver Island and Washington are considered separate study areas for the purposes of localization, and results are combined in the final catalogue as described in Section 4.2.1.

Region	Dates (YYYY/MM/DD)
Washington	2010/08/01 – 2010/09/04
	2017/02/13 – 2017/03/04
	2021/09/26 – 2021/10/28
	2022/05/20 – 2022/06/05
	2022/08/03 – 2022/08/11
	2022/10/22 – 2022/10/30
	2022/12/02 – 2022/12/06
	2023/04/05 – 2023/04/23
	2023/06/28 – 2023/06/28
	2023/08/16 – 2023/08/17
	2023/09/21 – 2023/09/22
Vancouver Island	2005/09/05 – 2005/09/28
	2010/08/15 – 2010/09/08
	2004/09/30 – 2004/10/04
	2021/09/30 – 2021/10/31
	2022/08/26 – 2022/09/01
	2022/12/14 – 2022/12/16
	2023/02/19 – 2023/02/24
	2023/07/06 – 2023/07/08
	2023/09/17 – 2023/09/17

PPD incorporates the distributed probability of all tremor events, it implicitly includes the uncertainties of individual events. The nature of averages is such that events with highly-concentrated PPDs contribute more substantially to the average at a smaller number of grid nodes than events with widely-distributed PPDs. As such, the average PPD should not be thought of as a histogram (count of events) or a proxy for event density, but rather the probability that at least one tremor event occurred at each node in the study study area within the study periods given in Table 4.2.1.

4.2.2 Source-scanning algorithm tremor catalogue

The SSA tremor catalogue from Kao et al. (2009) has been updated by its authors (but not previously published) to span the years 1997 to 2012 and includes 43,416 events (Figure C.0.3). This catalogue is computed using the methodology described in Kao and Shan (2004) and Kao et al. (2009) with traveltimes computed using a 3D Vp model (scaled by 1.73 to represent Vs; Ramachandran et al., 2006). The SSA catalogue is presently the only temporally-continuous tremor catalogue in N. Cascadia to resolve source depths on a regional scale, but its spatial coverage extends only as far south as the JdF Strait. Tremor depths are fairly scattered in the SSA catalogue (e.g., Bombardier et al., 2023), so we consider only depth trends. The median depth of a large set of tremor events such as this can provide accurate information, even if uncertainties on individual events are large, unless localizations are influenced by systematic error. A common source of systematic error in localization is inaccurate velocity models, and since the DTBI and SSA catalogues are both computed using traveltimes from 3D velocity models, we consider any such errors to be reasonably limited.

4.2.3 LFE Catalogues

Three LFE catalogues totalling exactly 1,000 localized events are employed in this study: LFE family template hypocentres (202 localizations) originally created by Bostock et al. (2015) and relocated in the tomographic inversion by Savard et al. (2018); LFE family centroids (45 localizations) created by Chestler and Creager (2017); and 4-S-plus-1-P LFE hypocentres (753 localizations) created by Armbruster et al. (2014). Interested readers can refer to the original publications for more information about the methods used. We employ these catalogues as they are provided by the authors without additional processing.

Tremor and LFE localizations are considered in relation to Vs and key SZ features. The Vs model is derived from 3D Vs tomographic models for Vancouver Island (Savard et al., 2018) and Washington (Merrill et al., 2020). The same methodology is used to compute both models making them directly comparable (Merrill et al., 2020). The models are merged by interpolating each onto a common 1 km^3 grid and averaging the two at nodes where both contain values. The SZ model is a three-boundary model estimated from receiver-function inversion by Bloch et al. (2023). The model resolves boundaries interpreted to be the oceanic Moho, the top of the oceanic crust, and the top of the ultra-low-velocity zone (ULVZ). The ULVZ, identified by high Vp/Vs ratios in tomographic models, has been interpreted as a volume of fluid-rich material with near-lithostatic pore-fluid pressures (Audet et al., 2009) either within the subducting crust or overriding forearc (discussed further in Section 4.4.1).

4.3 Observations

Profiles along dip and strike of the SZ are shown in Figures 4.3.1 and 4.3.2 corresponding to transect lines in Figure 4.1.1. The average PPD from the DTBI catalogue, the Vs model, and the SZ model are represented as vertical slices interpolated along transect planes. LFEs and earthquakes are projected onto transect planes within a perpendicular distance of ±5 km. Tremor events in the SSA catalogue within ±5 km are projected onto transect planes and represented as depth trends (moving median lines).

Five key observations from Figures 4.3.1 and 4.3.2 can be summarized as follows:

1. High tremor probabilities in the DTBI average PPD are generally in agreement with tremor source-depth trends along dip and strike in the SSA catalogue (dark blue lines).

2. Tremor source depths do not coincide strictly with any one feature in the SZ model and can span several kilometres in depth. In S. Vancouver Island (transects A and B), tremor is localized within the oceanic crust, ULVZ, and lower forearc crust. In WA, tremor is localized predominantly within the ULVZ and lower forearc crust (transects D and E), but seldom within the oceanic crust (transect F).

3. Tremor and LFEs are vertically offset by $\sim$ 5–10 km at nearly all locations, with LFEs typically occurring at the deepest edge of the average tremor PPD.

4. LFEs do not coincide strictly with any one feature in the SZ model. LFEs localize near the oceanic Moho beneath S. Vancouver Island and near the top of the oceanic crust in the JdF Strait and WA.

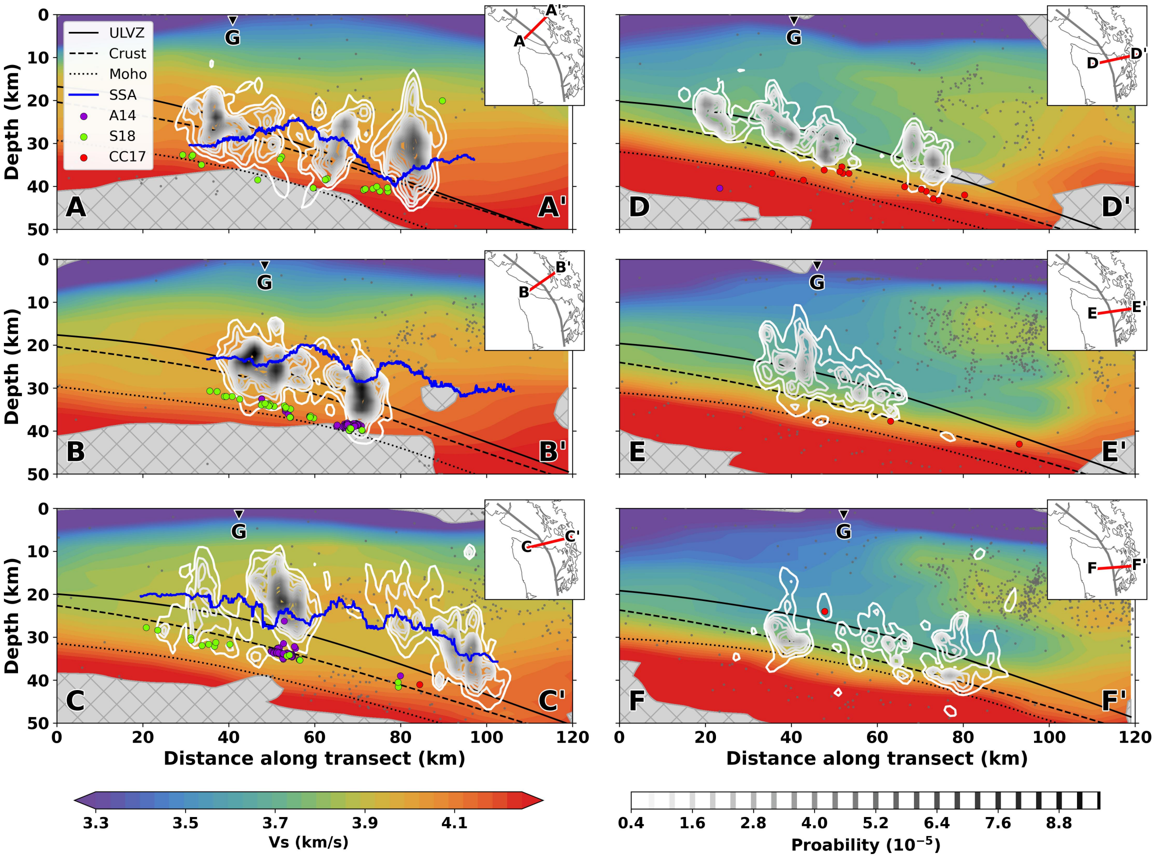

Figure 4.3.1: Along-dip transects showing Vs, key SZ features, tremor, and LFEs. Greyscale contour lines represent tremor probabilities in the DTBI average PPD. LFEs are represented as circles coloured by catalogue: purple, Armbruster et al. (2014); green, Savard et al. (2018); and red, Chestler and Creager (2017). Blue lines are moving-median trends of 2561, 1966, and 780 events from the SSA catalogue on transects A, B, C, respectively. Dotted, dashed, and solid black lines represent the tops of the oceanic Moho, crust, and ULVZ, respectively, and grey dots are earthquakes within ±5 km of transects. Intersection points of the along-strike transect G are indicated by inverted black triangles. Background shading represents Vs and is masked (grey hatching) where resolution is low according to checkerboard tests (Savard et al., 2018; Merrill et al., 2020). Inset maps indicate the transect location of each profile (red) and intersecting along-strike transect G (grey). No vertical exaggeration.

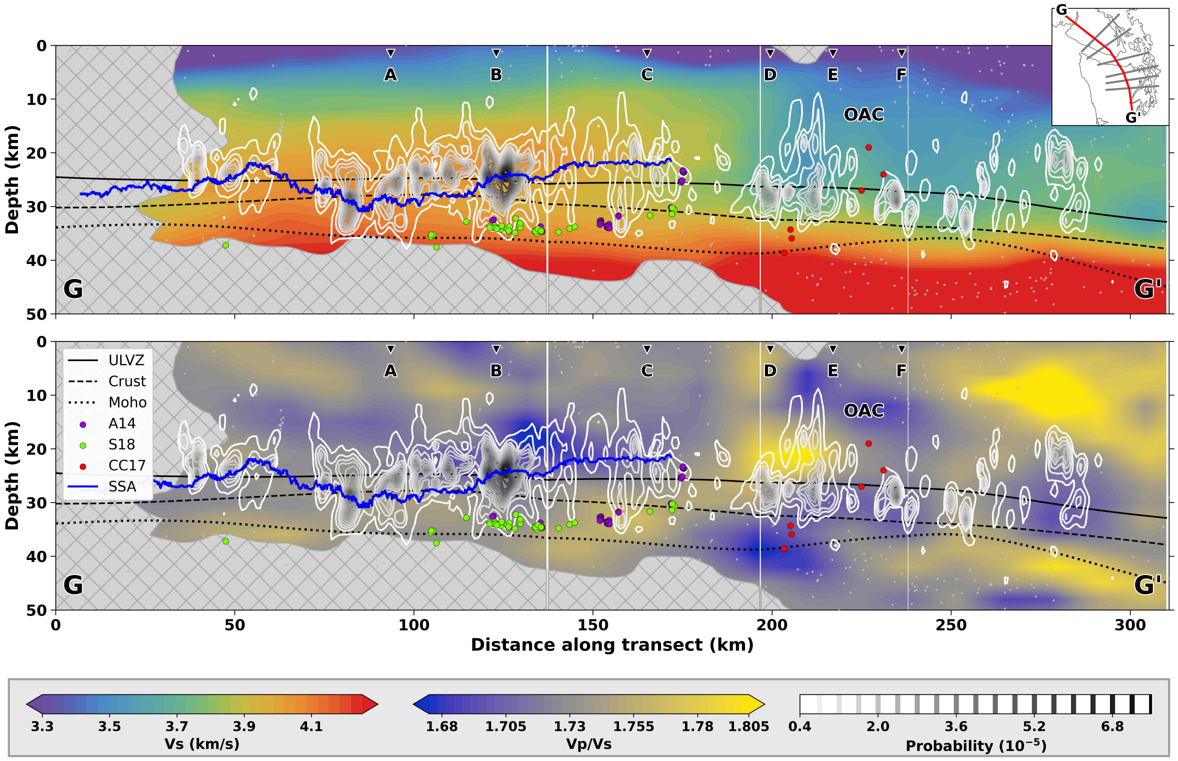

Figure 4.3.2: Along-strike transect G-G' (north to south) showing seismic velocities, key SZ features, tremor, and LFEs. Greyscale contour lines represent tremor probabilities in the DTBI average PPD. LFEs are represented as circles coloured by catalogue: purple, Armbruster et al. (2014); green, Savard et al. (2018); and red, Chestler and Creager (2017). The blue line is a moving-median trend of 4722 events from the SSA catalogue projected onto transects from within ±5 km. Dotted, dashed, and solid black lines represent the tops of the oceanic Moho, crust, and ULVZ, respectively, and grey dots are earthquakes within ±5 km of transects. Intersection points of along-dip transects A to F are indicated by inverted black triangles. Background shading represents Vs (top) and Vp/Vs (bottom) and is masked (grey hatching) where resolution is low according to checkerboard tests (Savard et al., 2018; Merrill et al., 2020). Inset maps indicate the transect location of the profile (red) and intersecting along-dip transects A to F (grey). OAC: Olympic Accretionary Complex. Vertical exaggeration is 1.5.

5. The average PPD is deeper and more narrowly-confined in depth beneath the low Vs signature of the Olympic Accretionary Complex along transects E and F.

4.3.1 Accuracy of tremor depths

There are two lines of reasoning that support the distribution of tremor depths presented here. First, DTBI and SSA methods use 3D velocity models to minimize errors. Bombardier et al. (2023) demonstrate that DTBI-relocated earthquakes have a median depth residual 3.6 km larger when using traveltimes computed with a 1D velocity model instead of a 3D model.

Second, high tremor probabilities in the DTBI average PPD correspond well with moving-median trend lines of the SSA catalogue along dip and strike (observation 1). While DTBI uses a simple version of SSA as its detection procedure, there are significant differences between the two methods that ultimately produce the tremor catalogues employed here. For instance, DTBI uses S-wave traveltime differences from horizontal-component seismograms, whereas SSA uses absolute S-wave traveltimes from horizontal- and vertical-component seismograms. In addition, the DTBI method uses 45 s windows of low-pass filtered (0.3 Hz) waveform envelopes in a cross-correlation procedure, whereas SSA back-projects tremor envelope peaks in a grid search.

If systematic error is to explain the tremor depth distributions presented here, it would need to produce similar effects in the same geographic areas in both tremor catalogues. Given the use of different 3D velocity models, different data types, and different methodological procedures, it seems highly unlikely that systematic error is responsible for our observed depth distributions.

4.4 Interpretations

We focus our interpretation on two fundamental questions: where (and what) is the megathrust in the ETS zone (Section 4.4.1), and how do tremor and LFEs differ (Section 4.4.2)?

4.4.1 Tremor and the megathrust

A variety of geophysical observations—tomography (e.g., Ramachandran et al., 2005, 2006; Savard et al., 2018; Preston et al., 2003), receiver functions (Nicholson et al., 2005; Audet et al., 2010; Bloch et al., 2023), seismicity (McCrory et al., 2012), and seismic reflection (Hyndman et al., 1990; Clowes et al., 1997; Calvert et al., 2011)—have been used to constrain the depth of the megathrust in the ETS zone in N. Cascadia, but estimates between these references vary up to 10 km. The most significant source of this variation/uncertainty is not poor-quality or insufficient data, but rather the interpretation of the data. Results from seismic-reflection imaging may be interpreted such that the “F” reflector denotes either the oceanic Moho (Calvert et al., 2020) or the top of the subducting slab (Hyndman et al., 1990). Receiver-function analysis may be used to interpret the location of the ULVZ to be either within the subducting slab (Nicholson et al., 2005; Audet et al., 2010) or within a layer of sediment accreted to the base of the forearc crust (Bloch et al., 2023). Further uncertainty arises in the attempt to interpret between studies. For example, seismic-reflection images reveal a several-kilometre-thick band of high reflectivity (the “E”–layer) that corresponds roughly with the ULVZ in tomographic models, but whether these should be interpreted as different features (Calvert et al., 2020) or two representations of the same feature (Calvert et al., 2011) is still debated.

The SZ model employed here interprets oceanic Moho, oceanic crust, and ULVZ signatures from receiver-function analysis. However, even perfect delineation of these features does not, by definition, provide a comprehensive description of all structures within the SZ, nor does it describe where seismogenic and tremor-generating processes occur. Normally, the megathrust fault is interpreted to be located at the top of the oceanic crust; however, given the aforementioned uncertainties, we do not assume here that the megathrust fault in the ETS zone corresponds to any particular feature in the SZ model, nor that subduction-driven processes and deformation are restricted to the megathrust.

The structure and location of the SZ depends on current and historical accretionary dynamics (Angiboust et al., 2021). Within a SZ there may be areas of accretion, whereby subducted material is deposited onto the underside of the upper plate (underplating), and erosion, whereby material from the downgoing plate or underplated mélange is removed and subducted. A given area may undergo alternating periods of accretion and erosion on million-year time scales, which can build extensive accretionary complexes in the middle and lower forearc crust ($\sim$ 15–45 km depth). Seismic reflection images (Clowes et al., 1987; Nedimović et al., 2003; Calvert et al., 2006) and gravity anomalies (Bassett and Watts, 2015) do indeed support the existence of a deep accretionary complex or duplex structure coinciding with the ETS zone in Cascadia. Within this framework, the megathrust supports elevated strain rates in the accretionary complex above it (Angiboust et al., 2021). The extent to which subduction-driven processes penetrate surrounding rock volumes likely depends on many factors, the study of which is beyond the scope of this work. We consider that the distribution of tremor could be interpreted to provide constraints on the location of some subduction-driven processes and possibly the minimum extent of the accretionary complex. In this section, we draw upon these ideas to interpret some features presented in Figures 4.3.1 and 4.3.2.

LFEs in S. Vancouver Island (transects A and B) localize near the oceanic Moho, $\sim$ 5 km deeper than the top of the oceanic curst (observation 4). Southward along strike (Figure 4.3.2), LFEs exhibit a shallowing trend through the JdF Strait (150–175 km), although remaining within the oceanic crust. Bloch et al. (2023) suggest these LFEs may represent the lower bound of a segment of oceanic crust actively detaching from the downgoing plate. Tremor depths in JdF Strait are localized up to 15 km above LFEs and the modelled oceanic crust, particularly downdip of transect G (Figure 4.3.1 transect C). At $\sim$ 175 km along strike, LFEs localize at and above the top of the oceanic crust, including a cluster of 14 LFEs from Armbruster et al.'s (2014) catalogue above the ULVZ at $\sim$ 24 km depth. Between 175 km and 190 km along strike there is an apparent gap of tremor coincident with the northern coast of Washington in the updip portion of the ETS zone (also evident in Figure 4.1.1). It is important to note that this tremor gap is apparent in the set of tremor episodes localized in this study (Table 4.2.1) but may not be present if more/different episodes were included.

Analysis of the Cascadia SZ through the CASIES21 survey (Carbotte et al., 2024) showed that the subducting JdF plate is susceptible to deformation and tearing, particularly due to loading from the upper plate. While the CASIE21 survey focused on the seismogenic zone offshore, it is prudent to consider the effects of such properties in the ETS zone. The depth distributions and trends of tremor and LFEs in JdF Strait and north coast of Washington suggest that there may be significant deformation of the downgoing plate in this area. Receiver-function and tomographic analyses can have relatively low resolution at slab depths in the ETS zone, and the addition of smoothing constraints and regularizing assumptions mean that some structures will not be represented in such models. The concave-oceanward geometry of the N. Cascadia orocline, which reaches its apex at the JdF Strait/N. Washington coast, is potentially suggestive of syntaxial folding/buckling (Mahadevan et al., 2010). However, to date no such feature has been observed or inferred, which suggests that, if such a feature does exist, it does not dominate the large-scale geometry of the subducting plate. Some work suggests that the N. Cascadia oroclinal bend is more likely driven by kinematics in the forearc rather than slab buckling (Finley et al., 2019; Aldrich, 2021).

The location of LFEs deep in the oceanic crust in S. Vancouver Island nevertheless suggests significant intraslab deformation. The shallowing trend of LFEs through the

JdF Strait terminating at the tremor gap of the N. Washington coast indicates that this intraslab activity is unique to Vancouver Island and that a transition or boundary exists between Vancouver Island and Washington. The JdF Strait is coincident with a major transition in forearc lithology—from the Wrangellia terrane complex in S. Vancouver Island to the Olympic Accretionary Complex and Siletzia in Washington—in addition to the apex of the oroclinal bend. Such large-scale properties of the forearc crust likely influence deformation within the downgoing plate, as indicated by the CASIES21 experiment (Carbotte et al., 2024). The three-dimensional distribution of tremor and LFEs supports the existence of significant structural features in the SZ in the vicinity of JdF Strait (150–175 km along strike) coincident with an along-strike transition of forearc lithology.

Between 190 km and 215 km, just south of the tremor gap (Figure 4.3.2), there is a low Vs, high Vp/Vs anomaly that is most prominent between transects D and E. Further south, the average tremor PPD is deeper and more narrowly-confined in depth beneath the Olympic Accretionary Complex along transects E and F (observation 5). In tomographic analyses, the Olympic Accretionary Complex is characterized by low Vs and low Vp/Vs ratios (Merrill et al., 2020), which indicates that this low Vs-high Vp/Vs feature is compositionally or structurally distinct from the Olympic Accretionary Complex. This high Vp/Vs feature is also coincident with tremor probabilities that extend well above the ULVZ. This abrupt change in the tremor depth range suggests that the Olympic Accretionary Complex, which extends to the depth of the oceanic crust (Merrill et al., 2020), imposes a significant control on the distribution of tremor-generating processes. The presence of this terrane may limit the vertical extent of the deep accretionary complex and thus tremor activity. As a result, water released from the subducting plate may be vertically restricted and sequestered to the north, creating the low Vs-high Vp/Vs anomaly and shallower tremor activity at $\sim$ 200 km along strike.

4.4.2 Tremor and LFEs

Depths where tremor is most probable do not coincide with LFE hypocentres anywhere in N. Cascadia (observation 3). Tremor probability contours sometimes have lobes extending $\sim$ 5–10 km down to LFE depths (e.g., Figure 4.3.1 transects B and C). LFE signals are often identified in tremor waveforms (e.g., Shelly et al., 2007), so it is very likely that tremor catalogues include some LFEs. We also cannot rule out the possibility that some tremor may occur at LFE depths. In either case, the ubiquitous vertical offset between LFEs and peak tremor suggests that processes generating such seismic signals span a range of $\sim$ 5 km beneath the Olympic Accretionary Complex (transect F), $\sim$ 5–10 km beneath S. Vancouver Island (transects A and B), and $\geq$ 10 km beneath JdF Strait (transect C). In addition, our observations indicate tremor and LFE generating processes are depth dependent, such that LFEs are generated deeper than most or all tremor at the same geographic location.

The processes generating tremor and LFEs are largely unknown. Evidence contributing to the understanding of source mechanisms comes from seismology, theoretical modelling, and geologic and petrologic observations. Specifically, seismological studies of moment tensors (Ide et al., 2007; Royer and Bostock, 2014), particle-motion polarization (La Rocca et al., 2005; Kao et al., 2006; Wech and Creager, 2007), frequency content of seismic energy emission (Wang et al., 2023), and LFE magnitude scaling (Bostock et al., 2015) reveal low-dip-angle double-couple thrust mechanisms that are scale-limited and produce low-frequency seismic energy with mostly transverse or horizontal particle motions. Localization analyses of tremor and LFEs reveal migration behaviours over a wide range of length and time scales. For instance, LFEs have been observed migrating rapidly transverse to the slip front (termed "rapid tremor migrations") and radially backwards from the slip front ("rapid tremor reversals"; Peng et al., 2015; Peng and Rubin, 2016) with migration speeds at least two orders of magnitude faster than the slip front itself (Gombert and Hawthorne, 2023). In addition, tremor epicentres are often localized to the leading edge of the slow slip area, rather than the location of peak slip (Bartlow et al., 2011; Hall et al., 2019; Itoh et al., 2022), which indicates a complex relationship between tremor and slip.

Mathematical and numerical modelling of fluid pressure and permeability (Farge et al., 2023; Shapiro et al., 2018), brittle-ductile matrices (Chestler and Creager, 2017; Luo and Liu, 2021), granular log jams (Sammis and Bostock, 2021), and mixed models (Bernaudin and Gueydan, 2018) provide possible explanations for ETS periodicity, the spectrum of ETS magnitudes/sizes, and the constituent cascades of seismic events (i.e., swarms of tremor and/or LFEs). This body of work constitutes a diverse set of models that generally serves to expand the scope of possible mechanisms rather than constrain it. In addition, Shapiro et al. (2018) demonstrated that the seismic radiation pattern and particle-motion polarization of a single-force mechanism, such as a pressure pulse, can be nearly identical to that of a low-dip-angle double-couple shear displacement when observed on a typical SZ seismic array. This suggests that there may be a significant observational limitation on the discernment between certain types of source mechanisms in a SZ setting.

Paleo-geologic studies provide essential observations on the composition and deformation styles within deep accretionary complexes because this area is often near the limit of what is observable using geophysical methods. At the same time, it remains challenging to identify exhumed paleo-subduction complexes that are close analogues of those that are currently active. In addition, it can be exceptionally difficult to integrate static, small-scale geologic observations with large-scale, dynamic geophysical processes. Geologic and petrologic observations (Bürgmann, 2018; Platt et al., 2018; Kirkpatrick et al., 2021; Condit and French, 2022) from exhumed SZs presumed to have hosted slow slip reveal widespread evidence of fluids at high pressures in complex networks of cracks, folds, and shear bands. These deformation zones include evidence of brittle and ductile deformation, foliation (mechanical anisotropy) due to directional strain, and intrinsically-weak mineral assemblages associated with a range of metamorphic environments. Such studies reveal that slow-slip source regions are not associated with a single deformation mechanism or petrologic profile (Kirkpatrick et al., 2021). Rather, these areas are characterized by compositional heterogeneity (variable within and between sites) and structural complexity (Behr and Bürgmann, 2021). Extensional fracturing within folds (i.e., crenulation trains; Platt et al., 2018) and fault-fracture meshes (Sibson, 2017; Ujiie et al., 2018) are coexistent with shear slip due to the complex geometry within these networks.

Within a framework that involves mechanisms of shear slip and extensional fracturing, it is well accepted that the former is a plausible mechanism of tremor and/or LFE generation; however, laboratory experiments demonstrate that fluid-driven fracturing/cracking also generates tremor-like signals (Yuan et al., 2024). Given the diversity of geologic observations and theoretical models, it seems possible, if not likely, that the production of tremor and LFEs involve multiple mechanisms of action. Future work may be able to parse seismic data to reveal the signature of multiple different mechanisms.

4.5 Limitations and Future Work

In this study, we have not rigorously defined a tremor event. If the differences between tremor and LFEs demonstrated in Section 4.3 are shown to be robust, there should be some precise description of the distinction between tremor and LFEs in terms of both the waveform characteristics and geophysical mechanisms. In addition, tremor and LFEs represent only the high-frequency (>1 Hz) component of a more broadband phenomenon that includes very low-frequency earthquakes (Ide et al., 2008; Ide, 2016, 2019; Fan et al., 2022), which were not considered in this study.

The work presented here considers only spatial distributions of seismic localizations. To the degree that a comparison in the space and time domains is possible, work that considers migration characteristics of tremor and LFEs will likely provide additional insights on the nature of their differences. A more direct comparison could use a single workflow to localize tremor and LFEs that are both present in the same waveforms rather than relying solely on the results from independent studies.

Finally, detecting and localizing tremor and LFEs has been carried out in a variety of ways and can be exceptionally challenging, often requiring many steps of processing and numerical problem solving. Much of this methodology is experimental, without the luxury of years of routine use and troubleshooting. Methodological improvements could include more rigorous measures to assess and minimize systematic error and uncertainties.

4.6 Summary and Conclusions

Two common ideas are commonly discussed in scientific literature on deep subduction ETS: (1) LFEs are the constituent unit of tremor, and (2) tremor and LFEs observed during ETS occur on the megathrust fault. In this study, we provide observational evidence that some ETS processes in N. Cascadia occur within a volume corresponding to the deep accretionary complex and that localizations of tremor and LFEs from multiple studies exhibit prevailing systematic differences.

The two tremor catalogues we employ have an advantage that supports the analysis of tremor depths present here. Both localization methods for the SSA ($\sim 43,000$ events) and DTBI ($\sim 13,000$ events) catalogues use traveltimes computed using 3D velocity models, which limit the influence of systematic error on location solutions. As such, analysis of tremor depth averages (or trends) should reflect real source depths. General agreement between the depth trends in the two catalogues further indicates that significant systematic error is unlikely. In addition, the DTBI catalogue is computed using a Bayesian inversion whose probabilistic uncertainty estimates indicate the best depth constraints on tremor sources to date, with average depth uncertainties (95% credibility intervals) of ~ 8 km. The average tremor PPD provides detailed insight into the 3D distribution of tremor throughout the N. Cascadia region. Using a SZ model representing the oceanic Moho, the top of the oceanic crust, and the top of the ULVZ (Bloch et al., 2023), we explore implications of tremor and LFE depth distributions on the structure of the SZ and the mechanisms of tremor generation.

Our main conclusions are summarized in Figure 4.6.1 and described as follows:

1. Subduction-driven processes associated with slow slip events, represented here by the distribution of tremor and LFEs (white and red circles, respectively, in Figure 4.6.1), are depth dependent within and above the SZ model. At any given

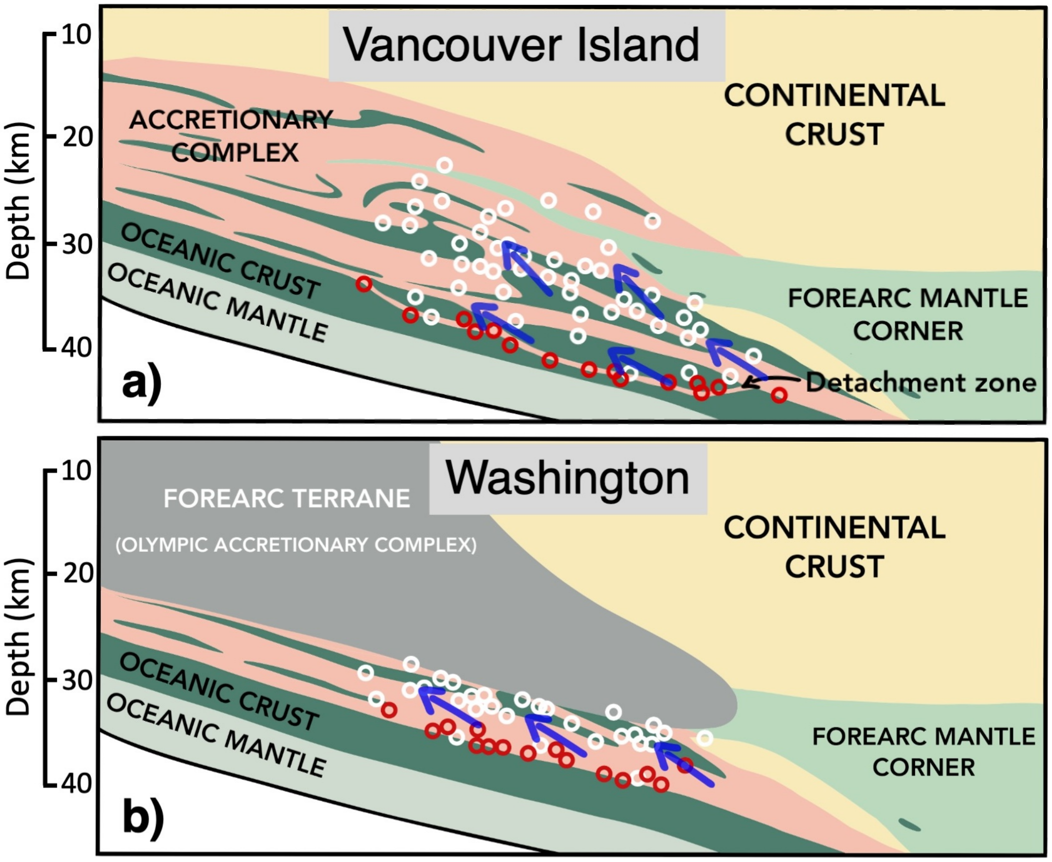

Figure 4.6.1: Cartoon diagrams of tremor and LFE situated in the subduction environment in (a) Vancouver Island and (b) Washington. Red and white circles denote LFEs and tremor, respectively. Coloured areas indicate distinct lithological features. Blue arrows indicate flow and direction of water. Design of the accretionary complex (pink region with green and yellow inclusions) is based on Figure 2 in Angiboust et al. (2021). Not to scale.

location, the vertical offset between LFEs and tremor is 5–10 km, wherein LFEs are systematically deeper, suggesting inherent differences in their generative processes. In S. Vancouver Island (Figure 4.6.1a), LFEs occur deep in the oceanic crust, potentially indicating crustal detachment within the downgoing plate (consistent with Bloch et al., 2023).

2. In the JdF Strait, tremor is localized as much as 10 km above the modelled oceanic crust, and LFEs exhibit southward shallowing within the oceanic crust. Considering results from the CASIE21 survey (Carbotte et al., 2024), we suggest that the location of the JdF Strait, which marks the apex of the oroclinal bend and a major transition in along-strike forearc lithology, may harbour large-scale deformational features, such as crustal tearing or overlapping, accommodated by

the weak JdF plate.

3. The depth range of tremor in N. Washington is restricted around the Olympic Accretionary Complex, which suggests that forearc lithology imposes significant constraints on the vertical extent of the accretionary complex and thus tremor (Figure 4.6.1b).

4. To place our observations in the context of previous work from a variety of disciplines, we propose that tremor and LFEs are generated by multiple mechanisms involving shear slip and extensional fracturing partly driven by dynamic changes in fluid pressure occurring in the accretionary complex. In this framework, the megathrust supports elevated strain rates in the accretionary complex above it, leading to structural complexity and compositional heterogeneity. In this case, high pore-fluid pressures in the ULVZ contribute to tremor generation, and the vertical distribution of tremor may be driven by the fluid-pressure gradient (vertical or sub-vertical) and structural constraints (pore spaces elongated in the direction of subduction strain). In addition, depth differences between tremor and LFEs suggest that there fundamental differences in their generating mechanisms, although more work is needed.

This work demonstrates considerable variation of tectonic tremor and LFE depths in relation to the SZ in N. Cascadia; as such, the specific interpretations enumerated above may not apply to other SZs where slow slip and tremor occur. However, there are four generalized conclusions that may be more globally applicable, which are: (1) independently constraining tremor source depths may reveal the distribution of active structures during slow slip events that is not evident from LFE sources alone; (2) tremor and LFEs may be generated by distinct sets of mechanisms that may be depth dependent; (3) the deep accretionary complex may play a role in generating tremor and accommodating slow slip-related deformation; and, (4) forearc lithology may provide constraints on the vertical distribution of tectonic tremor.

Chapter 5

Summary and Future Work

This chapter summarizes the scientific contributions of the three main chapters and discusses possible directions for future work based on the contents of this dissertation.

Chapter 2 defines and spatially characterizes tremor episodes ranging in size from 10 to more than 13,000 tremor events throughout N. Cascadia between 2006 and 2023. We find that tremor episodes representing ETS events—classified as major episodes—contain two thirds of all tremor but make up only 4% of episodes recurring every 10.5–15.5 months. ETS events have been a large focus of geophysics research since their discovery (Rogers and Dragert, 2003); therefore, the main scientific contribution of this chapter is its focus on minor tremor episodes. Minor episodes do not occur uniformly throughout N. Cascadia, and their heterogeneity in size, spatial distribution, and recurrence may reveal properties of the SZ that are not readily apparent in the study of major episodes. For example, the east coast of S. Vancouver Island exhibits a dearth of tremor activity during small and large episodes, demonstrating that this part of the SZ exhibits properties that favour tremor generation primarily during episodes of intermediate size (Figure 2.3.2). Precisely what geophysical properties cause this is a topic for future work. In addition, segmentation of tremor during major and minor episodes exists throughout S. Vancouver Island and S. Washington, creating along-dip tremor distributions that are bimodal around the FMC (Figure 2.4.3). In areas where the FMC is located near the downdip edge of the ETS zone, such as through the northern half of Washington, all tremor episodes occur updip of the FMC resulting in unimodal distributions of tremor. This regional correlation between the FMC and the distribution of major and minor tremor episodes is a novel result that may aid future researchers in discerning how geophysical properties of the FMC influence the character of tectonic tremor and SSEs.

Building upon Chapter 2, future work might define and characterize tremor asperities and their activation (or lack thereof) during tremor episodes. Maps of tremor from long-term catalogues (e.g., Figures 2.1.1, 2.3.3, 4.1.1, and C.0.3) exhibit clustering of events into high-density tremor patches, or asperities. The area noted above near the east coast of S. Vancouver Island may be one such asperity. Some case studies have already investigated the spatial clustering of tremor into asperities during three episodes in the N. Washington/JdF Strait area (e.g., Ghosh et al., 2012; Armbruster et al., 2014; Peng and Rubin, 2016). The episode catalogue produced in Chapter 2 could support an investigation into the activation of asperities across all major and minor episodes throughout the entire N. Cascadia region, including whether activation during minor episodes inhibits near-future activation in subsequent major episodes. Further, exploring the interaction between asperities might enhance our understanding of the relationship between minor and major episodes. Modelling from Luo and Liu (2021) suggests that major episodes are driven by cascades of minor episodes. This may suggest that the recurrence intervals of asperities preferentially activated during minor episodes (i.e., downdip of the FMC) control the initiation location and time of major episodes. Such analyses require regional, long-term catalogues that should be well supported by the work presented in Chapter 2.

Chapter 3 addresses the need for better constraints on tremor source depths and direct observation of tremor depth distributions. Many tremor catalogues either do not constrain source depths at all or exhibit poor depth resolution. This limitation of tremor localization often requires assuming that sources originate from a modelled surface representing the megathrust fault in order to discuss the relationship of tremor to the SZ. One notable example to the contrary is presented in La Rocca et al. (2010), where the authors use particle polarization and a cross-correlation procedure to locate tremor sources in S. Vancouver Island from P and S wave at three stations. Their localization results include probability density functions that estimate depth uncertainties of $\sim$ 2 km for ideally-situated events (i.e., directly beneath their station array); interestingly, many events localize up to 10 km shallower than the modelled subduction fault. However, this method is limited to small study areas and exhibits large horizontal uncertainties in the range of 10–20 km.

The DTBI workflow is designed to detect and locate tremor sources, and its effectiveness is demonstrated on regular earthquakes and tremor in Chapter 3. The primary scientific contribution of this work is the improved constraints on tremor sources compared to most previous work. Two important elements that support this outcome are: (1) the use of a 3D velocity model to compute traveltimes, thereby limiting systematic errors; and (2) robust estimation of localization uncertainties in a Bayesian framework that quantify probabilistic credibility intervals on each tremor source. A test performed on regular earthquakes demonstrates that DTBI can compute relocations with reasonable agreement to the official NRCan catalogue. This relocation test used 35 earthquakes and found that 89% of depth residuals were within 10 km (median of

5 km) of NRCan solutions; 90 earthquakes that were incidentally localized by DTBI in Chapter 4 replicate this result exactly. This test also finds that the median depth residual between NRCan and DTBI-relocated earthquakes is 3.6 km larger when the 1D NRCan velocity model is used compared to a 3D regional tomographic model.

Verifying DTBI's effectiveness with an earthquake relocation procedure is useful but suffers from several issues: (1) earthquake signals often exhibit clear P and S phase arrivals that can negatively influence (possibly even bias) waveform-envelope cross-correlation designed to use only shear waves; (2) because earthquake signals exhibit clear phase arrivals, using alternative information is expected to produce poorer results; and (3) very small earthquakes (<M2) are required for such a test, and uncertainties are likely to be larger on smaller earthquakes in the NRCan catalogue (although uncertainty estimates are not reported). In addition, the degree to which systematic error influences the NRCan catalogue resulting from the use of a 1D velocity model is unknown. Consequently, I consider earthquake relocation performed by DTBI to be somewhat informative, but limited. A more informative demonstration of DTBI's effectiveness is presented in Figure 3.3.7, where the distribution of tremor localized in the 2004 ETS event is compared to that in the SSA catalogue (Kao et al., 2009). This comparison shows that DTBI tremor events are just as numerous and more tightly clustered in horizontal and vertical dimensions than SSA tremor. Since errors tend to cause spatial scatter and wider distributions, a greater degree of spatial clustering therefore likely indicates a greater degree of accuracy.

There are at least three improvements that could be made to the DTBI method. First, additional testing and experimentation could be done to better characterize the nature of errors and biases on differential traveltimes. Analysis of exactly how a dataset of differential traveltimes is likely to be influenced by different factors and how the localization results are subsequently affected may help inform what procedures could be implemented to mitigate or correct these errors. Second, lowpass-filtered waveform-envelopes are currently the only information derived from seismograms. Other studies have demonstrated that particle-motion polarization and/or raypath backazimuth can provide reliable directional information (e.g., La Rocca et al., 2010; Armbruster et al., 2014) that may serve to improve localization results in DTBI. Finally, the computational workflow is inefficient because the entire program is implemented using Python without parallelization. On a 2021 MacBook Pro with 64 GB of RAM, an M1 Max processor, and 10 CPUs, processing one day of seismic data from 50–60 stations in the S. Vancouver Island study area may take 4–8 hours (using pre-computed traveltimes). Python libraries are convenient for seismic data processing and plotting results, but the numerical procedures (i.e., detection, dataset construction, and localization procedures) could run more efficiently in a lower-level, procedural programming language, such as C. Further, while some sequential processing is essential in order to manage seismic data on a daily basis, numerical procedures are grid-based operations that are highly parallelizable. Long computation times are a significant impedance to the convenience of using the DTBI method, and I expect large improvements are possible from these two changes alone.

Chapter 4 employs the DTBI method to localize tremor during 20 episodes across the S. Vancouver Island and Washington regions to explore tremor depth distributions in relation to LFEs, SZ structures, and the forearc crust. The primary scientific contribution of this chapter is the production and analysis of a tremor catalogue with unprecedented constraints on source depths on a regional scale. The DTBI tremor catalogue is represented as an average probability distribution over all tremor sources (each source is represented as a 3D PPD), which provides detailed depth information throughout the N. Cascadia region. This work directly investigates two commons ideas in the scientific literature: (1) tremor originates from the megathrust fault, often assumed to coincide with the top of the oceanic crust; and (2) tremor is composed of LFEs, and thus they should exhibit reasonable agreement in their overall spatial distributions. Instead, our observations reveal that tremor does not coincide strictly with the top of the oceanic crust, and that LFEs are localized 5–10 km deeper than the majority of tremor. We conclude that the primary geophysical environment that hosts tremor is the deep accretionary complex, which has been inferred and imaged in other work. In addition, the widespread depth differences between tremor and LFEs suggest that their generating mechanisms are at least partially distinct and dependent on distance from the downgoing plate. Given that much remains unknown about the deep accretionary complex and tremor-generating mechanisms, interpretations of our observations rely heavily on the wider scientific literature and include some informed speculations.

There are several directions for future work related to Chapter 4. First, seismic reflection and refraction surveys have revealed some SZ features in the ETS zone both onshore Vancouver Island and offshore through the JdF Strait and Puget Sound. Work that superimposes tremor sources over these imaged structures may provide additional insight into the relationship between tremor and the SZ. Second, some tremor in S. Vancouver Island appears approximately colocated with regular earthquakes in the forearc crust (Figure 4.3.1 transects A–C). Some active crustal faults have been inferred to extend to 30 km depth (such as the Leech River Fault zone; Li et al., 2018). If some processes related to SSEs (i.e., tremor) occur as shallow as 20 km, or even 15 km, forearc faults may influence such processes. Conversely, conditions that contribute to tremor generation (e.g., water pressure or strain diffusion) may influence conditions on forearc faults that increase the likelihood of triggering seismicity; observations in the Hikurangi SZ do indeed demonstrate that SSEs increase seismicity rates during and after the event (Yarce et al., 2023). Finally, there are currently no rigorous definitions of a tremor event; in Chapter 4, we describe tremor simply as low-frequency, emergent seismic waveforms. Such a definition leaves much to be desired. One way to resolve this issue may be to more rigorously understand the similarities and differences between tremor and LFEs, insofar as this may provide insight into the physical processes that generate them.

The work in this dissertation uses tectonic tremor to explore properties and behaviours of the N. Cascadia SZ. In Chapter 2 I demonstrated that the FMC is a primary factor that affects (or controls) the distribution of major and minor tremor episodes. This result indicates that the geophysical conditions landward of the FMC facilitate more-frequent, shorter-duration tremor episodes. The DTBI method presented in Chapter 3 localizes tremor with improved depth constraints over previously-existing methods and facilitates rigorous probabilistic uncertainty estimates on tremor sources. The DTBI method is used to compute a catalogue of tremor sources that are presented in Chapter 4 in relation to LFEs and key SZ features. The detailed depth distributions of tremor presented here reveal that tremor occurs within a volume corresponding to the deep accretionary complex up to 10 km shallower than the top of the oceanic crust. This work also demonstrates that LFEs do not typically occur at the same depths as tremor, suggesting fundamental differences in their generative processes. These insights into the spatial distribution of tremor, particularly in depth, may aid future researchers in exploring the mechanisms that generate tectonic tremor and the relationship between tremor and slip. Answering these open questions are essential to understanding SZs and their potential impacts on human populations.

Appendix A
Supplement to Chapter 2

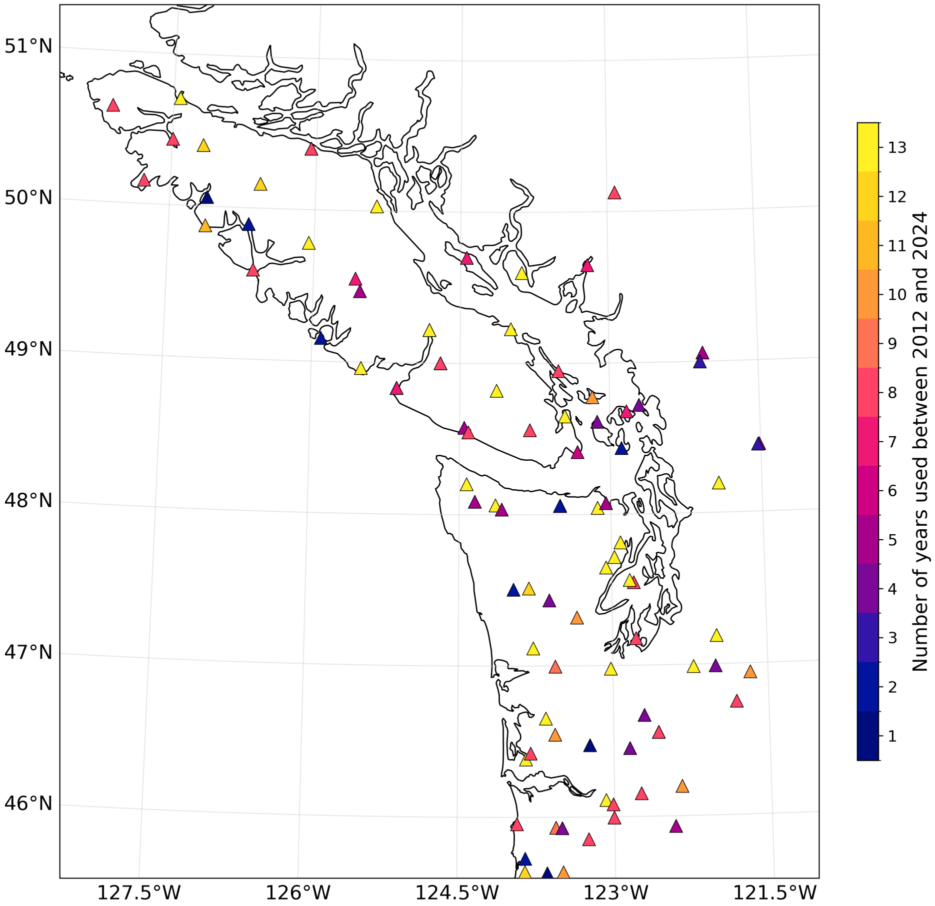

Figure A.0.1: All seismic stations (coloured triangles) used to compute the PNSN tremor catalog between the years 2012 and 2024 in N. Cascadia. Stations are coloured by the number of years they were queried for data regardless of whether they were operational at any given time. As such, colours represent the maximum amount of time for which stations were used to localize tremor events. Information in this figure, which is unavailable for years prior to 2012, was provided by Aaron Wech through personal communication.

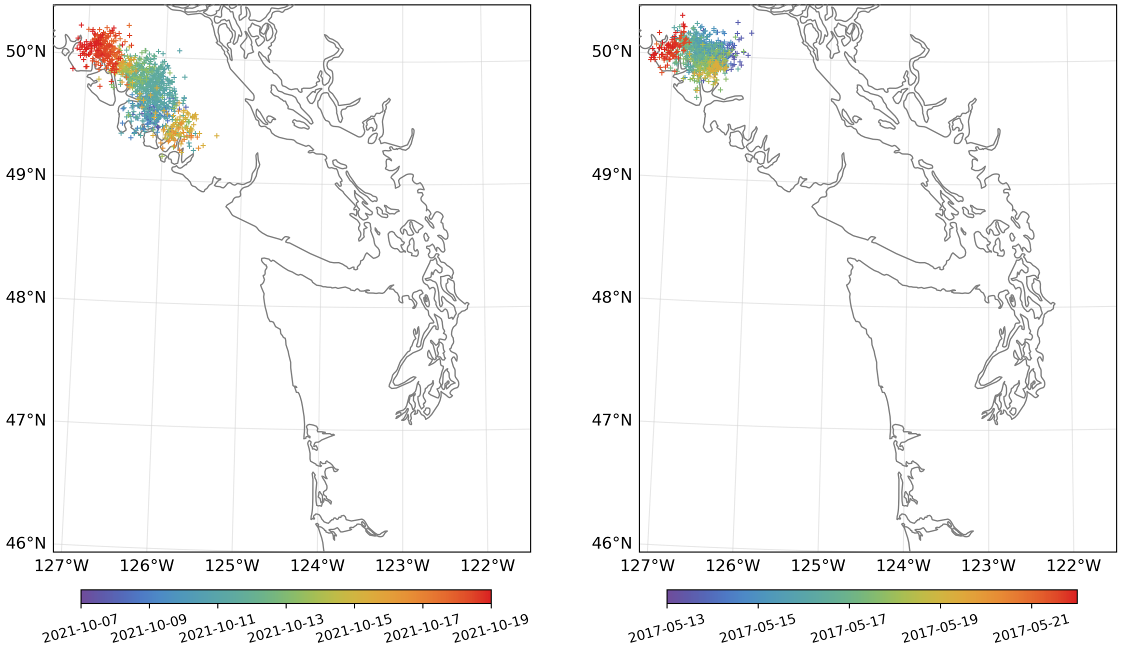

Figure A.0.2: Two examples of minor episodes in northern Vancouver Island that may be considered ETS events (i.e., major episodes). Panels left to right show episodes containing approximately 900 and 1200 events, respectively, occurring in 2017–05 and 2021–10.

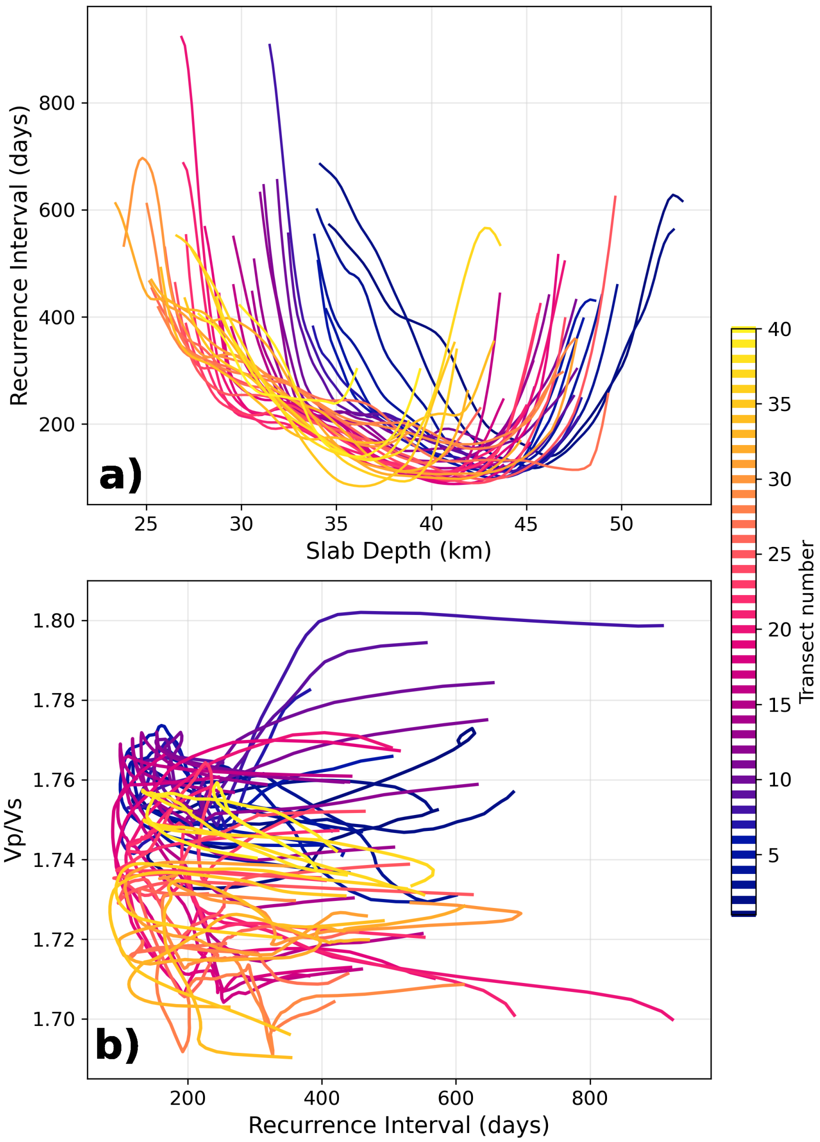

Figure A.0.3: Same Figure 2.4.2 but with datasets extracted along transects through the entire tremor zone rather than just the ETS zone (where recurrence intervals are > 450 days) and plotted with respect to slab depth rather than slab depth increase.

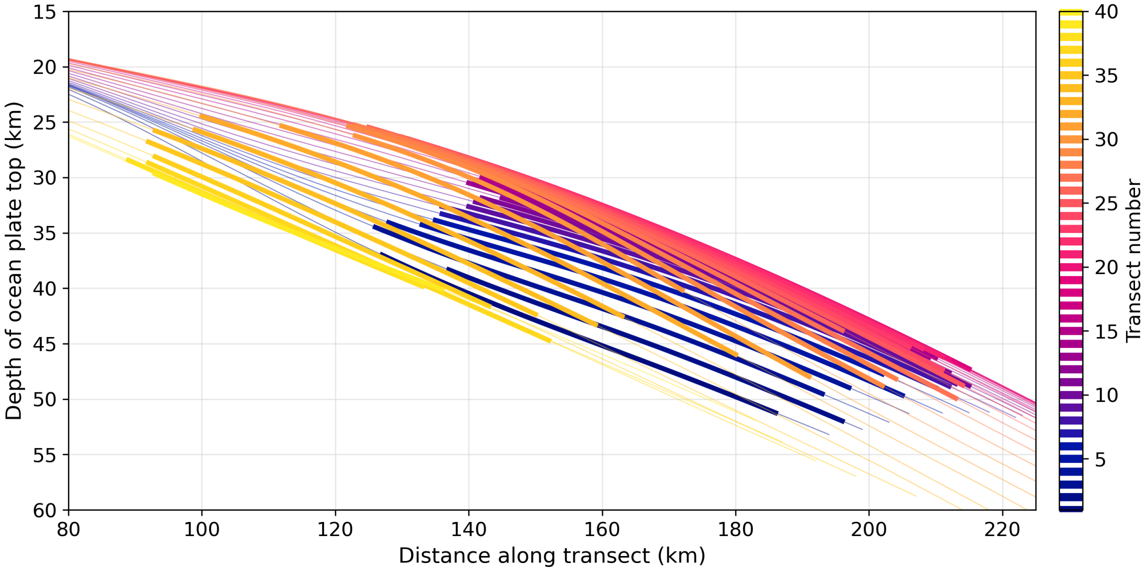

Figure A.0.4: Depth to oceanic crust along 40 margin-perpendicular transects shown in Figure 2.4.1. Thick lines indicate the portion of the interpolated slab surface in the ETS zone (i.e., where recurrence intervals are $\leq$ 450 days).

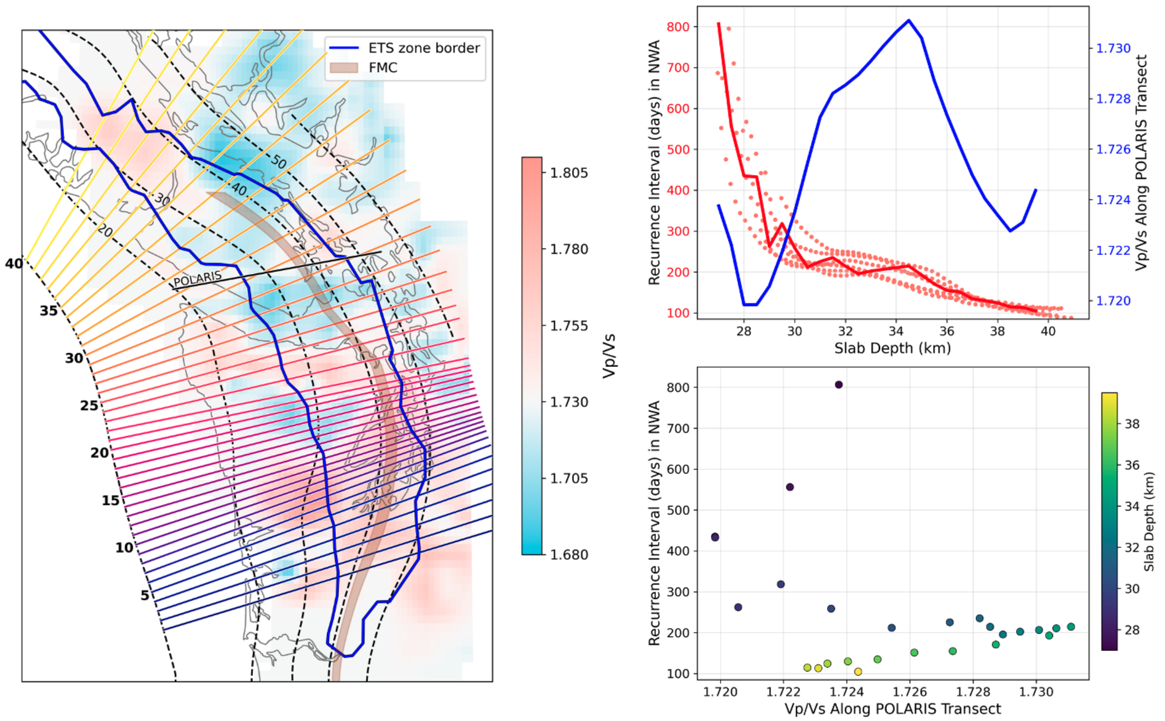

Figure A.0.5: (left) same as Figure 2.4.1 with the addition of the POLARIS transect in S. Vancouver Island (black line). (right, top) forearc Vp/Vs along the POLARIS transect (blue line) and tremor episode recurrence intervals along transects 17–23 in N. Washington (red dots fit with a red line) as a function of slab depth. (right, bottom) recurrence intervals (red line in the top panel) as a function of forearc Vp/Vs (blue line from the top panel) coloured by slab depth. This figure is meant to replicate the findings of Audet and Bürgmann (2014) as closely as possible using the datasets presented in the main text.

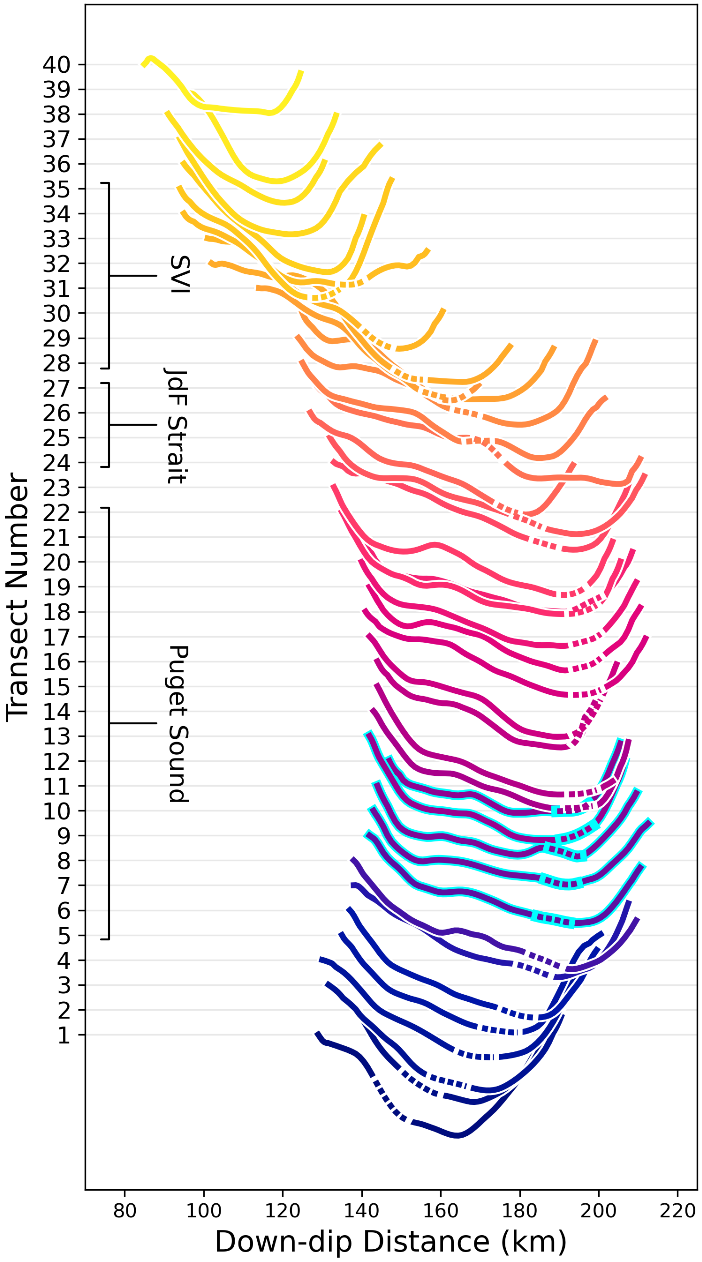

Figure A.0.6: Same as Figure 2.4.3a but showing relative recurrence intervals for all tremor episodes in the tremor zone rather than number of tremor events. The location of the FMC is denoted by the dotted portion of the lines.

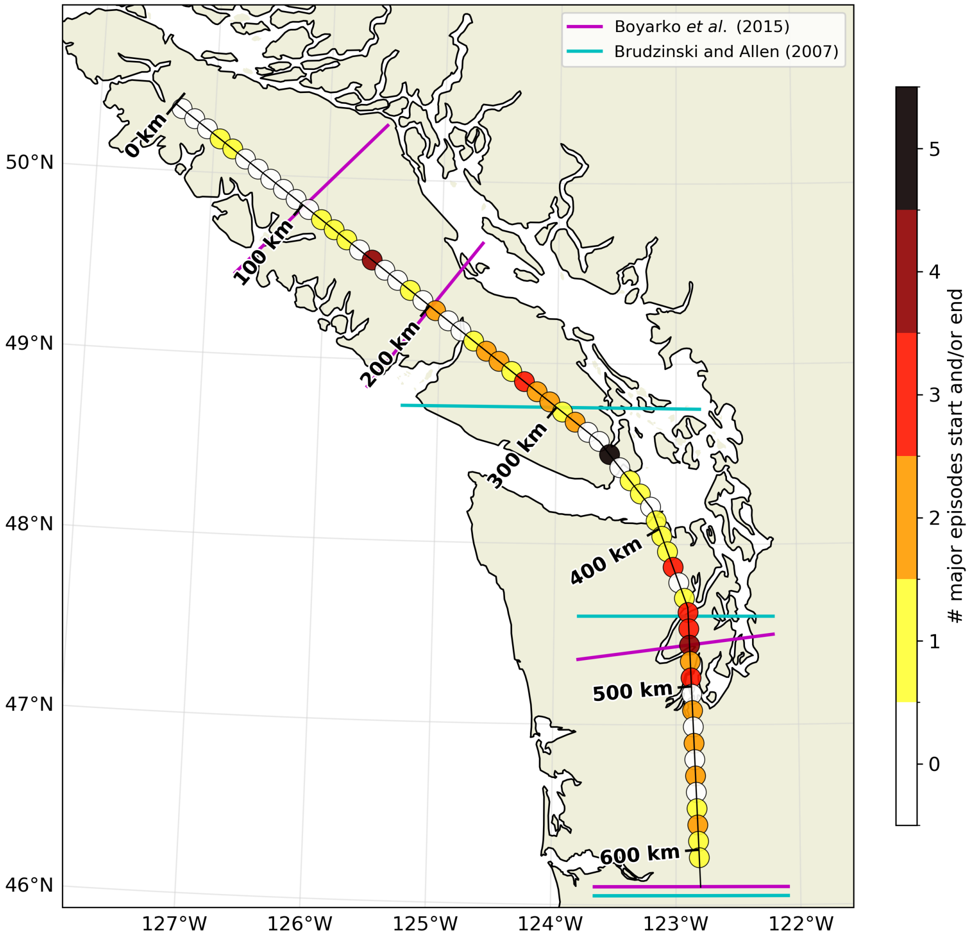

Figure A.0.7: Number of major episodes beginning or ending in 10-km along-strike bins (coloured circles), 18 of which occur in the central Puget Sound area discussed in the main text. Teal and purple lines denote segment boundaries from Brudzinski and Allen (2007) and Boyarko et al. (2015), respectively. Start and end points for episodes are defined as the position along strike of the first and last tremor event, respectively, in each episode.

This figure is intended to provide supplementary information for the discussion in Section 2.4.2 in the main text. We caution against over interpreting segmentation boundaries derived from the episode catalog presented in the main text because the begin and end locations of episodes are determined from individual tremor events that occur earliest and latest in episodes; a more rigorous analysis of segment boundaries should account for the scatter in the PNSN catalog by using a different determinant of begin and end locations (e.g., centroids).

Nonetheless, this figure hints at an interesting characteristic of ETS events that has not been discussed yet in the literature and warrants more investigation. This is the fact that the JdF Strait area sometimes acts as a barrier to or initiation of along-strike migration of major episodes. The one bin in the JdF Strait in which 5 episodes began and/or ended is actually comprised of 4 episodes, one of which both began and ended at this location, 3 of which began at this location. These 4 episodes are more recent than 2018. In addition to these episodes, there are 4 more major episodes in our catalog that appear to jump or avoid this area (two close in time late 2014, and two close in time early 2017). Based on this preliminary analysis, 8 of the 15–20 major episodes occurring in the S. Vancouver Island – N. Washington area are impeded or initiated in/near the JdF Strait.

Appendix B

Supplement to Chapter 3

Table B.0.1: Seismic stations used to relocate earthquakes in this study provided by the Canadian National Seismograph Network (CN), Pacific Northwest Seismic Network (UW), and Pacific Boundary Observatory Borehole Seismic Network (PB).

Network	Station name	Latitude	Longitude	Elevation [m]
CN	WPB	49.6478	-123.2094	260.0
CN	CBB	50.0315	-125.365	277.0
CN	BTB	49.4686	-125.5226	1607.0
CN	GHNB	49.3065	-124.2364	5.0
CN	BFSB	48.8336	-125.136	33.0
CN	GOBB	48.9493	-123.5105	173.0
CN	WOSB	50.1608	-126.5704	961.0
CN	MGRB	48.9997	-124.6971	1310.0
CN	NLLB	49.227	-123.988	199.0
CN	NTKA	49.5924	-126.6166	12.0
CN	PABB	49.2188	-124.8114	36.0
CN	PTRF	48.544	-124.413	164.0
CN	SHB	49.5985	-123.8771	1129.0
CN	SHPB	49.3476	-126.2598	26.0
CN	SNB	48.775	-123.172	402.0
CN	SYMB	48.559	-123.799	945.0
CN	TXDB	49.6979	-124.437	501.0
CN	VGZ	48.413	-123.325	67.0
CN	CLRS	48.82	-124.131	174.0
CN	GDR	49.7805	-126.0557	123.0
PB	B001	48.043	-123.131	237.0
PB	B010	48.6502	-123.4513	5.0
PB	B012	48.9246	-125.542	13.0
PB	B014	47.5133	-123.8125	64.7
PB	B926	48.8202	-124.1312	191.6
PB	B927	49.2188	-124.8113	39.0
PB	B011	48.6495	-123.4482	22.0
PB	B928	48.8337	-125.1345	9.5
PB	B007	48.0576	-123.5041	293.0
PB	B013	47.813	-122.9108	75.3

PB	B006	48.059	-123.501	302.0
PB	B004	48.2019	-124.427	30.0
PB	B003	48.0624	-124.1409	284.7
UW	SLDQ	48.062	-124.141	297.0
UW	SWID	48.0129	-122.411	62.0
UW	PABH	47.2128	-124.2045	36.0
UW	QKTN	47.8086	-122.5293	30.7
UW	TAHO	47.3444	-124.2875	6.4
UW	QJLF	48.9851	-122.743	13.5
UW	QGBP	48.7334	-122.6676	4.0
UW	QCDG	48.1	-122.587	52.2
UW	WISH	47.117	-123.7712	45.0
UW	STW	48.151	-123.671	308.0
UW	ERW	48.4538	-122.6261	387.0
UW	OHC	47.3326	-123.1588	11.0
UW	DOSE	47.717	-122.972	53.0
UW	EVCC	48.0063	-122.2036	38.0
UW	EVGW	47.8542	-122.1546	152.4
UW	FMW	46.9419	-121.6715	1900.0
UW	FORK	47.948	-124.566	44.9
UW	CORE	46.9257	-123.9136	46.0
UW	BLN	48.0066	-122.9726	601.0
UW	GNW	47.564	-122.825	220.0
UW	OOW2	47.7492	-124.1754	741.0
UW	BEVT	47.925	-122.2781	174.09
UW	KIMR	47.5027	-122.7686	121.81
UW	LCMC	47.4449	-123.1874	744.0
UW	LUMI	48.7201	-122.7063	19.4
UW	MKAH	48.371	-124.589	18.0
UW	NMRF	47.4326	-122.9828	147.81
UW	OCEN	46.9525	-124.1595	4.0
UW	OCP	48.298	-124.625	487.0
UW	HURR	47.97	-123.499	1605.0
UW	JCW	48.1953	-121.9275	792.0

Table B.0.2: Seismic stations used to locate tremor in this study provided by the Canadian National Seismograph Network (CN), Canadian Seismic Research Network (C8), Pacific Northwest Seismic Network (UW), Pacific Boundary Observatory Borehole Seismic Network (PB), and Portable Observatories for Lithospheric Analysis and Research Investigating Seismicity (PO) array.

Network	Station name	Latitude	Longitude	Elevation [m]
C8	TWBB	48.5846	-124.092	122.0
C8	THAB	49.28	-124.9184	115.0
C8	SHVB	48.4723	-123.636	69.0
C8	CPLB	48.6118	-124.7512	40.0
C8	PHYB	49.0828	-123.8431	39.0
C8	GLBC	48.396	-123.6363	100.0
C8	JRBC	48.3957	-123.96	20.0
C8	MGCB	48.6317	-123.6808	236.0
CN	VGZ	48.4131	-123.3251	67.0
CN	GHNB	49.3065	-124.2364	5.0
CN	LZB	48.6122	-123.824	794.0
CN	MGB	48.9999	-124.697	1310.0
CN	OZB	48.9612	-125.4978	626.0
CN	YOUB	48.901	-124.2618	771.0
CN	PGC	48.6498	-123.4521	12.0
CN	SHB	49.5985	-123.8771	1129.0
CN	SNB	48.7751	-123.1723	402.0
CN	NLLB	49.2271	-123.9882	199.0
CN	PFB	48.5747	-124.4541	449.0
PB	B007	48.0576	-123.5041	293.0
PB	B006	48.0588	-123.5008	302.0
PB	B005	48.0595	-123.5033	302.7
PB	B003	48.0624	-124.1409	284.7
PB	B001	48.0431	-123.1314	237.0
PO	TWKB	48.6448	-123.7332	128.0
PO	KLNB	48.6611	-123.5706	0.0
PO	SILB	48.602	-123.2815	76.0
PO	SSIB	48.7558	-123.3875	12.0
PO	TSJB	48.6013	-123.9885	378.0
UW	ERW	48.4538	-122.6261	387.0

Table B.0.3: Catalogued earthquakes from NRCan (left) within the study area during 2019 relocated using the DTBI method and a 3D velocity model (right). Horizontal lines indicate events that were not successfully relocated.

Time [UTC]	Latitude	Longitude	Depth [km]	M_L	Latitude	Longitude	Depth [km]	NS CI [km]	EW CI [km]	Depth CI [km]
2019-01-01 13:16:22.0	48.12	-123.27	45.0	0.42	48.17	-123.30	29	3	2	4
2019-01-16 09:29:24.7	48.50	-123.28	24.7	1.8	48.51	-123.29	20	2	2	3
2019-01-17 03:47:06.7	48.13	-123.29	45.1	2.62	48.14	-123.25	34	2	2	3
2019-01-18 08:43:33.2	48.43	-123.31	47.89	0.81	48.44	-123.31	38	1	2	3
2019-01-21 00:40:53.5	48.46	-123.46	15.56	1.32	48.48	-123.44	14	1	2	3
2019-02-14 00:07:29.2	48.64	-123.83	22.27	0.84	48.66	-123.80	20	2	2	3
2019-02-24 11:44:53.3	48.58	-123.09	10.5	0.66	——	——	–	–	–	–
2019-02-28 04:07:54.3	48.45	-123.31	10.25	-0.07	——	——	–	–	–	–
2019-03-05 07:48:03.6	48.20	-123.20	40.9	1.31	48.21	-123.18	36	2	3	5
2019-03-11 03:30:16.3	48.97	-125.36	29.77	0.38	——	——	–	–	–	–
2019-04-05 19:52:12.8	48.59	-123.10	17.13	1.9	——	——	–	–	–	–
2019-04-05 20:04:03.6	48.59	-123.09	15.66	2.04	——	——	–	–	–	–
2019-04-05 22:58:05.6	48.59	-123.09	19.73	1.79	——	——	–	–	–	–
2019-04-10 00:48:57.9	48.67	-123.54	14.49	-0.05	——	——	–	–	–	–
2019-04-10 07:39:50.4	48.59	-123.09	15.87	1.39	——	——	–	–	–	–
2019-04-15 02:28:34.1	48.42	-123.59	17.82	0.74	48.42	-123.60	11	2	1	4
2019-05-05 06:26:34.4	48.35	-123.40	38.84	1.32	48.37	-123.40	31	2	2	4
2019-05-15 18:40:31.3	48.28	-123.54	35.91	0.88	48.31	-123.52	28	1	2	5
2019-05-20 20:35:56.5	48.22	-124.38	34.62	2.08	48.21	-124.42	37	3	3	4
2019-06-15 20:52:26.8	48.17	-123.29	42.27	1.52	48.17	-123.29	43	3	2	3
2019-06-18 18:00:52.0	48.85	-125.56	29.83	1.15	——	——	–	–	–	–
2019-07-01 23:05:39.9	48.49	-123.54	25.69	0.2	48.48	-123.55	19	1	2	4
2019-07-11 02:13:15.1	48.81	-125.17	14.2	1.45	48.83	-125.19	9	3	3	3
2019-07-18 20:19:36.8	48.65	-123.61	12.3	0.54	——	——	–	–	–	–
2019-07-22 07:12:21.2	48.44	-123.26	24.44	0.83	48.46	-123.23	17	2	3	5
2019-07-22 09:11:12.2	48.47	-123.54	17.67	0.52	48.48	-123.55	12	1	2	4
2019-07-22 09:48:57.7	48.99	-125.02	38.03	0.41	48.98	-125.03	29	2	2	4
2019-07-29 00:34:25.5	48.47	-123.54	23.16	0.22	48.48	-123.53	20	2	3	6
2019-08-17 08:56:55.6	48.05	-124.58	43.6	1.27	——	——	–	–	–	–

2019-08-17 21:36:29.0	48.51	-123.53	22.27	0.88	48.51	-123.53	18	1	2	3
2019-08-25 21:11:56.6	48.71	-123.52	18.41	0.32	48.73	-123.52	14	1	1	2
2019-08-31 02:34:32.0	48.67	-124.54	35.1	0.48	48.68	-124.59	42	2	2	4
2019-08-31 08:11:36.3	48.51	-123.12	52.21	0.31	48.51	-123.18	30	2	3	5
2019-09-06 20:54:02.1	48.15	-123.24	23.08	0.99	48.16	-123.17	28	2	3	6
2019-09-12 01:58:13.7	48.46	-123.28	21.54	0.36	48.48	-123.23	16	2	3	3
2019-09-13 20:54:07.3	48.92	-123.59	22.12	0.78	——	——	–	–	–	–
2019-09-14 03:33:25.0	48.80	-125.17	15.09	1.47	——	——	–	–	–	–
2019-09-14 03:33:25.0	48.80	-125.17	15.09	1.47	48.83	-125.21	8	2	3	3
2019-09-14 22:18:53.1	48.60	-123.64	22.24	0.21	48.61	-123.63	19	2	2	3
2019-09-24 11:24:49.5	48.73	-125.04	13.14	1.3	——	——	–	–	–	–
2019-09-26 10:06:41.2	48.89	-124.00	17.6	1.77	48.89	-124.04	15	3	2	4
2019-10-08 14:06:12.3	48.73	-125.04	12.92	1.2	——	——	–	–	–	–
2019-10-11 01:35:12.6	48.49	-123.64	25.01	0.05	48.50	-123.65	15	1	1	2
2019-10-11 21:58:37.8	48.18	-123.47	21.28	0.95	48.20	-123.45	15	2	1	3
2019-10-20 18:20:58.6	48.60	-124.46	38.49	1.88	48.62	-124.48	38	2	3	4
2019-10-23 03:04:48.8	48.20	-123.26	21.4	1.11	48.25	-123.18	18	2	3	4
2019-10-23 10:40:45.1	48.78	-124.65	37.48	1.74	48.78	-124.69	32	2	2	4
2019-10-31 14:18:55.8	48.81	-123.50	11.63	0.05	——	——	–	–	–	–
2019-11-03 23:45:58.3	48.46	-123.33	16.9	0.27	——	——	–	–	–	–
2019-11-04 11:40:49.1	48.73	-125.17	15.94	0.75	——	——	–	–	–	–
2019-11-04 14:16:12.2	48.80	-125.15	16.72	0.64	——	——	–	–	–	–
2019-11-06 06:40:43.2	48.79	-125.14	15.75	1.0	——	——	–	–	–	–
2019-11-10 07:03:23.6	48.80	-125.19	12.34	1.12	48.83	-125.18	8	3	2	2
2019-12-07 21:42:38.0	48.13	-123.46	40.6	0.95	48.14	-123.41	36	2	2	4
2019-12-08 05:52:07.7	48.58	-123.38	49.13	0.01	——	——	–	–	–	–
2019-12-19 03:38:28.2	48.70	-125.07	29.37	2.07	——	——	–	–	–	–
2019-12-24 06:39:31.3	48.46	-123.22	21.56	0.39	48.48	-123.21	14	2	3	4
2019-12-31 17:13:50.7	48.58	-123.09	13.82	2.17	——	——	–	–	–	–

Appendix C
Supplement to Chapter 4

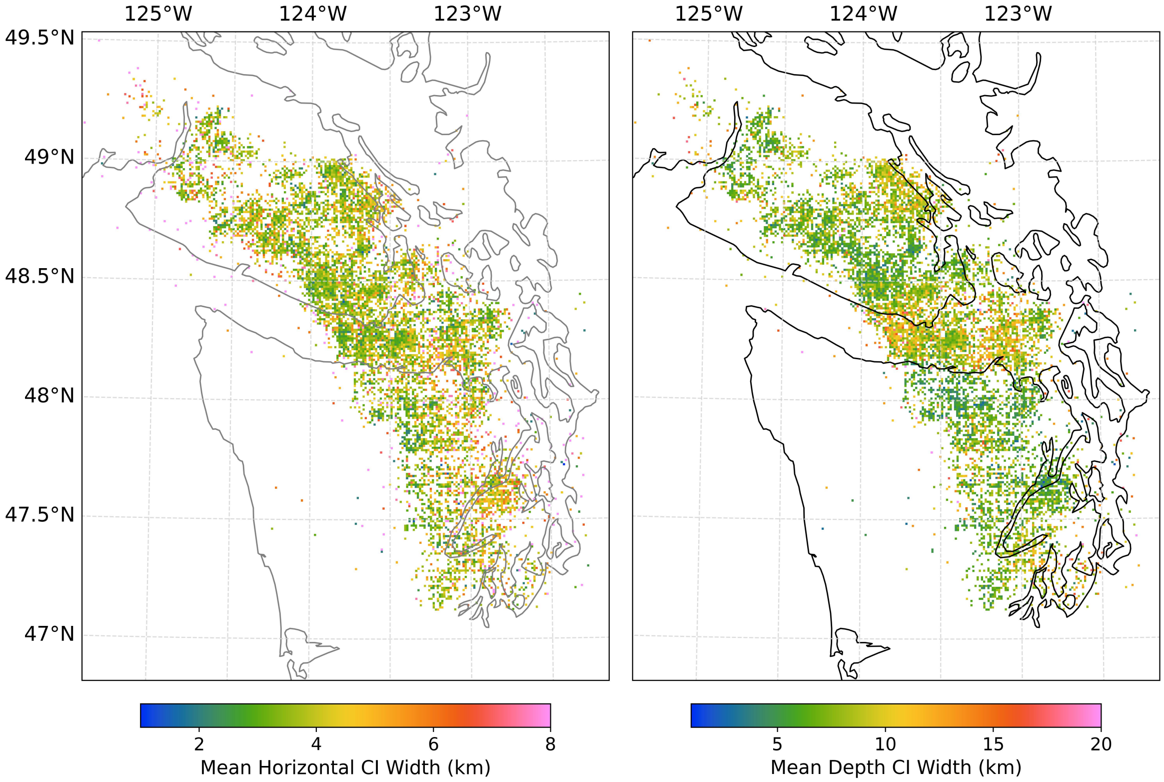

Figure C.0.1: Mean horizontal (NS and EW combined) and depth uncertainties in the DTBI catalogue. Uncertainties are quantified as minimum-width 95% credibility intervals (CIs) of individual events. Note the different colour scales for each panel.

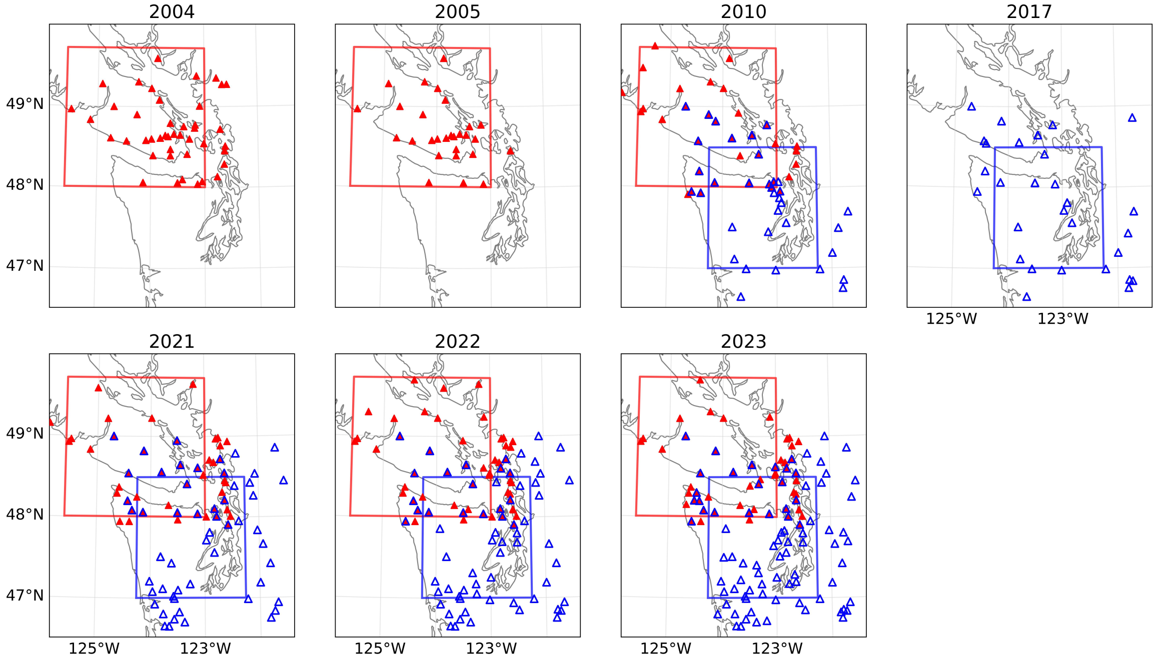

Figure C.0.2: Supplementary figure of the study areas for Vancouver Island (red polygon) and Washington (blue polygon) and the stations used to localize tremor within each for selected years (Table 4.2.1 in the main text). Seismic stations are represented by red solid triangles if they are used to localize tremor in the Vancouver Island study area or blue empty triangles if used in the Washington study area; some stations are used in both study areas (solid red triangles with blue outline).

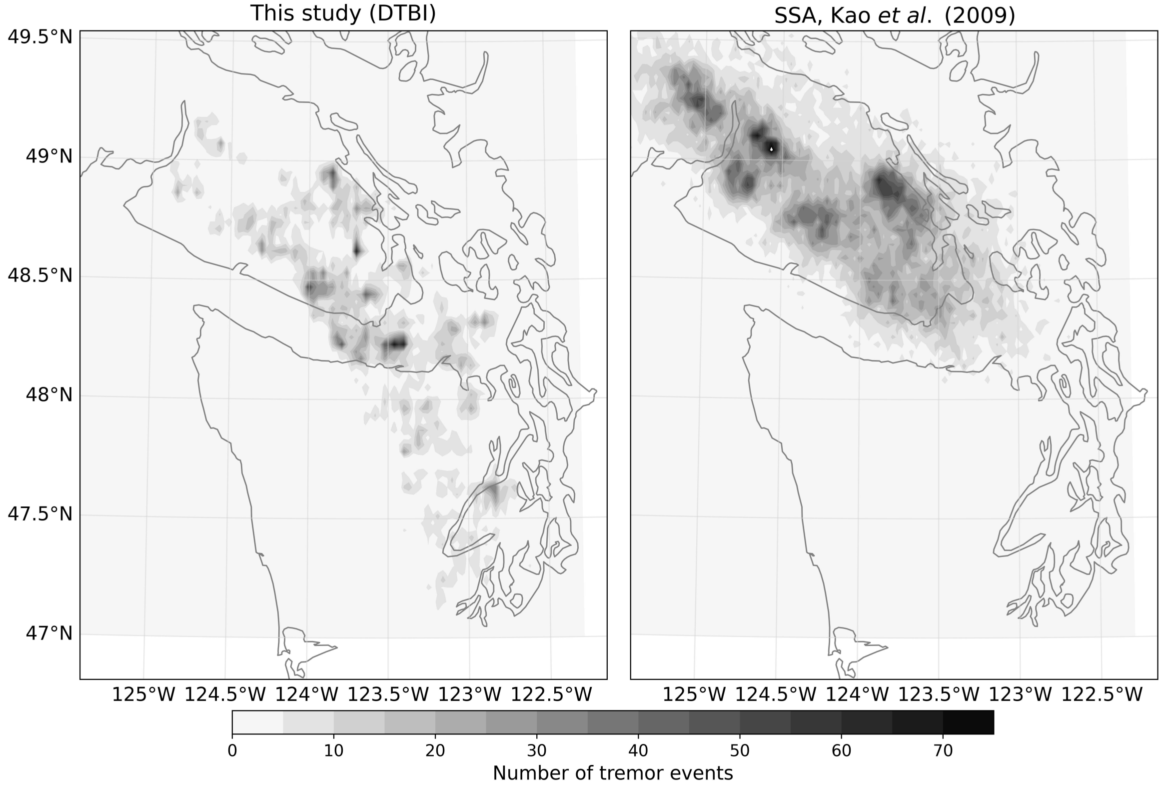

Figure C.0.3: Supplementary figure of (left) the DTBI tremor catalogue (considered as point sources) over the time periods given in Table 4.2.1 in the main text, and (right) the SSA tremor catalogue spanning the years 1997 to 2012. Both are represented as histograms showing the number of tremor events in geographic units approximately 9 km^2.

Bibliography

Aldrich, M. J. (2021). Structural styles, deformation, and uplift of the Olympic Mountains, Washington: Implications for accretionary wedge deformation. *GSA Bulletin*, 133(11-12):2567–2581.

Angiboust, S., Menant, A., Gerya, T., and Oncken, O. (2021). The rise and demise of deep accretionary wedges: A long-term field and numerical modeling perspective. *Geosphere*, 18(1):69–103.

Armbruster, J. G., Kim, W.-Y., and Rubin, A. M. (2014). Accurate tremor locations from coherent S and P waves. *Journal of Geophysical Research: Solid Earth*, 119(6):5000–5013.

Audet, P., Bostock, M. G., Boyarko, D. C., Brudzinski, M. R., and Allen, R. M. (2010). Slab morphology in the Cascadia fore arc and its relation to episodic tremor and slip. *Journal of Geophysical Research: Solid Earth*, 115(B4):B00A16.

Audet, P., Bostock, M. G., Christensen, N. I., and Peacock, S. M. (2009). Seismic evidence for overpressured subducted oceanic crust and megathrust fault sealing. *Nature*, 457(7225):76–78.

Audet, P. and Bürgmann, R. (2014). Possible control of subduction zone slow-earthquake periodicity by silica enrichment. *Nature*, 510(7505):389–392.

Audet, P. and Kim, Y. (2016). Teleseismic constraints on the geological environment of deep episodic slow earthquakes in subduction zone forearcs: A review. *Tectonophysics*, 670:1–15.

Bartlow, N. M. (2020). A long-term view of episodic tremor and slip in Cascadia. *Geophysical Research Letters*, 47(3):e2019GL085303.

Bartlow, N. M., Miyazaki, S., Bradley, A. M., and Segall, P. (2011). Space-time correlation of slip and tremor during the 2009 Cascadia slow slip event. *Geophysical Research Letters*, 38(18):L18309.

Bassett, D. and Watts, A. B. (2015). Gravity anomalies, crustal structure, and seismicity at subduction zones: 2. interrelationships between fore-arc structure and seismogenic behavior. *Geochemistry, Geophysics, Geosystems*, 16(5):1541–1576.

Behr, W. M. and Bürgmann, R. (2021). What's down there? The structures, materials and environment of deep-seated slow slip and tremor. *Philosophical Transactions of the Royal Society A: Mathematical, Physical and Engineering Sciences*, 379(2193):20200218.

Benson, P. M., Austria, D. C., Gehne, S., Butcher, E., Harnett, C. E., Fazio, M., Rowley, P., and Tomas, R. (2020). Laboratory simulations of fluid-induced seismicity, hydraulic fracture, and fluid flow. *Geomechanics for Energy and the Environment*, 24:100169.

Bernaudin, M. and Gueydan, F. (2018). Episodic tremor and slip explained by fluid-enhanced microfracturing and sealing. *Geophysical Research Letters*, 45(8):3471–3480.

Beroza, G. C. and Ide, S. (2011). Slow earthquakes and nonvolcanic tremor. *Annual Review of Earth and Planetary Sciences*, 39(Volume 39, 2011):271–296.

Bloch, W., Bostock, M. G., and Audet, P. (2023). A Cascadia slab model from receiver functions. *Geochemistry, Geophysics, Geosystems*, 24(10):e2023GC011088.

Bombardier, M. (2024). Episode metadata. *Zenodo*.

Bombardier, M., Cassidy, J. F., Dosso, S. E., and Kao, H. (2024). Spatial distribution of tremor episodes from long-term monitoring in the northern cascadia subduction zone. *Journal of Geophysical Research: Solid Earth*, 129(8):e2024JB029159.

Bombardier, M., Dosso, S. E., Cassidy, J. F., and Kao, H. (2023). Tackling the challenges of tectonic tremor localization using differential traveltimes and Bayesian inversion. *Geophysical Journal International*, 234(1):479–493.

Bostock, M. G. (2013). The Moho in subduction zones. *Tectonophysics*, 609:547–557.

Bostock, M. G., Christensen, N. I., and Peacock, S. M. (2019). Seismicity in Cascadia. *Lithos*, 332-333:55–66.

Bostock, M. G., Royer, A. A., Hearn, E. H., and Peacock, S. M. (2012). Low frequency earthquakes below southern Vancouver Island. *Geochemistry, Geophysics, Geosystems*, 13(11):Q11007.

Bostock, M. G., Thomas, A. M., Savard, G., Chuang, L., and Rubin, A. M. (2015). Magnitudes and moment-duration scaling of low-frequency earthquakes beneath southern Vancouver Island. *Journal of Geophysical Research: Solid Earth*, 120(9):6329–6350.

Boyarko, D., Brudzinski, M., Porritt, R., Allen, R., and Tréhu, A. (2015). Automated detection and location of tectonic tremor along the entire Cascadia margin from 2005 to 2011. *Earth and Planetary Science Letters*, 430:160–170.

Brown, J. R., Beroza, G. C., Ide, S., Ohta, K., Shelly, D. R., Schwartz, S. Y., Rabbel, W., Thorwart, M., and Kao, H. (2009). Deep low-frequency earthquakes in tremor localize to the plate interface in multiple subduction zones. *Geophysical Research Letters*, 36(19):L19306.

Brudzinski, M. R. and Allen, R. M. (2007). Segmentation in episodic tremor and slip all along Cascadia. *Geology*, 35(10):907–910.

Bürgmann, R. (2018). The geophysics, geology and mechanics of slow fault slip. *Earth and Planetary Science Letters*, 495:112–134.

Calvert, A. J., Bostock, M. G., Savard, G., and Unsworth, M. J. (2020). Cascadia low frequency earthquakes at the base of an overpressured subduction shear zone. *Nature Communications*, 11(1):3874.

Calvert, A. J., Preston, L. A., and Farahbod, A. M. (2011). Sedimentary underplating at the Cascadia mantle-wedge corner revealed by seismic imaging. *Nature Geoscience*, 4(8):545–548.

Calvert, A. J., Ramachandran, K., Kao, H., and Fisher, M. A. (2006). Local thickening of the Cascadia forearc crust and the origin of seismic reflectors in the uppermost mantle. *Tectonophysics*, 420(1):175–188.

Carbotte, S. M., Boston, B., Han, S., Shuck, B., Beeson, J., Canales, J. P., Tobin, H., Miller, N., Nedimovic, M., Tréhu, A., Lee, M., Lucas, M., Jian, H., Jiang, D., Moser, L., Anderson, C., Judd, D., Fernandez, J., Campbell, C., Goswami, A., and Gahlawat, R. (2024). Subducting plate structure and megathrust morphology from deep seismic imaging linked to earthquake rupture segmentation at Cascadia. *Science Advances*, 10(23):eadl3198.

Chestler, S. R. and Creager, K. C. (2017). A model for low-frequency earthquake slip. *Geochemistry, Geophysics, Geosystems*, 18(12):4690–4708.

Clowes, R. M., Baird, D. J., and Dehler, S. A. (1997). Crustal structure of the Cascadia subduction zone, southwestern British Columbia, from potential field and seismic studies. *Canadian Journal of Earth Sciences*, 34(3):317–335.

Clowes, R. M., Brandon, M. T., Green, A. G., Yorath, C. J., Brown, A. S., Kanasewich, E. R., and Spencer, C. (1987). LITHOPROBE—southern Vancouver Island: Cenozoic subduction complex imaged by deep seismic reflections. *Canadian Journal of Earth Sciences*, 24(1):31–51.

Condit, C. B. and French, M. E. (2022). Geologic evidence of lithostatic pore fluid pressures at the base of the subduction seismogenic zone. *Geophysical Research Letters*, 49(12):e2022GL098862.

Condit, C. B., Guevara, V. E., Delph, J. R., and French, M. E. (2020). Slab dehydration in warm subduction zones at depths of episodic slip and tremor. *Earth and Planetary Science Letters*, 552:116601.

Davis, E. E., Sun, T., Heesemann, M., Becker, K., and Schlesinger, A. (2023). Long-term offshore borehole fluid-pressure monitoring at the northern Cascadia subduction zone and inferences regarding the state of megathrust locking. *Geochemistry, Geophysics, Geosystems*, 24(6):e2023GC010910.

Delph, J. R., Thomas, A. M., and Levander, A. (2021). Subcretionary tectonics: Linking variability in the expression of subduction along the Cascadia forearc. *Earth and Planetary Science Letters*, 556:116724.

Dragert, H., Wang, K., and James, T. S. (2001). A silent slip event on the deeper Cascadia subduction interface. *Science*, 292(5521):1525–1528.

Ducellier, A. and Creager, K. C. (2022). Depth and thickness of tectonic tremor in the northeastern Olympic Peninsula. *Journal of Geophysical Research: Solid Earth*, 127(1):e2021JB022708.

Egbert, G. D., Yang, B., Bedrosian, P. A., Key, K., Livelybrooks, D. W., Schultz, A., Kelbert, A., and Parris, B. (2022). Fluid transport and storage in the Cascadia forearc influenced by overriding plate lithology. *Nature Geoscience*, 15(8):677–682.

Ester, M., Kriegel, H.-P., Sander, J., and Xu, X. (1996). A density-based algorithm for discovering clusters in large spatial databases with noise. In *Proceedings of the Second International Conference on Knowledge Discovery and Data Mining*, KDD'96, page 226–231. AAAI Press.

Fan, W., Barbour, A. J., McGuire, J. J., Huang, Y., Lin, G., Cochran, E. S., and Okuwaki, R. (2022). Very low frequency earthquakes in between the seismogenic and tremor zones in Cascadia? *AGU Advances*, 3(2):e2021AV000607.

Farge, G., Jaupart, C., Frank, W. B., and Shapiro, N. M. (2023). Along-strike segmentation of seismic tremor and its relationship with the hydraulic structure of the subduction fault zone. *Journal of Geophysical Research: Solid Earth*, 128(12):e2023JB027584.

Finley, T., Morell, K., Leonard, L., Regalla, C., Johnston, S. T., and Zhang, W. (2019). Ongoing oroclinal bending in the Cascadia forearc and its relation to concave-outboard plate margin geometry. *Geology*, 47(2):155–158.

Font, Y., Kao, H., Lallemand, S., Liu, C.-S., and Chiao, L.-Y. (2004). Hypocentre determination offshore of eastern Taiwan using the maximum intersection method. *Geophysical Journal International*, 158(2):655–675.

Frank, W. B. (2016). Slow slip hidden in the noise: The intermittence of tectonic release. *Geophysical Research Letters*, 43(19):10,125–10,133.

Frank, W. B. and Brodsky, E. E. (2019). Daily measurement of slow slip from low-frequency earthquakes is consistent with ordinary earthquake scaling. *Science Advances*, 5(10):eaaw9386.

Frank, W. B., Shapiro, N. M., Husker, A. L., Kostoglodov, V., Romanenko, A., and Campillo, M. (2014). Using systematically characterized low-frequency earthquakes as a fault probe in Guerrero, Mexico. *Journal of Geophysical Research: Solid Earth*, 119(10):7686–7700.

Gao, X. and Wang, K. (2017). Rheological separation of the megathrust seismogenic zone and episodic tremor and slip. *Nature*, 543(7645):416–419.

Ghosh, A., Vidale, J. E., and Creager, K. C. (2012). Tremor asperities in the transition zone control evolution of slow earthquakes. *Journal of Geophysical Research: Solid Earth*, 117(B10):B10301.

Ghosh, A., Vidale, J. E., Sweet, J. R., Creager, K. C., Wech, A. G., Houston, H., and Brodsky, E. E. (2010). Rapid, continuous streaking of tremor in Cascadia. *Geochemistry, Geophysics, Geosystems*, 11(12):Q12010.

Gombert, B. and Hawthorne, J. C. (2023). Rapid tremor migration during few minute-long slow earthquakes in Cascadia. *Journal of Geophysical Research: Solid Earth*, 128(2):e2022JB025034.

Hall, K., Schmidt, D., and Houston, H. (2019). Peak tremor rates lead peak slip rates during propagation of two large slow earthquakes in Cascadia. *Geochemistry, Geophysics, Geosystems*, 20(11):4665–4675.

Haney, M. M. (2014). Backprojection of volcanic tremor. *Geophysical Research Letters*, 41(6):1923–1928.

Hirose, H. and Obara, K. (2005). Repeating short- and long-term slow slip events with deep tremor activity around the Bungo channel region, southwest Japan. *Earth, Planets and Space*, 57(10):961–972.

Hyndman, R. D., McCrory, P. A., Wech, A., Kao, H., and Ague, J. (2015). Cascadia subducting plate fluids channelled to fore-arc mantle corner: ETS and silica deposition. *Journal of Geophysical Research: Solid Earth*, 120(6):4344–4358.

Hyndman, R. D., Yorath, C. J., Clowes, R. M., and Davis, E. E. (1990). The northern Cascadia subduction zone at Vancouver Island: seismic structure and tectonic history. *Canadian Journal of Earth Sciences*, 27(3):313–329.

Ide, S. (2010). Striations, duration, migration and tidal response in deep tremor. *Nature*, 466(7304):356–359.

Ide, S. (2012). Variety and spatial heterogeneity of tectonic tremor worldwide. *Journal of Geophysical Research: Solid Earth*, 117(B3):B03302.

Ide, S. (2016). Characteristics of slow earthquakes in the very low frequency band: Application to the Cascadia subduction zone. *Journal of Geophysical Research: Solid Earth*, 121(8):5942–5952.

Ide, S. (2019). Detection of low-frequency earthquakes in broadband random time sequences: Are they independent events? *Journal of Geophysical Research: Solid Earth*, 124(8):8611–8625.

Ide, S. (2021). Empirical low-frequency earthquakes synthesized from tectonic tremor records. *Journal of Geophysical Research: Solid Earth*, 126(12):e2021JB022498.

Ide, S., Imanishi, K., Yoshida, Y., Beroza, G. C., and Shelly, D. R. (2008). Bridging the gap between seismically and geodetically detected slow earthquakes. *Geophysical Research Letters*, 35(10).

Ide, S., Shelly, D. R., and Beroza, G. C. (2007). Mechanism of deep low frequency earthquakes: Further evidence that deep non-volcanic tremor is generated by shear slip on the plate interface. *Geophysical Research Letters*, 34(3):L03308.

Idehara, K., Yabe, S., and Ide, S. (2014). Regional and global variations in the temporal clustering of tectonic tremor activity. *Earth, Planets and Space*, 66(66):1880–5981.

Itoh, Y., Aoki, Y., and Fukuda, J. (2022). Imaging evolution of Cascadia slow-slip event using high-rate GPS. *Scientific Reports*, 12(1):7179.

Johnson, C. E., Lindh, A., Hirshorn, B., and (U.S.), G. S. (1997). *Robust regional phase association [microform] / by Carl E. Johnson, Allan G. Lindh, and Barry Hirshorn*. U.S. Dept. of the Interior, U.S. Geological Survey [Menlo Park, CA].

Kao, H. and Shan, S.-J. (2004). The source-scanning algorithm: mapping the distribution of seismic sources in time and space. *Geophysical Journal International*, 157(2):589–594.

Kao, H., Shan, S.-J., Dragert, H., and Rogers, G. (2009). Northern Cascadia episodic tremor and slip: A decade of tremor observations from 1997 to 2007. *Journal of Geophysical Research: Solid Earth*, 114(B11):B00A12.

Kao, H., Shan, S.-J., Dragert, H., Rogers, G., Cassidy, J. F., Wang, K., James, T. S., and Ramachandran, K. (2006). Spatial-temporal patterns of seismic tremors in northern Cascadia. *Journal of Geophysical Research: Solid Earth*, 111(B3):B03309.

Kao, H., Wang, K., Dragert, H., Kao, J. Y., and Rogers, G. (2010). Estimating seismic moment magnitude (Mw) of tremor bursts in northern Cascadia: Implications for the "seismic efficiency" of episodic tremor and slip. *Geophysical Research Letters*, 37(19).

Kato, A., Iidaka, T., Ikuta, R., Yoshida, Y., Katsumata, K., Iwasaki, T., Sakai, S., Thurber, C., Tsumura, N., Yamaoka, K., Watanabe, T., Kunitomo, T., Yamazaki, F., Okubo, M., Suzuki, S., and Hirata, N. (2010). Variations of fluid pressure within the subducting oceanic crust and slow earthquakes. *Geophysical Research Letters*, 37(14).

Kirkpatrick, J. D., Fagereng, Å., and Shelly, D. R. (2021). Geological constraints on the mechanisms of slow earthquakes. *Nature Reviews Earth & Environment*, 2(4):285–301.

La Rocca, M., Galluzzo, D., Malone, S., McCausland, W., and Del Pezzo, E. (2010). Array analysis and precise source location of deep tremor in Cascadia. *Journal of Geophysical Research: Solid Earth*, 115(B6):B00A20.

La Rocca, M., McCausland, W., Galluzzo, D., Malone, S., Saccorotti, G., and Del Pezzo, E. (2005). Array measurements of deep tremor signals in the Cascadia subduction zone. *Geophysical Research Letters*, 32(21):L21319.

Li, G., Liu, Y., Regalla, C., and Morell, K. D. (2018). Seismicity relocation and fault structure near the Leech River Fault Zone, Southern Vancouver Island. *Journal of Geophysical Research: Solid Earth*, 123(4):2841–2855.

Li, K. L., Sadeghisorkhani, H., Sgattoni, G., Gudmundsson, O., and Roberts, R. (2017). Locating tremor using stacked products of correlations. *Geophys. Res. Lett.*, 44(7):3156–3164.

Luo, Y. and Liu, Z. (2021). Fault zone heterogeneities explain depth-dependent pattern and evolution of slow earthquakes in Cascadia. *Nature Communications*, 12(1):1959.

Mahadevan, L., Bendick, R., and Liang, H. (2010). Why subduction zones are curved. *Tectonics*, 29(6).

McBrearty, I. W., Gomberg, J., Delorey, A. A., and Johnson, P. A. (2019). Earthquake arrival association with backprojection and graph theory. *Bulletin of the Seismological Society of America*, 109(6):2510–2531.

McCausland, W. A., Creager, K. C., La Rocca, M., and Malone, S. D. (2010). Short-term and long-term tremor migration patterns of the Cascadia 2004 tremor and slow slip episode using small aperture seismic arrays. *Journal of Geophysical Research: Solid Earth*, 115(B8):B00A24.

McCrory, P. A., Blair, J. L., Waldhauser, F., and Oppenheimer, D. H. (2012). Juan de Fuca slab geometry and its relation to Wadati-Benioff zone seismicity. *Journal of Geophysical Research: Solid Earth*, 117(B9):B09306.

McCrory, P. A., Hyndman, R. D., and Blair, J. L. (2014). Relationship between the Cascadia fore-arc mantle wedge, nonvolcanic tremor, and the downdip limit of seismogenic rupture. *Geochemistry, Geophysics, Geosystems*, 15(4):1071–1095.

McLellan, M., Audet, P., Rosas, J. C., and Currie, C. (2022). Margin-wide variations in slab dehydration in Cascadia and their relationship to slow slip. *Lithos*, 434-435:106912.

Merrill, R., Bostock, M. G., Peacock, S. M., Calvert, A. J., and Christensen, N. I. (2020). A double difference tomography study of the Washington forearc: Does Siletzia control crustal seismicity? *Journal of Geophysical Research: Solid Earth*, 125(10):e2020JB019750.

Morton, E. A., Bilek, S. L., and Rowe, C. A. (2023). Cascadia subduction zone fault heterogeneities from newly detected small magnitude earthquakes. *Journal of Geophysical Research: Solid Earth*, 128(6):e2023JB026607.

Nakajima, J. and Hasegawa, A. (2016). Tremor activity inhibited by well-drained conditions above a megathrust. *Nature Communications*, 7(1):13863.

Nedimović, M. R., Hyndman, R. D., Ramachandran, K., and Spence, G. D. (2003). Reflection signature of seismic and aseismic slip on the northern Cascadia subduction interface. *Nature*, 424(6947):416–420.

Nicholson, T., Bostock, M., and Cassidy, J. F. (2005). New constraints on subduction zone structure in northern Cascadia. *Geophysical Journal International*, 161(3):849–859.

Nishikawa, T., Ide, S., and Nishimura, T. (2023). A review on slow earthquakes in the Japan Trench. *Progress in Earth and Planetary Science*, 10(1):1.

Obara, K. (2002). Nonvolcanic deep tremor associated with subduction in southwest Japan. *Science*, 296(5573):1679–1681.

Obara, K. and Kato, A. (2016). Connecting slow earthquakes to huge earthquakes. *Science*, 353(6296):253–257.

Obara, K., Tanaka, S., Maeda, T., and Matsuzawa, T. (2010). Depth-dependent activity of non-volcanic tremor in southwest Japan. *Geophysical Research Letters*, 37(13).

Peacock, S. M. (2009). Thermal and metamorphic environment of subduction zone episodic tremor and slip. *Journal of Geophysical Research: Solid Earth*, 114(B8):B00A07.

Pedregosa, F., Varoquaux, G., Gramfort, A., Michel, V., Thirion, B., Grisel, O., Blondel, M., Prettenhofer, P., Weiss, R., Dubourg, V., Vanderplas, J., Passos, A., Cournapeau, D., Brucher, M., Perrot, M., and Duchesnay, E. (2011). Scikit-learn: Machine learning in Python. *Journal of Machine Learning Research*, 12:2825–2830.

Peng, Y. and Rubin, A. M. (2016). High-resolution images of tremor migrations beneath the Olympic Peninsula from stacked array of arrays seismic data. *Geochemistry, Geophysics, Geosystems*, 17(2):587–601.

Peng, Y., Rubin, A. M., Bostock, M. G., and Armbruster, J. G. (2015). High-resolution imaging of rapid tremor migrations beneath southern Vancouver Island using cross-station cross correlations. *Journal of Geophysical Research: Solid Earth*, 120(6):4317–4332.

Peng, Z. and Gomberg, J. (2010). An integrated perspective of the continuum between earthquakes and slow-slip phenomena. *Nature Geoscience*, 3(9):599–607.

Platt, J. P., Xia, H., and Schmidt, W. L. (2018). Rheology and stress in subduction zones around the aseismic/seismic transition. *Progress in Earth and Planetary Science*, 5(1):24.

Preston, L. A., Creager, K. C., Crosson, R. S., Brocher, T. M., and Trehu, A. M. (2003). Intraslab earthquakes: Dehydration of the Cascadia slab. *Science*, 302(5648):1197–1200.

Ramachandran, K., Dosso, S. E., Spence, G. D., Hyndman, R. D., and Brocher, T. M. (2005). Forearc structure beneath southwestern British Columbia: A three-dimensional tomographic velocity model. *Journal of Geophysical Research: Solid Earth*, 110(B2).

Ramachandran, K. and Hyndman, R. D. (2012). The fate of fluids released from subducting slab in northern Cascadia. *Solid Earth*, 3(1):121–129.

Ramachandran, K., Hyndman, R. D., and Brocher, T. M. (2006). Regional P wave velocity structure of the northern Cascadia subduction zone. *Journal of Geophysical Research: Solid Earth*, 111(B12).

Rogers, G. and Dragert, H. (2003). Episodic tremor and slip on the Cascadia subduction zone: The chatter of silent slip. *Science*, 300(5627):1942–1943.

Royer, A. and Bostock, M. G. (2014). A comparative study of low frequency earthquake templates in northern Cascadia. *Earth and Planetary Science Letters*, 402:247–256.

Sammis, C. G. and Bostock, M. G. (2021). A granular jamming model for low-frequency earthquakes. *Journal of Geophysical Research: Solid Earth*, 126(7):e2021JB021963.

Savard, G. and Bostock, M. G. (2015). Detection and location of low-frequency earthquakes using cross-station correlation. *Bulletin of the Seismological Society of America*, 105(4):2128–2142.

Savard, G., Bostock, M. G., and Christensen, N. I. (2018). Seismicity, metamorphism, and fluid evolution across the northern Cascadia fore arc. *Geochemistry, Geophysics, Geosystems*, 19(6):1881–1897.

Sawaki, Y., Ito, Y., Ohta, K., Shibutani, T., and Iwata, T. (2021). Seismological structures on bimodal distribution of deep tectonic tremor. *Geophysical Research Letters*, 48(8):e2020GL092183.

Schneider, M., Flury, H., Guttorp, P., and Wright, A. (2023). Earthquake catalog processing and swarm identification for the Pacific Northwest. *Seismological Research Letters*, 94(5):2500–2513.

Schwartz, S. Y. and Rokosky, J. M. (2007). Slow slip events and seismic tremor at circum-pacific subduction zones. *Reviews of Geophysics*, 45(3).

Shapiro, N. M., Campillo, M., Kaminski, E., Vilotte, J.-P., and Jaupart, C. (2018). Low-frequency earthquakes and pore pressure transients in subduction zones. *Geophysical Research Letters*, 45(20):11,083–11,094.

Shelly, D. R., Beroza, G. C., and Ide, S. (2007). Non-volcanic tremor and low-frequency earthquake swarms. *Nature*, 446(7133):305–307.

Shelly, D. R., Beroza, G. C., Ide, S., and Nakamula, S. (2006). Low-frequency earthquakes in Shikoku, Japan, and their relationship to episodic tremor and slip. *Nature*, 442(7099):188–191.

Sibson, R. H. (1990). Conditions for fault-valve behaviour. *Geological Society, London, Special Publications*, 54(1):15–28.

Sibson, R. H. (2013). Stress switching in subduction forearcs: Implications for overpressure containment and strength cycling on megathrusts. *Tectonophysics*, 600:142–152.

Sibson, R. H. (2017). Tensile overpressure compartments on low-angle thrust faults. *Earth, Planets and Space*, 69(1):113.

Takemura, S., Hamada, Y., Okuda, H., Okada, Y., Okubo, K., Akuhara, T., Noda, A., and Tonegawa, T. (2023). A review of shallow slow earthquakes along the Nankai trough. *Earth, Planets and Space*, 75(1):164.

Tan, F., Kao, H., Nissen, E., and Eaton, D. (2019). Seismicity-scanning based on navigated automatic phase-picking. *Journal of Geophysical Research: Solid Earth*, 124(4):3802–3818.

Ujiie, K., Saishu, H., Fagereng, A., Nishiyama, N., Otsubo, M., Masuyama, H., and Kagi, H. (2018). An explanation of episodic tremor and slow slip constrained by crack-seal veins and viscous shear in subduction melange. *Geophysical Research Letters*, 45(11):5371–5379.

Wallace, L. M. (2020). Slow slip events in New Zealand. *Annual Review of Earth and Planetary Sciences*, 48(Volume 48, 2020):175–203.

Wang, K. and Tréhu, A. M. (2016). Invited review paper: Some outstanding issues in the study of great megathrust earthquakes—the Cascadia example. *Journal of Geodynamics*, 98:1–18.

Wang, Q.-Y., Frank, W. B., Abercrombie, R. E., Obara, K., and Kato, A. (2023). What makes low-frequency earthquakes low frequency. *Science Advances*, 9(32):eadh3688.

Wech, A. G. (2010). Interactive tremor monitoring. *Seismological Research Letters*, 81(4):664–669.

Wech, A. G. (2021). Cataloging tectonic tremor energy radiation in the Cascadia subduction zone. *Journal of Geophysical Research: Solid Earth*, 126(10):e2021JB022523.

Wech, A. G. and Bartlow, N. M. (2014). Slip rate and tremor genesis in Cascadia. *Geophysical Research Letters*, 41(2):392–398.

Wech, A. G. and Creager, K. C. (2007). Cascadia tremor polarization evidence for plate interface slip. *Geophysical Research Letters*, 34(22).

Wech, A. G. and Creager, K. C. (2008). Automated detection and location of Cascadia tremor. *Geophysical Research Letters*, 35(20):L20302.

Wech, A. G. and Creager, K. C. (2011). A continuum of stress, strength and slip in the Cascadia subduction zone. *Nature Geoscience*, 4(9):624–628.

Wech, A. G., Creager, K. C., and Melbourne, T. I. (2009). Seismic and geodetic constraints on Cascadia slow slip. *Journal of Geophysical Research: Solid Earth*, 114(B10):B10316.

Wells, R. E., Blakely, R. J., and Weaver, C. S. (2002). Cascadia microplate models and within-slab earthquakes. Open File 4350, Geological Survey of Canada.

Wells, R. E., Blakely, R. J., Wech, A. G., McCrory, P. A., and Michael, A. (2017). Cascadia subduction tremor muted by crustal faults. *Geology*, 45(6):515–518.

White, M. C. A., Fang, H., Nakata, N., and Ben-Zion, Y. (2020). PyKonal: A Python package for solving the Eikonal equation in spherical and Cartesian coordinates using the fast marching method. *Seismological Research Letters*, 91(4):2378–2389.

Yarce, J., Sheehan, A. F., and Roecker, S. (2023). Temporal relationship of slow slip events and microearthquake seismicity: Insights from earthquake automatic detections in the northern Hikurangi margin, Aotearoa New Zealand. *Geochemistry, Geophysics, Geosystems*, 24(3):e2022GC010537.

Yuan, C., Cochard, T., Denolle, M., Gomberg, J., Wech, A., Xiao, L., and Weitz, D. (2024). Laboratory hydrofractures as analogs to tectonic tremors. *AGU Advances*, 5(1):e2023AV001002.